The Computer Simulation of Liquid Crystals

Mark Alistair Warren

H. H. Wills Physics Laboratory,

University of Bristol

A thesis submitted to the University of Bristol

in accordance with the requirements for the degree of

Doctor of Philosophy

in the Faculty of Science

March 1997

Abstract

In this thesis, we investigate several aspects of the behaviour of systems of elongated molecules, using large scale computer simulations of a simple single site model. For much of this work, we made use of parallel molecular dynamics programs, which are discussed briefly. We then describe three essentially independent research topics.

The first of these concerns the measurement of the Frank elastic constants K_1–K_3, which describe the energy cost of orientational deformations in the nematic phase. A technique for constraining the director during a simulation is introduced, and used to facilitate measurement of appropriate components of fluctuations in the reciprocal space order tensor. By extrapolating to low wavevectors, we obtain estimates of the elastic constants K_1–K_3. Our values agree with those obtained by carrying out the same simulation in the unconstrained ensemble, and qualitatively with experiment.

Next, we report the results of extensive simulations of a large system of Gay-Berne particles near the weakly first order nematic-isotropic transition. We examine the divergence of correlation lengths, behaviour of direct correlation functions, and collective reorientation times in the neighbourhood of the transition temperature T_{NI}, and compare our results with theory. We also discuss briefly the kinetics of a quench of a very large system from the isotropic into the nematic phase.

The recent theoretical and experimental discovery of a new class of liquid crystal phases has generated much excitement. In our third project, we attempt a molecular-scale simulation of the *twist grain boundary* (TGB) phase, mimicking a twist-cell experiment by means of modified boundary conditions. The orientational and translational ordering seen is consistent with the structure of the TGB phase. We develop a technique for automatically locating twist defects, based on simulated annealing; the distribution and nature of defects found in our configurations provide further evidence for the identity of the phase.

Acknowledgements

I should like to thank my advisor, Dr. Mike Allen, for his insights, teaching, patience and encouragement.

I wish to acknowledge support from the Engineering and Physical Sciences Research Council, and from Daresbury Laboratory, in the form of maintainance grants and the provision of computing facilities.

I should also like to thank staff at CINECA (Bologna) and Edinburgh Parallel Computing Centre, and my CASE supervisor at Daresbury, Dr. W. Smith, for their helpful advice on parallel programming and other matters. I am also indebted to Mark Wilson and Alain Sauron, and other contributors to the High Performance Computing Initiative consortium on "Simulation and Statistical Mechanics of Complex Fluids", for their role in developing the parallel codes used in much of my work. Also, a thank you to Martin Bates and the Southampton group for introducing me to their version of the Gay-Berne potential. Thanks are due to J. P. Melot for keeping the departmental computing facilities in such good shape, and to the departmental librarians for their help.

Many people in Bristol and beyond have sustained me during my time here, with scientific discussions, advice, and above all friendship. My heartfelt thanks to all of them, and especially to present and past members of the theory group - Raúl, Carl, Julian, Philip, Héctor and Jeroen - to Steve, Massimo, Ben and Kate, and Esther. Finally, I would like to thank Gill, Chris and Rebecca, and my family for their love and support: words are not enough.

Is not chance the antithesis of all law?

- Bertrand Russell

Author's Declaration

I declare that no part of this thesis has been submitted for a higher degree in this, or any other, university. The research reported herein is the result of my own investigation except where reference is made to the work of others. All research was carried out under the supervision of Dr. M. P. Allen at the University of Bristol, between October 1992 and March 1997.

M. Alwarren

Mark Alistair Warren

March 1997

Contents

List of Figures

List of Tables

Chapter 1

Introduction

1.1 Liquid crystal phases

Three forms of matter: solid, liquid and gas, are familiar from our everyday lives. Many of the properties which distinguish them, such as density, rigidity and thermal conductivity, are immediately evident. Equally familiar is the idea that a single substance such as water can be transformed between these different states by altering external conditions of temperature and pressure. In the last century, great advances have been made in understanding how these phases, and the transformations between them, are related to the microscopic behaviour of matter. Central to this understanding is the observation that phase transitions are often accompanied by a change in *symmetry*. The freezing transition, for example, is characterised by the breaking of rotational and translational symmetry, so that in the solid phase the only operations which leave the structure unchanged are the point group symmetries of the unit cell and translation through multiples of the lattice vectors.

At normal temperatures and pressures, all monatomic substances, and many polyatomic ones, only have these three phases. However, at the end of the nineteenth century, it was discovered that on cooling certain liquids, solidification is preceded by the formation of *mesophases*, or liquid crystalline phases, in which there is an intermediate degree of symmetry breaking. A common feature of most molecules (mesogens) which give rise to these phases is that they are highly elongated. Typical

Chapter 1

Introduction

1.1 Liquid crystal phases

Three forms of matter: solid, liquid and gas, are familiar from our everyday lives. Many of the properties which distinguish them, such as density, rigidity and thermal conductivity, are immediately evident. Equally familiar is the idea that a single substance such as water can be transformed between these different states by altering external conditions of temperature and pressure. In the last century, great advances have been made in understanding how these phases, and the transformations between them, are related to the microscopic behaviour of matter. Central to this understanding is the observation that phase transitions are often accompanied by a change in *symmetry*. The freezing transition, for example, is characterised by the breaking of rotational and translational symmetry, so that in the solid phase the only operations which leave the structure unchanged are the point group symmetries of the unit cell and translation through multiples of the lattice vectors.

At normal temperatures and pressures, all monatomic substances, and many polyatomic ones, only have these three phases. However, at the end of the nineteenth century, it was discovered that on cooling certain liquids, solidification is preceded by the formation of *mesophases*, or liquid crystalline phases, in which there is an intermediate degree of symmetry breaking. A common feature of most molecules (mesogens) which give rise to these phases is that they are highly elongated. Typical

examples are shown in figure 1.1. This anisotropy hints at the structure of liquid

Figure 1.1: Two common mesogens, *N*-(*p*-methoxybenzylidene)-*p*-butylaniline (MMBA) and *p*-azoxyanisole (PAA). At atmospheric pressure, these materials form a nematic phase in the indicated temperature range.

MMBA
(20°C – 47°C)

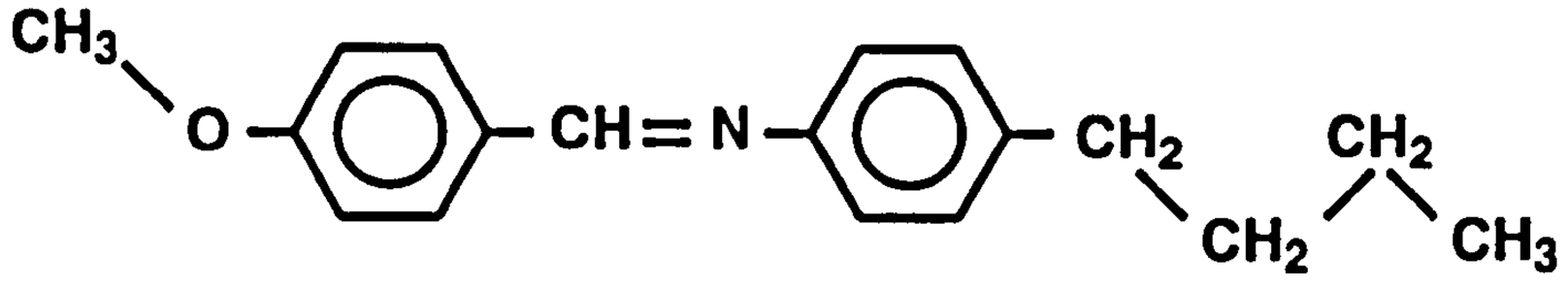

PAA
(116°C – 135°C)

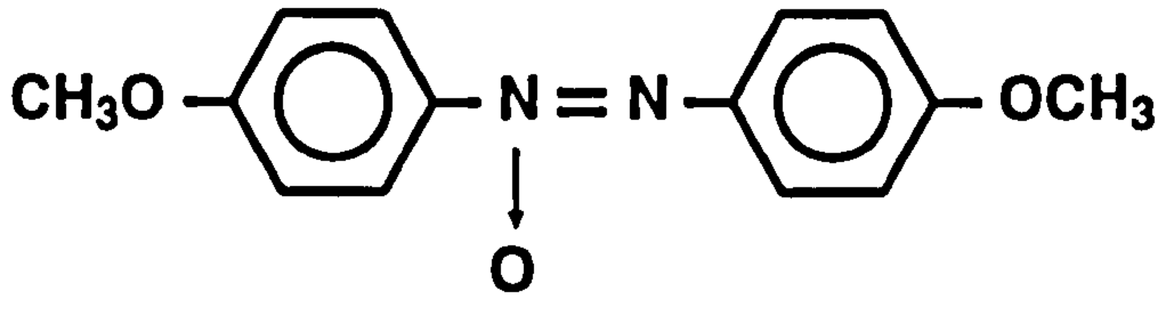

crystalline phases: they all have a lower rotational symmetry with respect to the isotropic liquid. In the case of *nematics* this is the only broken symmetry - molecules are preferentially aligned along a certain direction, the *director*. In *smectics*, there is also some degree of translational ordering, but less than the full periodicity of the solid. In the smectic A phase, there is a periodic modulation of the density along the director. In chapters 3 and 4 of this thesis, we shall be investigating the properties of the nematic and isotropic phases. The smectic A phase is relevant to chapter 5. For illustrative purposes, we show typical configurations from computer simulations of these three phases in figure 1.2. There are many other mesophases, including biaxial nematics, discotics and columnar phases, blue phases, tilted smectics, and a plethora of chiral phases. Details of these can be found in [1–3]. The recently discovered *twist grain boundary* phase is the subject of some of the work in this thesis; we defer description of this phase to chapter 5. Liquid crystal phases are quite delicate - their structure can be modified quite easily by applying external fields. This property is of great importance for LCD technology, which relies on the

ability to modify the optical properties of a nematic liquid crystal by applying an electric field. An overview of technological applications can be found in [4].

Figure 1.2: Isotropic, nematic and smectic phases.

Isotropic phase

- Short-range order of molecular orientations.
- Short-range order of molecular positions.

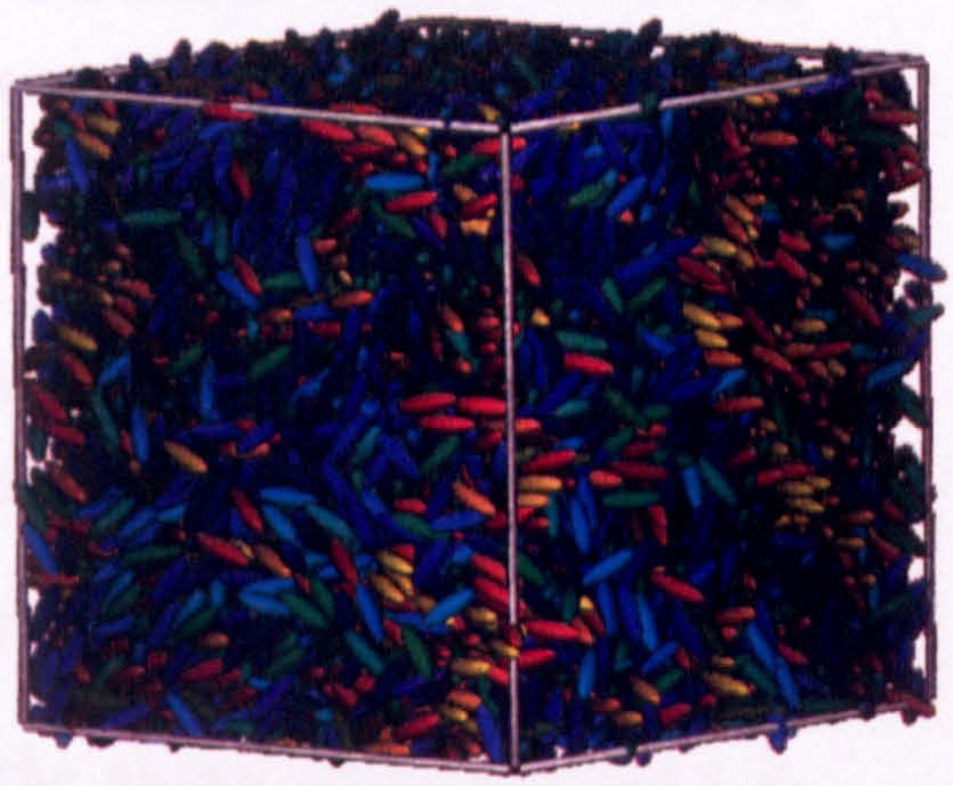

Nematic phase

- Long-range orientational order .
- Short-range order of molecular positions.

Director $\mathbf{n}$, uniaxial symmetry, $\mathbf{n} \equiv -\mathbf{n}$.

Order parameter $S = \langle P_2(\mathbf{e} \cdot \mathbf{n}) \rangle$.

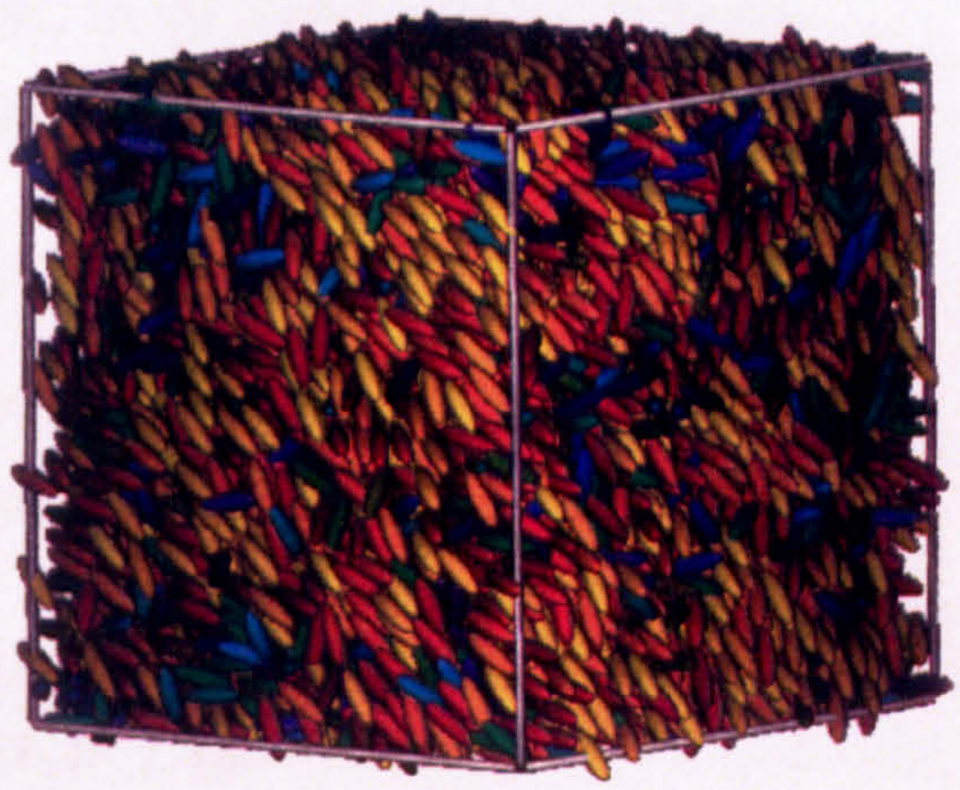

Smectic A phase

- Orientational order as nematic.
- Long-range positional order in one dimension.

Layer normal $\mathbf{N}$ (coupled to $\mathbf{n}$).

Complex order parameter $\psi(\mathbf{r})$.

(See section 5.2).

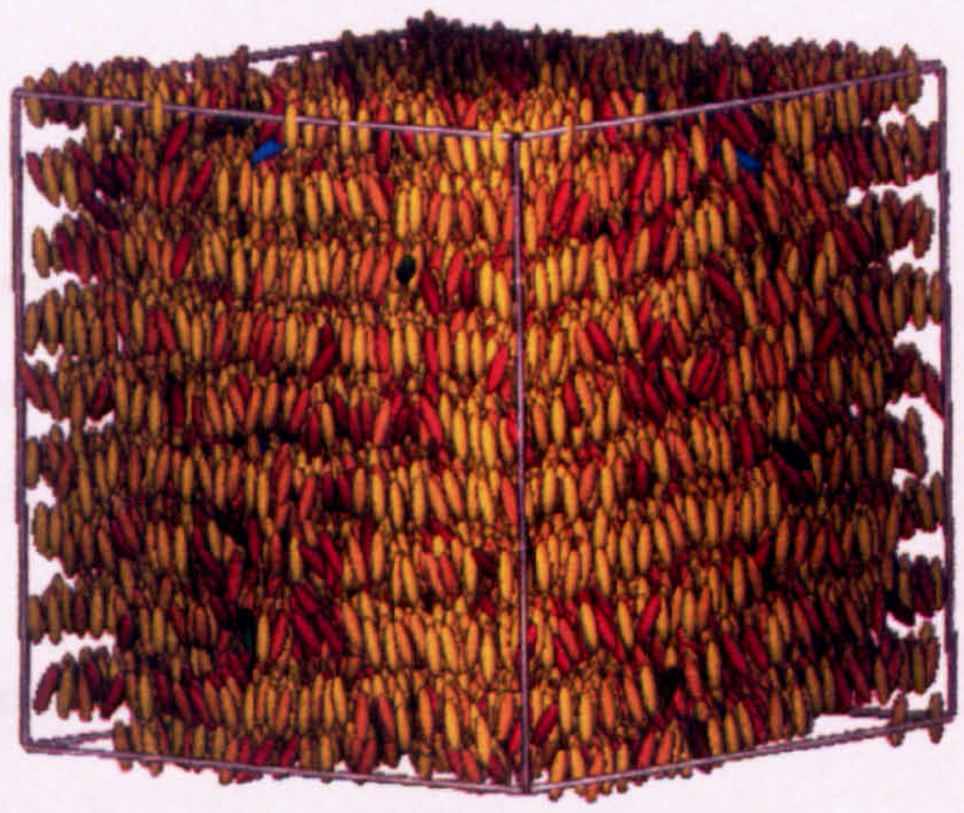

1.2 Static and dynamical averages

The formalism of statistical mechanics [5, 6], which relates the structure of matter at the atomic and molecular level to its macroscopic properties, was developed at the end of the 19$^{\text{th}}$ century by Ludwig Boltzmann and Josiah Willard Gibbs. The fundamental concept which enables this link to be made is that of the *statistical ensemble*. Values of macroscopic observables in a thermodynamic system at equilibrium can be expressed as averages over an ensemble. In a system of N particles, with positions $\mathbf{r} \equiv \{\mathbf{r}_1, \mathbf{r}_2 \cdots \mathbf{r}_N\}$ and conjugate momenta $\mathbf{p} \equiv \{\mathbf{p}_1, \mathbf{p}_2 \cdots \mathbf{p}_N\}$, governed by a Hamiltonian $\mathcal{H}(\mathbf{r}, \mathbf{p})$, an ensemble average of a variable $A(\mathbf{r}, \mathbf{p})$ takes the form

$$\langle A \rangle_{\text{Gibbs}} = \int \int \mathrm{d}\mathbf{r}\, \mathrm{d}\mathbf{p}\; f(\mathbf{r}, \mathbf{p})\, A(\mathbf{r}, \mathbf{p}) \; . \tag{1.1}$$

The phase space distribution $f(\mathbf{r}, \mathbf{p})$ depends on the nature of the external constraints to which the system is subjected; for example, in the microcanonical ensemble, the number of particles N, volume V and total energy E are fixed, and

$$f_{\text{NVE}}(\mathbf{r}, \mathbf{p}) = \frac{\delta\left[\mathcal{H}(\mathbf{r}, \mathbf{p}) - E\right]}{\int \int \mathrm{d}\mathbf{r}\, \mathrm{d}\mathbf{p}\; \delta\left[\mathcal{H}(\mathbf{r}, \mathbf{p}) - E\right]} \; , \tag{1.2}$$

so that the average in eqn (1.1) is over an isosurface of total energy.

At constant number, temperature and volume, the average is over the canonical ensemble:

$$f_{\text{NVT}}(\mathbf{r}, \mathbf{p}) = \frac{\exp\left[-\mathcal{H}(\mathbf{r}, \mathbf{p}) \,/\, k_B T\right]}{\int \int \mathrm{d}\mathbf{r}\, \mathrm{d}\mathbf{p}\; \exp\left[-\mathcal{H}(\mathbf{r}, \mathbf{p}) \,/\, k_B T\right]} \; . \tag{1.3}$$

In the Boltzmann formulation, macroscopic observables are expressed as dynamical averages,

$$\langle A \rangle_{\text{Boltzmann}} = \lim_{\tau \to \infty} \frac{1}{\tau} \int_0^{\tau} \mathrm{d}t\; A\left[\mathbf{r}(t), \mathbf{p}(t)\right] \tag{1.4}$$

The Gibbs and Boltzmann averages are equivalent, since (except in pathological cases), Hamiltonian systems are ergodic. We assume this to be the case for the many-particle systems studied here, and henceforth will denote averages of either kind by $\langle \cdots \rangle$.

In some cases, we may wish to calculate *dynamical* quantities. Of particular interest are time correlation functions defined by

$$C_{AA}(t) = \langle A(t) A(0) \rangle \; . \tag{1.5}$$

These describe the decay of fluctuations of a variable A, and are also related to the linear response of the system to an external, time varying field coupling to A [7,8]. In certain instances, they can be measured experimentally, for example inelastic neutron scattering probes density correlations, $\langle \rho_{\mathbf{k}}(t)\rho^*_{\mathbf{k}}(0)\rangle$. Similarly defined functions are useful in characterising orientational fluctuations in anisotropic fluids, a topic which we touch on in chapter 4.

1.3 Mean field theories

Solving a problem in statistical mechanics means, in its fullest sense, evaluating the partition function, a sum over all classical phase space or over all quantum states, from which all thermodynamic functions and ensemble averages can be derived. However, the partition function, though often easy to write down for a given system, is fearsomely difficult to evaluate. Exact solutions are few and far between, and most are for lattice systems [9], most famously the 2D Ising ferromagnet, which was solved by Onsager in 1944 [10]. To date, no exact solutions have been obtained for even the simplest model of a liquid crystal, the Lebwohl-Lasher [11,12] model. Much of the work in the past century has therefore consisted of constructing approximate theories which can be solved analytically. The most far ranging of these are *mean field theories*, which provide a unifying framework for discussing phase transitions. They are based on the concept of an *order parameter*, a macroscopic average which is zero in the disordered phase, and nonzero in the ordered phase. For example, the order parameter which describes the nematic-isotropic (NI) transition is a traceless second rank tensor, formed by averaging over the particle orientations $\mathbf{e_i}$:

$$Q_{\alpha\beta} = \frac{V}{N}\sum_{i=1}^{N}\left\{e_{i\alpha}e_{i\beta} - \tfrac{1}{3}\delta_{\alpha\beta}\right\} . \tag{1.6}$$

A phenomenological mean field theory (MFT) of the NI transition can be derived by expanding the free energy in powers of the order parameter. In the NI case, the free energy expansion is (see for example [13]):

$$f \;=\; \frac{1}{2}r\left(\frac{3}{2}\mathrm{Tr}Q^2\right) - w\left(\frac{9}{2}\mathrm{Tr}Q^3\right) + u\left(\frac{3}{2}\mathrm{Tr}Q^2\right)^2 \tag{1.7}$$

$$= \frac{1}{2}rS^2 - wS^3 - uS^4 , \tag{1.8}$$

where S is the largest eigenvalue of Q, $r = a(T - T^*)$ and w and u are positive phenomenological constants. This model free energy captures several important aspects of the transition. Firstly, it shows that the transition is first order: the transition occurs at a temperature T_{NI}, with $a(T_{\mathrm{NI}} - T^*) = w^2/2u$. On cooling from the isotropic, there is thus a metastable region for $T_{\mathrm{NI}} < T < T^*$ where the isotropic and nematic states are separated by a free energy barrier. Similarly, on heating the nematic, the orientational ordering is metastable up to a temperature T^{**}, with $a(T^{**} - T^*) = 9w^2/16u$. Nematic molecules tend to have anisotropic diamagnetic susceptibilities, and their interaction with a magnetic field can be represented in the free energy by an external field coupling to the order parameter. The theory predicts that the susceptibility to this field $\chi \propto (T - T^*)^{-1}$, i.e. the inverse susceptibility can be extrapolated to zero at the limit of metastability of the nematic phase. MFT can be further extended by allowing the order parameter to vary spatially. The free energy then becomes a functional of the order parameter - usually a spatial average of a term similar to equation eqn (1.6), plus a square gradient term favouring spatial uniformity. Using a theory of this type, Ornstein and Zernike [14] accounted for the divergence of correlation lengths near the critical point in a simple fluid. The treatment can be generalised [3, 13] to describe correlations near the NI transition. There are other ways of formulating a MFT of the nematic-isotropic transition, for example the free energy functional approach of Onsager [15].

1.4 The role of computer simulation

Some approximations in statistical mechanics are extrapolations of an exactly soluble limiting case - in Onsager theory, for example, the limit of infinitely thin rods. In other cases, their physical meaning is less clear, as for example the closure relations (e.g. hypernetted chain and Percus-Yevick) which form the basis of theories of simple fluids [7]. Given the difficulty of obtaining exact analytical results, the question arises: how do we know which approximations are valid? One of the functions of

computer simulation is to answer this question. It provides a way of obtaining exact *numerical* results for a given model. Simulation studies of the hard sphere fluid, for instance, were able to confirm the interesting theoretical result that this system undergoes a freezing transition at a density below close packing [16]. Computer simulation data have occasionally led to altogether new theoretical results, such as the long-time behaviour of velocity autocorrelation functions.

Another motivation of simulation is to determine how well a given model captures experimentally observed behaviour. This is of particular relevance in the field of liquid crystals, where the range of observed phases is large, and the constituent molecules moderately complex. It is known experimentally that the phase diagram morphology of mesogens is very sensitive to the details of molecular structure. However, it is hard to investigate systematically the effects of molecular shape in the laboratory, owing to the difficulty of synthesising and characterising these organic compounds. Computer simulations allow this kind of study to be undertaken, since the form of the intermolecular potential can be altered at will. Another key advantage of simulation is that there is no restriction, *a priori*, on the kinds of observables which may be measured - simulation gives one access to the full microscopic behaviour of the system.

The limitations of computer simulation mostly have to do with the restricted time and length scales which are accessible, given finite computing resources. In efficient algorithms, CPU time scales linearly with the number of particles and duration of the simulation. In some cases, the structure of liquid crystalline phases can be quite subtle. Blue phases, for example, consist of a topologically complex arrangement of the director field which tiles space periodically. A meaningful simulation of this kind of structure would certainly require a system at least as large as the unit cell, which in real systems might contain of the order of 10^6 molecules. The timescale for the formation of really complex structures like this is also very large. For these reasons, molecular scale simulations of blue phases are probably not possible at present. Even in less exotic phases, there are often some quantities of interest which are hard to measure in computer simulations. In a fluid close to a critical point, for instance, there are fluctuations on all length scales. The simulation of critical phenomena, and

in particular measurement of critical exponents, is difficult, since long wavelength fluctuations are suppressed by the periodic boundary conditions. As we shall see, the same issues arise near the NI transition, which exhibits pretransitional divergence of length scales since it is only weakly first order.

Despite these challenges, there is no cause for pessimism. The huge increase in computer power over the last 20 years has enabled an ever wider range of systems to be tackled. This expansion has taken two directions: larger and longer simulations of simple models, and simulation of more complex fluids such as polymers and amphiphilic systems. The latter have been promoted by new mesoscopic simulation techniques, which retain information on both microscopic and macroscopic structure without the need to treat all the degrees of freedom explicitly [17].

1.5 Model potentials

Early simulations of liquid crystal systems were on systems of hard ellipsoids and spherocylinders, the objective being to determine the range of validity of Onsager theory. Since these models are computationally inexpensive, and are in some sense natural anisotropic analogues of hard spheres, they have been extensively studied and much is now known about both their static structure and dynamics. Both ellipsoids and spherocylinders possess a nematic phase if sufficiently elongated; the latter also have smectic phases. A review of these and other hard convex body fluids can be found in [18].

The "canonical" continuous potential for simple fluids is the Lennard-Jones function. Again, there is no unique way of generalising this to model nonspherical molecules. One possibility is to connect Lennard-Jones atoms with rigid bond constraints. Though quite realistic models can be constructed in this way, they are quite computationally expensive, the number of site-site interactions increasing with the square of the chain length. An alternative approach is to use an anisotropic single-site potential. Among the first of these was the Gaussian overlap (GO) potential of Berne and Pechukas [19]. This model represents molecules by anisotropic Gaussian distributions with longitudinal and transverse ranges $\sigma_\perp$ and $\sigma_\parallel$. In the basic

GO model, the interaction potential is simply the overlap integral of the two distributions, a function of the orientations $\mathbf{e}_i$ and $\mathbf{e}_j$, and separation $\mathbf{r} = r\hat{\mathbf{r}}$, of the particles:

$$I_{ij} = \epsilon(\mathbf{e}_i, \mathbf{e}_j) \exp\left[\frac{-r_{ij}^2}{\sigma^2(\hat{\mathbf{r}}, \mathbf{e}_i, \mathbf{e}_j)}\right] . \tag{1.9}$$

In this expression, the well depth and range are given by

$$\epsilon(\mathbf{e}_i, \mathbf{e}_j) = \epsilon_0 \left[1 - \chi^2(\mathbf{e}_i \cdot \mathbf{e}_j)^2\right]^{-\frac{1}{2}} , \tag{1.10}$$

$$\sigma(\hat{\mathbf{r}}, \mathbf{e}_i, \mathbf{e}_j) = \sigma_0 \left[1 - \frac{\chi}{2}\left(\frac{(\hat{\mathbf{r}} \cdot \mathbf{e}_i + \hat{\mathbf{r}} \cdot \mathbf{e}_j)^2}{1 + \chi(\mathbf{e}_i \cdot \mathbf{e}_j)} + \frac{(\hat{\mathbf{r}} \cdot \mathbf{e}_i - \hat{\mathbf{r}} \cdot \mathbf{e}_j)^2}{1 - \chi(\mathbf{e}_i \cdot \mathbf{e}_j)}\right)\right]^{-\frac{1}{2}} , \tag{1.11}$$

where $\chi = (\sigma_\parallel^2 - \sigma_\perp^2)/(\sigma_\parallel^2 + \sigma_\perp^2)$. In order to reproduce the anisotropic short range repulsion and long range attraction of real systems, Berne and Pechukas inserted the above expressions for $\epsilon(\mathbf{e}_i, \mathbf{e}_j)$ and $\sigma(\hat{\mathbf{r}}, \mathbf{e}_i, \mathbf{e}_j)$ into a Lennard-Jones potential:

$$v^{\mathrm{GO}} = 4\epsilon(\mathbf{e}_i, \mathbf{e}_j)\left[\left(\frac{r}{\sigma(\hat{\mathbf{r}}, \mathbf{e}_i, \mathbf{e}_j)}\right)^{12} - \left(\frac{r}{\sigma(\hat{\mathbf{r}}, \mathbf{e}_i, \mathbf{e}_j)}\right)^{6}\right] \tag{1.12}$$

A few unphysical features remain, however. In a linear multisite model (for example a chain of Lennard-Jones atoms), the side-by-side well depth would clearly be significantly higher than in the end-to-end arrangement. The GO model fails to take account of this effect. On the other hand, the GO well-width *does* depend on the relative orientations, and this is not particularly realistic. The Gay-Berne (GB) model [20] addresses both of these problems, at the expense of increasing the computational complexity slightly, and introducing more free parameters. The potential is defined as follows:

$$v^{\mathrm{GB}}(\mathbf{e}_i, \mathbf{e}_j, \mathbf{r}_{ij}) = 4\varepsilon(\mathbf{e}_i, \mathbf{e}_j, \hat{\mathbf{r}}_{ij})\left\{\left(\frac{\sigma_s}{r_{ij} - \sigma(\mathbf{e}_i, \mathbf{e}_j, \hat{\mathbf{r}}_{ij}) + \sigma_s}\right)^{12} - \left(\frac{\sigma_s}{r_{ij} - \sigma(\mathbf{e}_i, \mathbf{e}_j, \hat{\mathbf{r}}_{ij}) + \sigma_s}\right)^{6}\right\} . \tag{1.13}$$

The distance function σ depends on the relative orientations of the molecules and the unit vector $\hat{\mathbf{r}}_{ij} = \mathbf{r}_{ij}/r_{ij}$:

$$\sigma(\mathbf{e}_i, \mathbf{e}_j, \hat{\mathbf{r}}_{ij}) = \sigma_s\left\{1 - \frac{\chi}{2}\left[\frac{(\mathbf{e}_i \cdot \hat{\mathbf{r}}_{ij} + \mathbf{e}_j \cdot \hat{\mathbf{r}}_{ij})^2}{1 + \chi \mathbf{e}_i \cdot \mathbf{e}_j} + \frac{(\mathbf{e}_i \cdot \hat{\mathbf{r}}_{ij} - \mathbf{e}_j \cdot \hat{\mathbf{r}}_{ij})^2}{1 - \chi \mathbf{e}_i \cdot \mathbf{e}_j}\right]\right\}^{-1/2} \tag{1.14}$$

with shape anisotropy parameter $\chi = (\kappa^2 - 1)/(\kappa^2 + 1)$; $\kappa = \sigma_e/\sigma_s$, σ_s is the side-by-side diameter and σ_e the end-to-end diameter. The well-depth function is

$$\varepsilon(\mathbf{e}_i, \mathbf{e}_j, \hat{\mathbf{r}}_{ij}) = \varepsilon_s [\varepsilon'(\mathbf{e}_i, \mathbf{e}_j, \hat{\mathbf{r}}_{ij})]^\mu \times [\varepsilon''(\mathbf{e}_i, \mathbf{e}_j)]^\nu \tag{1.15}$$

$$\varepsilon'(\mathbf{e}_i, \mathbf{e}_j, \hat{\mathbf{r}}_{ij}) = 1 - \frac{\chi'}{2}\left[\frac{(\mathbf{e}_i \cdot \hat{\mathbf{r}}_{ij} + \mathbf{e}_j \cdot \hat{\mathbf{r}}_{ij})^2}{1 + \chi' \mathbf{e}_i \cdot \mathbf{e}_j} + \frac{(\mathbf{e}_i \cdot \hat{\mathbf{r}}_{ij} - \mathbf{e}_j \cdot \hat{\mathbf{r}}_{ij})^2}{1 - \chi' \mathbf{e}_i \cdot \mathbf{e}_j}\right] \tag{1.16}$$

$$\varepsilon''(\mathbf{e}_i, \mathbf{e}_j) = \left[1 - \chi^2 (\mathbf{e}_i \cdot \mathbf{e}_j)^2\right]^{-1/2} \tag{1.17}$$

with well-depth anisotropy parameters $\chi' = (\kappa'^{1/\mu} - 1)/(\kappa'^{1/\mu} + 1)$; $\kappa' = \varepsilon_s/\varepsilon_e$. The two quantities ε_s and ε_e are respectively the side-by-side and end-to-end well depths.

It is usual to apply a spherical cutoff r^c, and so in practice one uses the cut and shifted Gay-Berne potential

$$v^{GBc}(\mathbf{e}_i, \mathbf{e}_j, \mathbf{r}_{ij}) = \begin{cases} v^{GB}(\mathbf{e}_i, \mathbf{e}_j, \mathbf{r}_{ij}) - v^{GB}(\mathbf{e}_i, \mathbf{e}_j, \mathbf{r}^c_{ij}) & r_{ij} \le r^c \\ 0 & r_{ij} > r^c\,, \end{cases} \tag{1.18}$$

where $\mathbf{r}^c_{ij} \doteq r^c \hat{\mathbf{r}}_{ij}$.

This has become one of the most widely used continuous potentials for simulations of anisotropic fluids. The phase diagram in the density-temperature plane has been determined for a number of parametrisations [21–23]; there have also been some systematic studies of the effects on the phase diagram of the anisotropy parameters κ and κ' [24,25]. and investigations have been made of many properties, such as dynamics [26], thermal conductivity [27,28] and viscosity [29,30]. References relating to the elastic properties will be cited in chapter 3.

The model, or modified versions of it can also be used for studying uniaxial plate-like molecules [31], or biaxial systems [32]. Polymer chains can be constructed out of Gay-Berne units.

1.6 Reduced units

In common with most literature on the Gay-Berne model, throughout this thesis we use reduced units. Usually we denote these with a superscript *, for example temperature $T^* = k_B T/\varepsilon_s$, density $\rho^* = \rho\sigma_s$, and time $t^* = (\varepsilon_s/m\sigma_s^2)^{1/2} t$.

1.7 Simulation methods

In a computer simulation we aim to calculate thermodynamic averages, i.e. to compute either the ensemble average, eqn (1.1), or an average over a phase space trajectory, eqn (1.4). Broadly, Monte Carlo (MC) and molecular dynamics (MD) simulations correspond respectively to these two possibilities.

1.7.1 Monte Carlo Simulation

The Monte Carlo method was developed in the 1940s, for studying the diffusion of neutrons in fissile materials. As an efficient technique for sampling from a multidimensional probability distribution, it finds applications in many fields. The closely related *simulated annealing* method is also a very powerful technique for finding global optima in many dimensions, and we shall be making use of it in chapter 5.

There are many books and review articles dealing with MC techniques for condensed matter simulation, for example [33–36]; here we summarise the method in its simplest form, taking the canonical ensemble as an example. The aim is to calculate weighted averages over phase space of the form:

$$\langle A \rangle = \frac{\int\int \mathrm{d}\mathbf{r}\,\mathrm{d}\mathbf{p}\; A(\mathbf{r},\mathbf{p}) \exp\left[-\mathcal{H}(\mathbf{r},\mathbf{p}) \,/\, k_B T\right]}{\int\int \mathrm{d}\mathbf{r}\,\mathrm{d}\mathbf{p}\; \exp\left[-\mathcal{H}(\mathbf{r},\mathbf{p}) \,/\, k_B T\right]} \,. \tag{1.19}$$

In most cases, the Hamiltonian decouples into two independent terms, a kinetic energy quadratic in the momenta, and a potential term depending solely on the coordinates. $f(\Gamma)$ is then a product of a Gaussian momentum distribution and a configurational part. When we calculate averages of a static variable $A(\mathbf{r})$, the momentum dependence disappears, and we are left with a configuration average:

$$\langle A \rangle = \frac{\int \mathrm{d}\mathbf{r}\; A(\mathbf{r}) \exp\left[-\mathcal{V}(\mathbf{r}) \,/\, k_B T\right]}{\int \mathrm{d}\mathbf{r}\; \exp\left[-\mathcal{V}(\mathbf{r}) \,/\, k_B T\right]} \,. \tag{1.20}$$

Clearly, an estimate of $\langle A \rangle$ can be obtained by selecting n_s points uniformly from configuration space, $\{\mathbf{r}^{(1)}, \mathbf{r}^{(2)} \ldots \mathbf{r}^{(n_s)}\}$ and calculating

$$\langle A \rangle_s = \frac{\sum_{i=1}^{n_s} A(\mathbf{r}_i) \exp\left(-\mathcal{V}(\mathbf{r}^{(i)}) \,/\, k_B T\right)}{\sum_{i=1}^{n_s} \exp\left(-\mathcal{V}(\mathbf{r}^{(i)}) \,/\, k_B T\right)} \,. \tag{1.21}$$

In a dense fluid, however, most randomly chosen configurations contain molecule overlaps, and so make an exponentially small contribution to the numerator and denominator of (1.21). Convergence is therefore very slow. It would be preferable to bias the selection of points towards regions where the configuration weight $\phi^{(i)} = \exp\left(-\mathcal{V}(\mathbf{r}^{(i)}) / k_B T\right)$ is quite large. Even better would be to generate a sequence of points which samples from the actual distribution of interest, ϕ. This can be accomplished by means of a Markov process, defined by a set of transition weights $W(\mathbf{r}^{(i)} \rightarrow \mathbf{r}^{(j)})$. Configurations are generated with the desired probability distribution in the asymptotic limit - i.e. after many transitions - provided[†]

$$\frac{W(\mathbf{r}^{(i)} \rightarrow \mathbf{r}^{(j)})}{W(\mathbf{r}^{(j)} \rightarrow \mathbf{r}^{(i)})} = \frac{\phi^{(j)}}{\phi^{(i)}} \,. \tag{1.22}$$

We can think of $W(\mathbf{r}^{(i)} \rightarrow \mathbf{r}^{(j)})$ as the product of a probability $P(\mathbf{r}^{(i)} \rightarrow \mathbf{r}^{(j)})$ for "trying" a move, and the probability $\Pi(\mathbf{r}^{(i)} \rightarrow \mathbf{r}^{(j)})$ of its acceptance. Rejecting a move means that the state remains unchanged, i.e. we set $\mathbf{r}^{(i+1)} = \mathbf{r}^{(i)}$ and include the same state in the average again. There are various ways of satisfying eqn (1.22). In the frequently used Metropolis scheme [37], the trial probabilities are chosen such that

$$\frac{P(\mathbf{r}^{(i)} \rightarrow \mathbf{r}^{(j)})}{P(\mathbf{r}^{(j)} \rightarrow \mathbf{r}^{(i)})} = 1 \,, \tag{1.23}$$

and the acceptance probability

$$\Pi(\mathbf{r}^{(i)} \rightarrow \mathbf{r}^{(j)}) = \min\left(\frac{\phi^{(j)}}{\phi^{(i)}}, 1\right) \,. \tag{1.24}$$

Again, there are many ways of choosing trial moves in accordance with eqn (1.23). The most common is to select one of the particles and attempt a displacement along a random direction through a distance uniformly distributed on $[0 : \Delta]$. The length of an MC run is usually expressed in MC sweeps, which correspond to cycles of N attempted moves, one on each particle.

Besides the number of sweeps, the sampling efficiency depends on the acceptance rate for the moves, which can be tuned by altering Δ. An acceptance rate of around 50% is common (the optimal value is system-dependent).

[†]Strictly, this condition of *detailed balance* is sufficient, but it is not necessary [34].

The extension of the method to dealing with orientational degrees of freedom is quite straightforward. The acceptance criterion is unaltered - one simply introduces moves which reorient particles.

1.7.2 Molecular Dynamics

In molecular dynamics, we explicitly compute a phase space trajectory $[\mathbf{r}(t), \mathbf{p}(t)]$. The way in which this is done depends on whether one is studying hard particles or continuous potentials. For hard particle models, the dynamics consists of an ordered sequence of collisions occurring at discrete times, with free flight and/or rotation of particles between collisions. The most intensive part of the algorithm is determining whether, and when, a given pair of particles are going to collide. The simplest case, the hard sphere fluid is a useful reference for theories of liquids, and the earliest MD simulations, by Alder and Wainwright [16] were on this system. The computational cost of non-spherical hard models is usually much greater, as the time of collision equation has to be solved iteratively.

In the case of continuous potentials, the dynamics is governed by Newton's equations. There are several different schemes for integrating these equations, which are discussed in [34] and elsewhere. For all our MD work, we use the well-known "leapfrog" integration scheme. In the case of interest to us, i.e. uniaxial molecules interacting via a pairwise additive continuous potential $\mathcal{V}$, the discretised equations of motion are as follows [38]:

$$\mathbf{r}_i(t+\delta t) = \mathbf{r}_i(t) + \delta t\, \mathbf{v}_i(t+\tfrac{1}{2}\delta t) \tag{1.25}$$

$$\mathbf{v}_i(t+\tfrac{1}{2}\delta t) = \mathbf{v}_i(t-\tfrac{1}{2}\delta t) + \delta t\, \mathbf{f}_i(t)/m \tag{1.26}$$

$$\mathbf{e}_i(t+\delta t) = \mathbf{e}_i(t) + \delta t\, \mathbf{u}_i(t+\tfrac{1}{2}\delta t) \tag{1.27}$$

$$\mathbf{u}_i(t+\tfrac{1}{2}\delta t) = \mathbf{u}_i(t-\tfrac{1}{2}\delta t) + \delta t\, \left[\mathbf{g}_i^{\perp}(t)/I + \lambda(t)\mathbf{e}(t)\right] \tag{1.28}$$

Here, $\mathbf{r}_i$, $\mathbf{v}_i$, $\mathbf{e}_i$ and $\mathbf{u}_i$ are the position, translational velocity, orientation, and orientational velocity of the i^{th} particle; $\mathbf{f}_i = -\partial\mathcal{V}/\partial\mathbf{r}_i$ are the forces. $\mathbf{g}_i^{\perp}$ is the component perpendicular to $\mathbf{e}_i$ of the "gorque" $\mathbf{g}_i = -\partial\mathcal{V}/\partial\mathbf{e}_i$. [†] Finally, $\lambda(t)$ is a Lagrange

[†]This is simply related to the torque: $\tau_i = \mathbf{e}_i \times \mathbf{g}_i$.

multiplier, introduced to constrain the orientation vectors $\mathbf{e}_i$ to be of unit length (we shall give more details on the calculation of λ in chapter 3, when we discuss our director constraint algorithm). Good energy conservation can be obtained with this integration scheme, provided the timestep δt is reasonably small.

1.7.3 Boundary conditions

The system sizes studied in computer simulations are quite modest, of the order of hundreds or thousands of molecules. In an open system of this size, surface effects would be very important - for example in a cube of $10 \times 10 \times 10$ particles, some 50% are on the surface. In order to measure bulk properties, we eliminate all surfaces by means of periodic boundary conditions, which can be envisaged as filling space with periodic images of the basic simulation cell. Both the calculation of forces and update of particle positions are affected:

- The potential (and force, in MD) between a pair of particles is calculated as if between their minimally separated periodic images.
- At the end of each MD timestep or MC sweep, particles which have left the basic cell are "reboxed".

Variants of this technique can be used to place various static or dynamical constraints on the system, for example to study shear flow [39] or liquid crystals subject to an imposed twist. The latter technique forms the basis of the simulations described in chapter 5.

1.7.4 MC versus MD

MD has several advantages, beyond its ability to measure dynamic quantities such as time correlation functions. One is the ease with which constraints can be built into the equations of motion. The "dynamics" in MC usually consists of a set of moves which operate on a single particle, whereas the constraint equations often involve collective properties. Implementing these kind of constraints in MC usually means over-constraining the single-particle moves, which leads to poor sampling

of phase space. Nevertheless, there are situations in which MC is preferred. For example, in the "real" dynamics of polymers, the timescale for reptation (motion of the whole chain) is much longer than that associated with microscopic motion of the constituent monomers. In MD, the simulation timestep is set by this fast motion, and so very long runs are required to sample the chain conformations adequately. Configuration bias Monte Carlo (CBMC) [35] attempts to overcome this problem by means of reptation-like moves, which traverse phase space more rapidly whilst still sampling the same ensemble.

In this thesis we shall be concerned only with single-site models, for which the problem of competing timescales does not arise (at least, not at the molecular level), and so CBMC techniques are not applicable - although they were the inspiration for the annealing moves we use in chapter 5. We make extensive use of parallel algorithms, especially for our study of the twist grain boundary phase. In our measurement of the elastic constants, we impose a constraint on the nematic director, a collective property. Although we employed MC for some of our equilibration runs, these considerations led us to use MD in most cases.

1.8 Practicalities

1.8.1 Simulation and analysis codes

Some of our work was carried out on Silicon Graphics or DEC Alpha workstations, using serial MD code developed by the author. These codes use standard techniques [34] such as linked lists and Verlet neighbour lists for computational efficiency. We also made use of these machines for much of the data analysis. However, for the bulk of the simulations we used parallel codes (see chapter 2) running on the t3d machines at Edinburgh and Bologna, and the SP2 machine at Daresbury Laboratory. Most of the analysis for chapter 5 was done on the YMP and J90 supercomputers at Edinburgh Parallel Computing Centre, with a certain amount carried out on departmental and university computers at Bristol. For transferring binary data between these machines, we used the NCSA hierarchical data format [40] libraries.

1.8.2 Visualisation

The ultimate aim of simulation is to describe the behaviour of a system numerically. Nevertheless, graphical representations of molecular configurations often provide valuable insight into the formation and evolution of the structure. This is especially true when studying phases with complex geometry, such as the TGB phase. Configuration snapshots appearing in this thesis were produced with our own molecular graphics (MG) software, illustrated in figure 1.3. This software, which runs on a variety of workstations and PCs, consists of a set of routines for producing depth-cued, shaded images of collections of points, lines, spheres, spherocylinders and ellipsoids. Object attributes - shape, colour, size, position and orientation - are initialised with a set of Fortran subroutine calls, making the routines versatile and easy to use. The viewing direction and other parameters can be adjusted interactively, and there are also facilities for displaying slices through the configuration. The rendered image can be output in various file formats, including postscript. The MG routines are widely used within our group, and may be downloaded from the World Wide Web [41].

Figure 1.3: The molecular graphics visualisation program, MG.

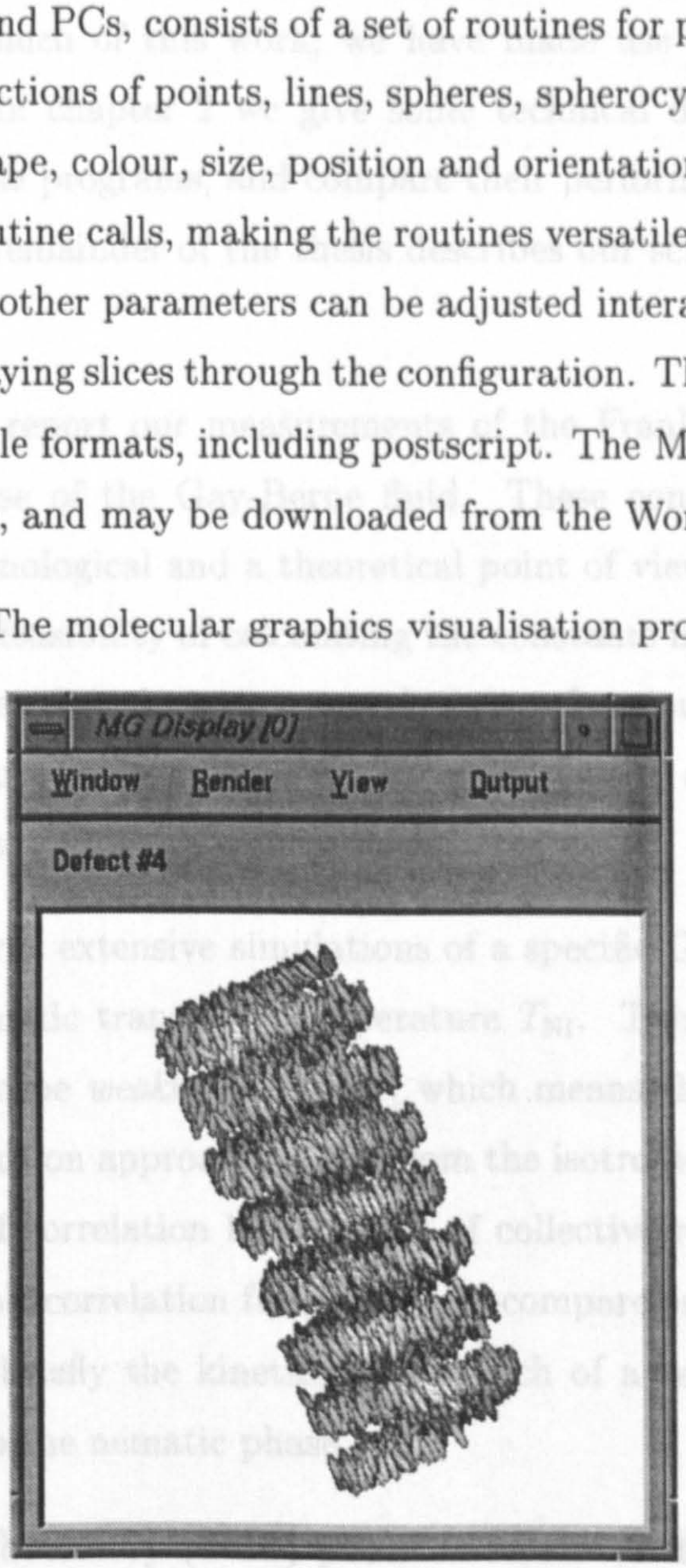

1.9 Scope of this thesis

In this thesis, we investigate several aspects of liquid crystalline behaviour, using the Gay-Berne model. As noted above, much is already known about the single-particle and intermediate-scale aspects of this model, and its phase diagram is well known. Rather than extending this work, we concentrate on three topics for which large scale simulations are required, namely calculation of elastic constants, pretransitional behaviour and ordering dynamics in the nematic-isotropic transition, and twisted smectic phases. For much of this work, we have made use of parallel molecular dynamics programs. In chapter 2 we give some technical details of the parallel algorithms used in these programs, and compare their performance for the systems of interest to us. The remainder of the thesis describes our scientific results, and is structured as follows:

- In chapter 3 we report our measurements of the Frank elastic constants in the nematic phase of the Gay-Berne fluid. These constants are important both from a technological and a theoretical point of view. In this chapter we demonstrate the feasibility of calculating the constants in molecular dynamics simulations, assess the advantages or otherwise of various measurement techniques, and compare our results with published figures obtained via different simulation routes, and experimental values.

- Chapter 4 concerns extensive simulations of a specific Gay-Berne model near the isotropic-nematic transition temperature T_{NI}. This transition is known experimentally to be *weakly* first order, which means that marked pretransitional effects occur on approaching T_{NI} from the isotropic side. We investigate the divergence of correlation lengths and of collective reorientation times by measuring suitable correlation functions, and compare our results with theory. We also discuss briefly the kinetics of a quench of a very large system from the isotropic into the nematic phase.

- The twist grain boundary (TGB) phase discussed in chapter 5 has been the subject of much investigation since its theoretical prediction and experimental

discovery in 1989. We have carried out large scale simulations of a particular parametrisation of the Gay-Berne model which is known to exhibit a smectic A phase. By applying twisted boundary conditions, we mimic the effect of placing an experimental sample in a twist cell. We define suitable quantities for characterising the structure seen in our simulations; their behaviour is consistent with the structure of the TGB phase. We develop a novel technique, based on simulated annealing, which is able to locate the topological defects which are predicted to occur in the TGB phase. Applying this technique to our configurations, we confirm that these defects are present, and that their distribution is in qualitative agreement with theoretical predictions.

Chapter 2

Parallelisation Techniques for Molecular Dynamics

2.1 Introduction

In the past two decades, the speed of single-processor machines has increased dramatically, and workstations are now capable of millions of floating point instructions per second. Recently however, this upward trend in computational power has begun to slow down, and for intensive calculations the emphasis has shifted towards parallel architectures. A number of high performance parallel machines are available in the UK for scientific research, notably the Cray t3d at Edinburgh, and much effort has gone in to finding efficient techniques for the parallelisation of numerical algorithms. In this chapter we will briefly discuss different types of parallel machine, and strategies for parallelisation of serial codes. Next we summarise the criteria which should be used to evaluate the efficiency of a parallel program. There follows a description of the parallel molecular dynamics codes which we have used for many of our simulations. Some of these programs were written by the present author, with valuable assistance from Dr W.Smith of Daresbury Laboratory; others were written as part of the High Performance Computing Initiative consortium "Simulation and Statistical Mechanics of Complex Fluids". The authorship of these programs is as follows:

Dr. W. Smith	Daresbury Laboratory	`MDMEGA` program for LJ atoms
Dr. M. R. Wilson	Durham University	`PVM` harness
Mr. A. Sauron	Sheffield Hallam University	
Dr. M. P. Allen Mr. M. A. Warren	Bristol University	`GBMEGA` and `GBMESO` code

2.2 Types of parallel architecture

A parallel machine consists of several, sometimes many, processors, with some means of communication between them. It is useful to classify parallel computers according to two criteria. The first concerns the distribution of memory among the nodes. On *single data* machines, the same physical memory is addressable by all the processing elements (nodes). This common memory can be used for internode communication. In contrast, on *multiple data* machines, some or all of the memory is the preserve of the node to which it is attached. If all the memory is *distributed* in this way, then dedicated communication links are needed to pass data between nodes.

Secondly, parallel machines are differentiated according to how instructions are distributed to the processing elements (nodes). On *single instruction* machines, there is just one program, and at each instruction cycle, the same operation is broadcast for execution on all nodes. The only autonomy nodes have in the execution of instructions is through the use of a mask, an array of logical values associated with each node: certain simple operations can be executed on the subset of nodes for which the mask is set. The DAP is a good example of such a machine. On multiple instruction machines, there is no such restriction, as the program runs independently on each node. In some cases, one can even run a completely different executable on each node.

Parallel machines are increasingly of the multiple instruction, multiple data (MIMD) type, since this architecture is cost-efficient to build and extend, and allows for more flexibility in the design of parallel algorithm. It is also more convenient for multiuser systems, as several jobs can be run simultaneously, each using a portion of the available processors. Both the Cray t3d and IBM SP2 fall into this category.

2.3 Parallel algorithms for MD

2.3.1 General considerations

The most important criterion for judging a parallel algorithm is the speedup on n processors compared with its single-node performance. Ideally, one would like the execution time to be inversely proportional to n; in practice this is rarely achieved, except on MIMD machines in the trivial case of *task farming*. The latter consists of treating the machine as a set of completely independent computers, and running independent simulations on each one. This method can be useful for condensed matter simulation, especially for surveys of the phase diagram. In the present work, however, we are more interested in simulations of a large system at a small number of state points. Methods other than task farming involve dividing the problem among processors and some degree of communication between them, which introduces the following sources of inefficiency:

- Duplication of work; in some cases the same calculation is performed on several nodes, especially in replicated data programs (see below).
- Uneven load balancing, which results in some processors lying idle whilst awaiting a result from another node.
- Communication overheads. These depend on the *latency* time (the startup time for sending a message, before any data is transmitted), and the bandwidth.

On MIMD machines, there are two ways of organising the data, which define two approaches to parallelisation, namely *replicated data* and *data parallel* methods. The programs `GBMESO` and `GBMEGA` use these two techniques respectively, and are described below.

2.3.2 Replicated data method: GBMESO

The term replicated data (RD) simply means that whilst the computational effort is distributed among the nodes in some way, a copy of the data structures describing

the state of the entire system is maintained on every node. Some parts of the calculation may be done on the same data on all nodes simultaneously. This may seem an unattractive proposition, especially on a machine with distributed memory. However, for many serial programs, the bulk of the computation time is spent in a few sections of code (see table 2.1). With the RD technique, we concentrate on parallelising these, and leave the remainder in serial form. The way in which the expensive calculations are parallelised will vary from case to case, but always involves dividing the work equally among the nodes in some way, and then using internode communications to distribute the results so that all nodes have all the data ready for the next stage of the calculation. As the number of nodes is increased, the communication costs involved in broadcasting data to all nodes, and the duplication of work in unparallelised sections, lead eventually to inefficient CPU usage. Also, by definition, the method is inefficient in its use of memory, and this often imposes a limit on the size of problem that can be tackled. Two major advantages of this kind of approach are that it is comparatively straightforward to parallelise an existing serial code in this way - the process is one of gradual modification rather than rewriting from scratch - and that serial and parallel versions of the program can be maintained alongside each other.

Table 2.1: Typical CPU usage in various sections of a serial MD program The timings shown are for a Gay-Berne simulation with a Verlet neighbour list, running on a DEC Alpha workstation. This workstation code also calculates certain properties related to the elastic constants (see chapter 3) during the simulation. Our parallel codes simply store configurations on disc for later analysis.

Task	Percentage of total CPU time
Force calculation, no list update	70.9
Force calculation with list update	14.8
Calculation of order tensor fluctuations	11.4
Leapfrog integration algorithm	1.2
Other	1.7

From table 2.1, we can see that the obvious candidate for parallelisation is the force calculation. The generation of the Verlet neighbour list involves checking for pairs within cutoff, $|\mathbf{r}_j - \mathbf{r}_i| < r^c$; $i, j = 1 \cdots N$. This all pairs calculation is distributed among the nodes, using the scheme of Brode and Ahlrichs [42]. In this scheme, "i" molecules are assigned to each processor in turn. For each of its i's, each node then checks molecules $j \in \{\overline{i}, \overline{i+1} ... \overline{i+N_{\mathrm{max}}}\}$, where

$$N_{\mathrm{max}} = \begin{cases} [N/2] & \text{odd } i \\ N/2 & \text{even } i,\ i > N/2 \\ N/2 - 1 & \text{even } i,\ i \leq N/2\,, \end{cases} \tag{2.1}$$

Here, the operation $[\cdots]$ denotes integer truncation, and

$$\overline{x} \equiv \begin{cases} x & x \leq N \\ x - N & x > N\,. \end{cases} \tag{2.2}$$

Once the Verlet list has been compiled, each particle goes through its (i, j) pairs and accumulates forces in the usual way:

```
foreach (i, j) {
    f_i ← f_i + f_ij
    f_j ← f_j − f_ij          (and similarly for the "gorques" g_i)
},
```

Global sums are used to calculate the total forces and gorques, ensure that these are distributed to all nodes, and to compute the total potential energy and virial. The forces are used to update the full set of particle positions and velocities independently on *all nodes*. No attempt is made to parallelise this part of the algorithm.

2.3.3 Data parallel method: GBMEGA

As the name suggests, in data parallel (DP) methods the data is distributed among the nodes. In many problems, this is done by partitioning the system into spatial domains. Domain decomposition is particularly efficient in the case of lattice models, where the rules which evolve the system from time t to $t + 1$ are *local*. In this case,

each domain can be updated almost independently of the others, the only external data required being the state of lattice sites in a narrow border region surrounding the domain. This same idea is used in the domain decomposition molecular dynamics program, GBMEGA . Briefly, this works as follows:

- The system is partitioned into cuboidal domains, of sides (l_x, l_y, l_z). Each domain is assigned to a node. Nominally, only the coordinates and velocities of particles lying within that domain are held on the node.

- In order to compute the forces on the particles within a given domain, the coordinates of the particles within the cutoff distance r^c of the domain must be imported. Assuming that $\min\{l_x, l_y, l_z\} > r^c$, only *neighbouring* nodes need to exchange coordinate data. This is accomplished by six communication steps, which transfer information in the $-x$, $+x$, $-y$, $+y$, $-z$ and $+z$ directions, as illustrated in figure 2.1.

- The forces on the domain's particles are calculated using a link cell algorithm, which speeds up the check for pairs within cutoff.

- Each node updates the coordinates and velocities of the particles in its domain - the border particles are now redundant.

- Each node *exports* any particles which have gone outside its domain to neighbouring nodes. The code to do this is very similar to that used for importing particles, except that in this case the particles' translational and orientational velocities are also exported.

Extensions to basic domain decomposition program

Partitioning into domains of equal size is appropriate for simulation of homogeneous systems. However, inhomogeneities in density can lead to poor load balancing. A general solution to this problem is rather difficult to develop, but this is not always necessary. For example, simulations of smectic vapour coexistence are often conducted in a slab geometry, so that the density varies only along one of the box

Figure 2.1: One of the communication steps used in the GBMEGA program to import particle coordinates into the domain border region. In the step illustrated, node (i, j, k) communicates the coordinates of all the particles which lie in the left-most r^c-wide strip of its domain to its neighbour $(i-1, j, k)$; it then waits to receive coordinates from node $(i+1, j, k)$, which belong in the border region to the right. This step is carried out simultaneously on all nodes. The sequential execution of this and five similar steps for the other directions ensures that all border particles, including ones in the corners, are correctly imported.

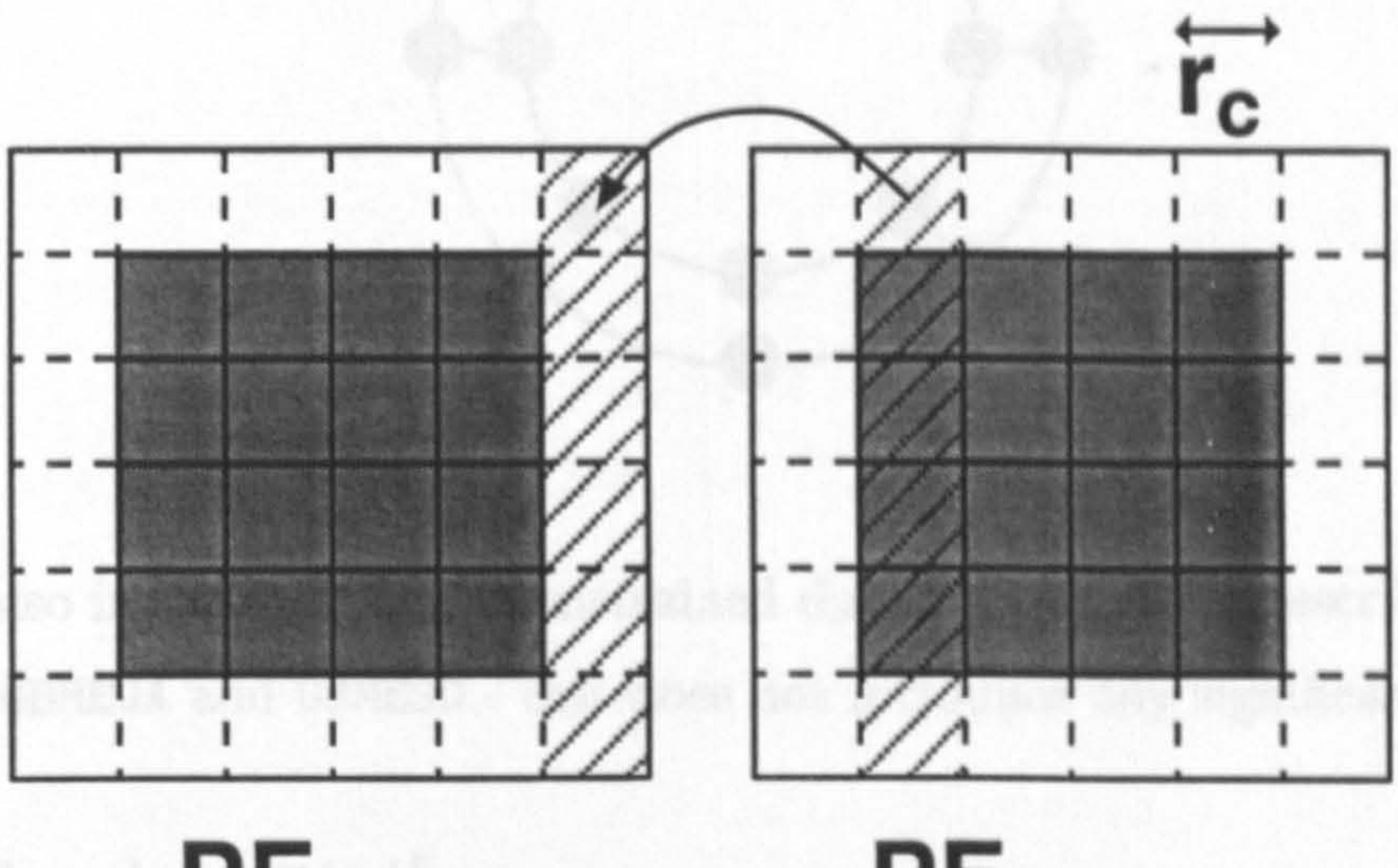

axes. We developed a modified version of GBMEGA for this case. The domain widths are allowed to vary dynamically such that each domain contains approximately the same number of particles (subject to the constraint that all domain sides remain longer than r^c). Though not used in this thesis, this version of the program has been employed by other members of our group [25].

In our study of the twist grain boundary phase we make use of *twisted periodic boundary conditions* (see chapter 5). Within GBMEGA , these are implemented by means of modified *import* and *export* routines, which apply a $\pm\frac{\pi}{2}$ rotation to particles transferred between the domains at the $\pm z$ ends of the simulation cell. We also change the map which defines the connectivity between neighbouring domains.

Figure 2.2: The distribution of the force calculation in the SIMD algorithm. The inner ring represents the stationary arrays; the outer one the travelling coordinates and forces. On each iteration the travelling coordinates are cycled in the sense shown.

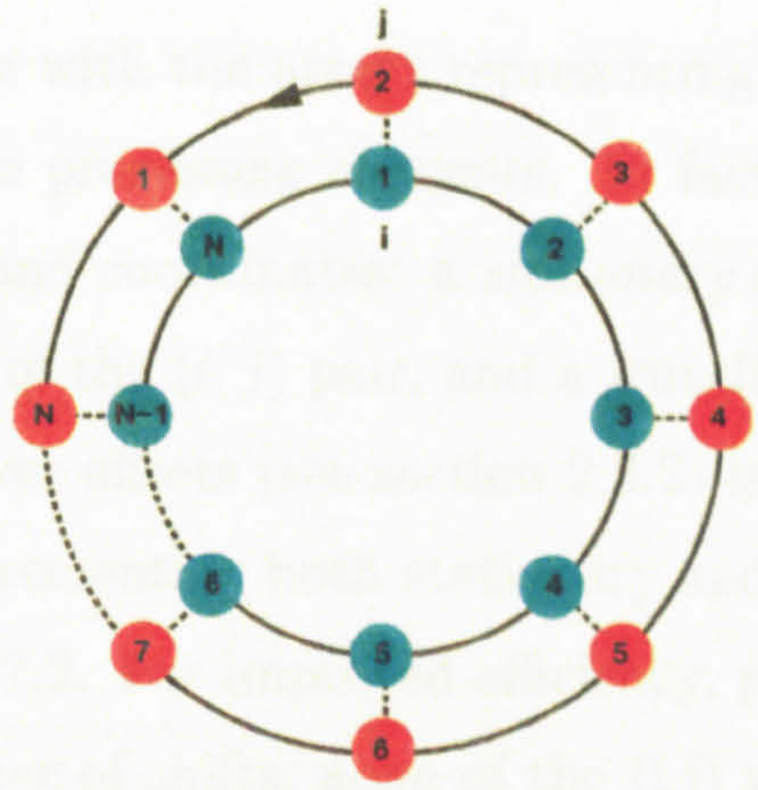

We have also implemented the constrained director mechanics described in chapter 3 in both GBMEGA and GBMESO - this does not introduce any significant overheads.

2.3.4 Implementation

Both of these t3d codes are based on a *harness* which provides a set of high-level routines for message passing and calculating global sums. Originally, the motive for this approach was to facilitate porting of the existing MDMEGA code for Lennard-Jones atoms, which was written for the iPSC supercomputer; the harness emulates the native parallel operations of this machine. Another advantage is that these routines are easier to use than the low-level PVM calls on which the harness is based. Originally PVM was the only message passing library available on the Cray t3d. The harness has now been ported to use the MPI calls - this version is slightly faster. On the IBM SP2, the PVM version is still used.

2.3.5 A parallel algorithm for SIMD architectures

Some of the elastic constant work for chapter 3 was carried out on the distributed array of processors (DAP) at Bristol. This machine differs from the Cray in that it has a large number of rudimentary processors ($n = 1024$), and is a single instruction multiple data (SIMD) machine. On the DAP, we made use of the Brode-Ahlrichs decomposition, but this time with the arrays representing particle coordinates and forces distributed among the processing elements. In fact, there are two separate distributed arrays of forces and coordinates: a *stationary* set of $\mathbf{r}, \mathbf{e}, \mathbf{f}, \mathbf{g}$ which correspond to the "i" molecule of the (i, j) pair, and a *travelling* set which correspond to molecule "j". The sum over offsets (see section 2.3.2) is done by circularly shifting the travelling arrays, incrementing both stationary and travelling forces at each step, as illustrated in figure 2.2. For improved efficiency, particles are sorted on r_z, so that after a certain number of shifts, none of the (i,j) pairs are within cutoff; it is then not necessary to take the offset all the way up to $N_{\mathbf{max}}$.

2.3.6 Performance of RD and DP algorithms

From tables 2.2 and 2.3, it is evident that the domain decomposition program scales very well with number of processors, especially for large system sizes where there are relatively fewer particles in the border regions. For small system sizes and smaller numbers of nodes, replicated data works well. It is perhaps worth noting that replicated data would be a much more favorable strategy for dealing with long range potentials. More detailed discussion of the algorithms and their performance can be found in [43]. For our present purposes, we simply observe that for the the large system sizes (generally $N > 8000$), and short ranged Gay-Berne potential studied in this thesis, `GBMEGA` was clearly the preferred choice.

Table 2.2: Timings (expressed in elapsed seconds per timestep) for the replicated data program GBMESO, running on the Cray t3d. Each of these test runs consisted of 100 timesteps of NVE MD on a cubic box of Gay-Berne particles in the nematic phase. The potential parameters were $\kappa = 3$, $\kappa' = 5$, $\mu = 2$, $\nu = 1$. Other parameters were as follows: radial cutoff $r^c = 4.0\sigma_0$, Verlet list radius $r^v = 4.4\sigma_0$, density $\rho^* = 0.32$, temperature $T^* = 1.00$, and integration timestep $\delta t = 0.0015$.

Number of particles	Number of nodes	CPU time	
(N)	(n)	Total	Integration
256	8	0.028	0.004
2048	4	0.588	0.030
2048	8	0.324	0.032
2048	16	0.195	0.035
2048	32	0.138	0.039
2048	64	0.113	0.044
16384	8	6.039	0.272
16384	16	3.298	0.294
16384	32	1.972	0.330
16384	64	1.348	0.368
16384	128	1.158	0.449

Table 2.3: Timings (expressed in elapsed seconds per timestep) for the domain decomposition program GBMEGA. The run parameters were exactly as in table 2.2.

Number of particles	Number of nodes	CPU time	
(N)	(n)	Forces	Other
256	8	0.058	0.0101
2048	32	0.105	0.0127
2048	64	0.061	0.0133
16384	8	2.712	0.0653
16384	16	1.431	0.0312
16384	32	0.748	0.0220
16384	64	0.395	0.0187
16384	128	0.225	0.0203
64000	8	8.895	0.1705
64000	16	4.818	0.0921
64000	32	2.685	0.0520
64000	64	1.448	0.0366
64000	128	0.740	0.0266
64000	256	0.409	0.0247

Chapter 3

Calculation of Frank Elastic Constants in the Nematic phase

3.1 Introduction

In a nematic liquid crystal, the distribution of molecular positions is translationally invariant but the orientational distribution shows preferential alignment along the director. Deviations from uniform alignment occur principally through the existence of defects (for example, the disclination lines or threads which give the phase its name) and through the equilibrium, temperature-driven fluctuations which are resisted by elastic restoring forces.

The continuum elastic theory of director fluctuations is based on Frank's expression [44] for the free energy increase, $\Delta\mathcal{F}$, as a function of gradients of the director field:

$$\Delta\mathcal{F} = \frac{1}{2}\int \mathrm{d}\mathbf{r}\left\{K_1\left[\nabla\cdot\mathbf{n}(\mathbf{r})\right]^2 + K_2\left[\mathbf{n}(\mathbf{r})\cdot(\nabla\times\mathbf{n}(\mathbf{r}))\right]^2 + K_3\left[\mathbf{n}(\mathbf{r})\times(\nabla\times\mathbf{n}(\mathbf{r}))\right]^2\right\}. \tag{3.1}$$

The parameters K_1, K_2 and K_3 in eqn (3.1) are the splay, twist and bend Frank elastic constants respectively, and the associated squared terms correspond to the three distinct kinds of deformation of the director field $\mathbf{n}(\mathbf{r})$ depicted in figure 3.1. As well as determining the relaxation of long-wavelength director field inhomogeneities, the Frank constants influence the shapes of disclination defects [44], play a role in

nematodynamic flow [45], and determine the extent to which liquid crystals transmit torques and respond to applied fields [3,46]. Since the last two of these are the main properties exploited in liquid crystal displays and switching devices, it is important to be able to relate them to the properties of the constituent molecules. There is also intrinsic interest in studying these quantities in the vicinity of the nematic-isotropic and nematic-smectic phase transitions.

Figure 3.1: The three distinct elastic deformations in a uniaxial nematic liquid crystal.

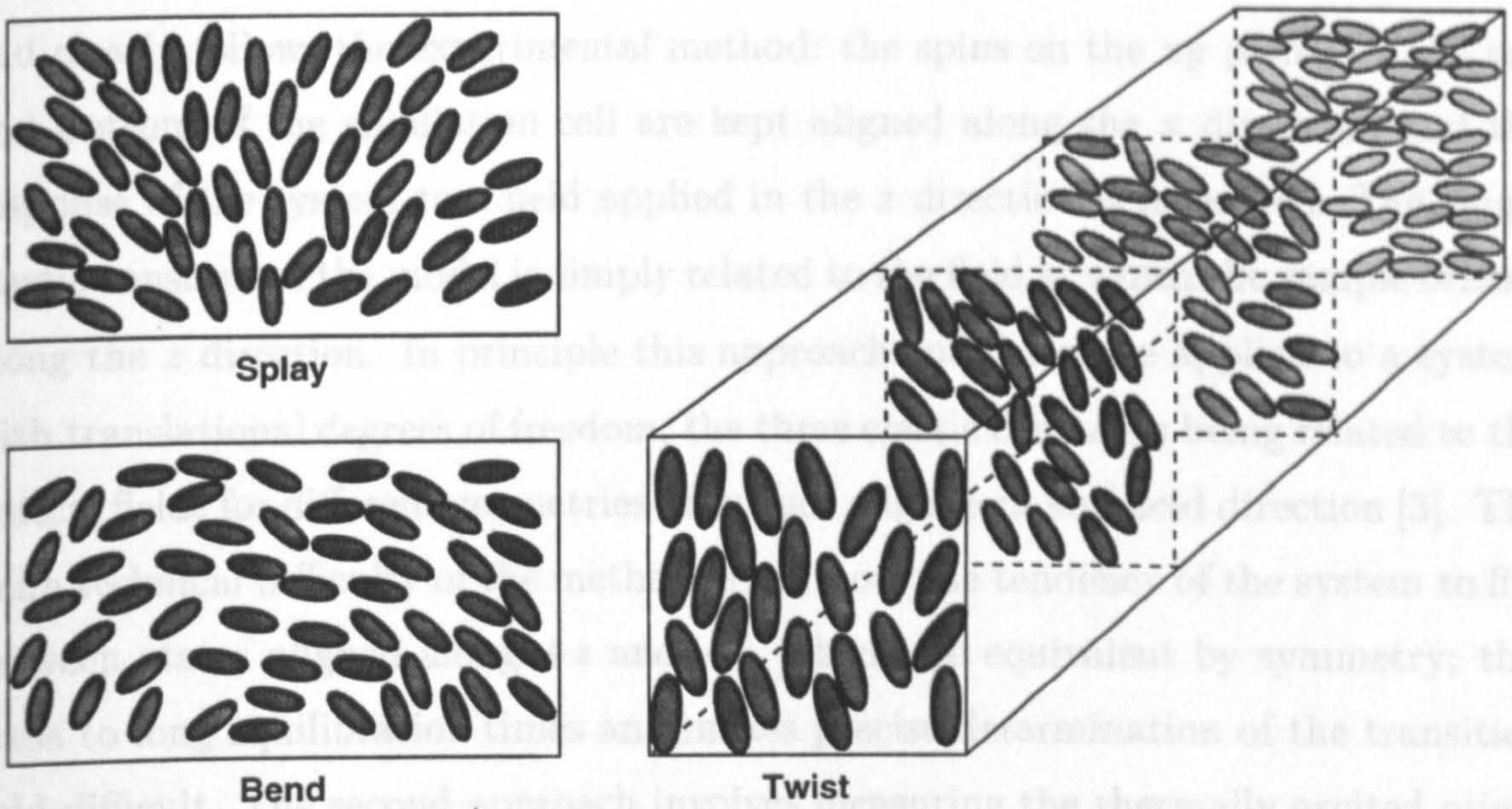

Various experimental techniques have been developed to determine the Frank constants. Observation of the Freedericksz transition [47], in which a sample is subjected to competing bulk and surface-aligning fields, and a phase transition observed to occur at a critical field, together with a continuum elastic theory [48,49], is one well-known route. Such experiments may be combined with the measurement of various optical [50–52] and other [52,53] properties. Quasielastic Rayleigh scattering in the presence of fluctuation-quenching fields [54] is another route, and the twist constant K_2 has been obtained by direct torque measurements [55].

Computer simulation provides a method of calculating the Frank constants for

simplified molecular models, and hence of shedding some light on the basic relationship with molecular structure. However, because the Frank free energy is only valid for slowly-varying director fields (i.e. for long wavelength perturbations) it is necessary to use reasonably large sample sizes: almost all practicable methods for estimating K_1–K_3 rely on extrapolating to low wavevector. At these low wavevectors, the orientational correlation functions decay relatively slowly, and so it in order to obtain reliable results it is also necessary to conduct reasonably long simulations.

An extensive study of the elementary Lebwohl-Lasher spin model [56], using systems of over 32000 lattice sites, compared three different techniques for calculating Frank elastic constants. The first of these is based on the Freedericksz transition, and closely follows the experimental method: the spins on the xy planes at the top and bottom of the simulation cell are kept aligned along the x direction, and the response of the system to a field applied in the z direction is measured. The single elastic constant of the model is simply related to the field at which the sample orients along the z direction. In principle this approach could also be applied to a system with translational degrees of freedom, the three elastic constants being related to the critical fields for different geometries of surface alignment and field direction [3]. The main technical difficulty of the method arises from the tendency of the system to flip between states aligned along $+z$ and $-z$, which are equivalent by symmetry; this leads to long equilibration times and makes precise determination of the transition field difficult. The second approach involves measuring the thermally excited orientational fluctuations. At low wavevector these fluctuations are quadratic in k, and the magnitude of fluctuations associated with each distortional mode can be used to calculate the corresponding elastic constant. The third method consists of perturbing the system with a sinusoidally varying orienting field of specific wavenumber. The linear response to this field is proportional to the orientational fluctuations at that wavenumber [57], and thus the dependence of the response on k is another route to K_1–K_3. The conclusions of [56] were that the Freedericksz transition method was insufficiently accurate to be useful in calculating the elastic constants, and that of the perturbed-system and fluctuation methods, the latter was more cost-effective, by virtue of giving information for a large number of wavevectors at once.

Prior to this, attempts had been made to calculate elastic constants for systems of freely rotating and translating molecules modelled as hard ellipsoids and spherocylinders [58–60]. In all cases the orientational fluctuation method was used. Typical system sizes were in the range $125 \leq N \leq 600$. Clearly, far fewer low values of k are available than for the large systems used in the Lebwohl-Lasher simulations, and this limited the accuracy of the results: probably the estimates of K_1–K_3 for these systems are reliable to about 15%. Some evidence was obtained that the dependence of orientational fluctuations on system size seemed not to be very serious [61], but the desirability of extending system sizes from a few hundred molecules to at least a few thousand was clear.

In this chapter we carry out such a programme, studying the well-known Gay-Berne molecular model in two parametrizations, for which state points in the nematic liquid crystal phase are well established, and using significantly larger system sizes than previously possible. The details of the molecular model are set out in section 3.2. We employ the method of studying equilibrium orientational fluctuations as a function of wave-vector **k**, and we review the theory of this approach in section 3.3. It is convenient, for the purposes of analysis, to fix the nematic director orientation in the simulation box, and to do this we use a constraint technique described in section 3.4. The method we use to analyze the orientational fluctuation data is explained in section 3.5. We present our simulation results in section 3.6 and draw some conclusions in section 3.7.

3.2 Gay-Berne model

We have already introduced the Gay-Berne model in section 1.5. As originally proposed [20], the potential parameters are $\kappa = 3$, $\kappa' = 5$, $\mu = 2$, $\nu = 1$. This system has been studied by various groups [62,63]; the phase diagram as a function of temperature and density has been determined [22,64–66], and the potential seems to give rise to isotropic, nematic and smectic B liquid crystal phases, as well as vapour and, presumably, solid phase(s) of unknown extent. Zannoni and co-workers [23] have studied the system $\kappa = 3$, $\kappa' = 5$, $\mu = 1$, $\nu = 3$. This gives rise to isotropic,

Figure 3.2: The two cut and shifted Gay-Berne potentials used in this chapter.

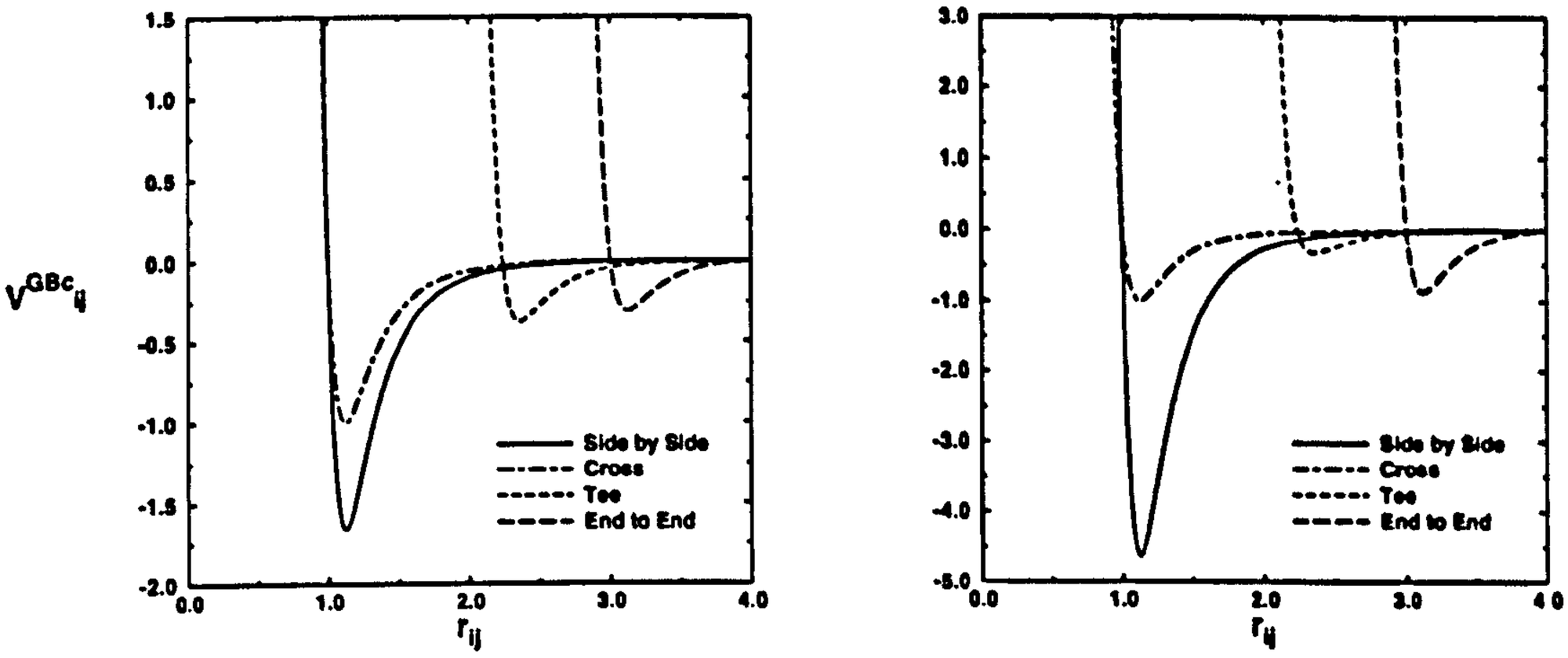

$\kappa = 3,\ \kappa' = 5,\ \mu = 2,\ \nu = 1$ $\qquad$ $\kappa = 3,\ \kappa' = 5,\ \mu = 1,\ \nu = 3$

nematic and smectic phases, and it seems that the nematic range is wider than in the case of some other models. Figure 3.2 shows the behaviour of the potentials as a function of radial separation, for several different relative orientations of the molecules. We conducted simulations at various state points in the nematic phases of these two different parametrisations.

3.3 Theoretical background

We define the ordering tensor in reciprocal space, in terms of the orientation vectors $\mathbf{e}_i = (e_{ix}, e_{iy}, e_{iz})$ of each molecule i (again, for simplicity we consider only uniaxial molecules):

$$\hat{Q}_{\alpha\beta}(\mathbf{k}) = \frac{V}{N} \sum_{i=1}^{N} \frac{3}{2} \left(e_{i\alpha} e_{i\beta} - \tfrac{1}{3}\delta_{\alpha\beta} \right) \exp(\mathrm{i}\mathbf{k} \cdot \mathbf{r}_i) \,. \tag{3.2}$$

Here $\delta_{\alpha\beta}$ is the Kronecker delta and $\alpha, \beta = x, y, z$. This is the Fourier transform of the real-space orientation density

$$Q_{\alpha\beta}(\mathbf{r}) \equiv \frac{1}{V} \sum_{\mathbf{k}} \hat{Q}_{\alpha\beta}(\mathbf{k}) \exp(-i\mathbf{k}.\mathbf{r}). \tag{3.3}$$

In an unperturbed system the orientation density is independent of position:

$$\langle \mathbf{Q}(\mathbf{r}) \rangle = \langle \mathbf{Q} \rangle = \langle \hat{\mathbf{Q}}(\mathbf{k} = 0) \rangle / V = \text{constant}. \tag{3.4}$$

The order parameter $\overline{P_2}$ is the highest eigenvalue of $\langle \mathbf{Q} \rangle$, and the director $\mathbf{n}$ is the corresponding eigenvector, as discussed by Zannoni [67]. $\overline{P_2} = \langle P_2(\cos\theta_i) \rangle$ is the average of the second Legendre polynomial of the cosine of the angle between $\mathbf{e}_i$ and $\mathbf{n}$. We may define an axis system [1], [2], [3], in which $\langle \mathbf{Q} \rangle$ is diagonal with $\mathbf{n} = (0, 0, 1)$ and

$$\begin{aligned} \langle Q_{11} \rangle = \langle Q_{22} \rangle &= -\tfrac{1}{2}\overline{P_2} \\ \langle Q_{33} \rangle &= \overline{P_2} \end{aligned}$$

provided the phase is genuinely uniaxial. In all of these expressions, angle brackets $\langle \ldots \rangle$ and the overline both indicate equilibrium ensemble averages.

Static orientational fluctuations are described in terms of $\hat{\mathbf{Q}}$, expressed in this coordinate system [8]:

$$\left\langle \hat{Q}_{13}(\mathbf{k}) \hat{Q}_{13}(-\mathbf{k}) \right\rangle \equiv \langle |\hat{Q}_{13}(\mathbf{k})|^2 \rangle = \frac{\frac{9}{4}\overline{P}_2^2 V k_B T}{K_1 k_1^2 + K_3 k_3^2} \tag{3.5}$$

$$\left\langle \hat{Q}_{23}(\mathbf{k}) \hat{Q}_{23}(-\mathbf{k}) \right\rangle \equiv \langle |\hat{Q}_{23}(\mathbf{k})|^2 \rangle = \frac{\frac{9}{4}\overline{P}_2^2 V k_B T}{K_2 k_1^2 + K_3 k_3^2} \tag{3.6}$$

where the wave-vector $\mathbf{k} = (k_1, 0, k_3)$ is chosen in the 13 plane. Just as the elastic constants are defined for long-wavelength director fluctuations, so the above equations are valid only in the limit of small k. In practical applications, it is necessary to extrapolate to $k = 0$. To extract the elastic constants from these expressions, one may fit

$$\mathcal{W}_{13}(k_1, k_3) \equiv \frac{\frac{9}{4}\overline{P}_2^2 V k_B T}{\langle |\hat{Q}_{13}(\mathbf{k})|^2 \rangle} \longrightarrow K_1 k_1^2 + K_3 k_3^2 \qquad \text{as } k \to 0 \tag{3.7}$$

$$\mathcal{W}_{23}(k_1, k_3) \equiv \frac{\frac{9}{4}\overline{P}_2^2 V k_B T}{\langle |\hat{Q}_{23}(\mathbf{k})|^2 \rangle} \longrightarrow K_2 k_1^2 + K_3 k_3^2 \qquad \text{as } k \to 0 \tag{3.8}$$

to functions of k_1^2 and k_3^2, and extrapolate to $k \to 0$. Clearly, taking the low-k limit is the crucial part of this process, and it is essential to have a large enough simulation box size L to guarantee that $\mathcal{W}_{13}(k_1, k_3)$, $\mathcal{W}_{23}(k_1, k_3)$ depend quadratically on k in the regime $k \geq 2\pi/L$.

Another expression for the Frank elastic constants [68, 69] involves the direct correlation function $C(i, j)$:

$$\left\{ \begin{array}{c} K_1 \\ K_2 \\ K_3 \end{array} \right\} = \frac{1}{2}\rho^2 k_B T \int \mathrm{dr}_{ij}\mathrm{de}_i\mathrm{de}_j \; C(i,j) \left\{ \begin{array}{c} (r_{i1} - r_{j1})^2 \\ (r_{i2} - r_{j2})^2 \\ (r_{i3} - r_{j3})^2 \end{array} \right\} e_{i1} e_{j1} f'(e_{i3}) f'(e_{j3}). \quad (3.9)$$

Here again the director $\mathbf{n} = (0, 0, 1)$ is chosen to lie in the z-direction. $f(e_{i3}) \equiv f(\cos\theta_i)$ is the single-particle orientational distribution function (θ_i being the angle between $\mathbf{e}_i$ and $\mathbf{n}$) and f' is its derivative with respect to its argument. The direct correlation function $C(i, j) = C(\mathbf{r}_{ij}, \mathbf{e}_i, \mathbf{e}_j)$ is of fundamental importance in liquid state theory, and can be written as a functional derivative of the free energy, but it cannot be measured directly by experiment or in simulation. However, the equation above does emphasize that, in measuring the K_1–K_3 we are learning something about the behaviour of $C(i, j)$ in the nematic phase. Note that these expressions are exactly equivalent to the fluctuation expressions given earlier; see, for example, the work of Somoza and Tarazona [70]. Recently, it has proved possible to extract $C(i, j)$ from simulation results by inverting the defining Ornstein-Zernike relation [71] and an attempt has been made to calculate Frank constants via this route [72,73] (we return to this later). The potential advantages of this approach are that extrapolation to low k is not required, and indeed, in principle, the relevant quantities can be measured by determining relatively short-range correlation functions.

Although not an objective of this work, it is of interest to compare elastic constants determined in simulations with theoretical predictions, some inspired by the work of Onsager [15], and applied to systems of hard rods, spherocylinders, or ellipsoids [60, 68, 74–79], and some directed at soft-particle or attractive interactions [76, 80, 81]. Many of these approaches, implicitly or overtly, are based on density-functional theory which begins with an ansatz for $C(i, j)$. From the comparisons made to date [60] density-functional theories agree better with each other

than with simulation results for K_1–K_3, while reproducing the transition density and order-parameter variation quite well. This suggests that the predicted elastic constants are very sensitive to small errors in $C(i,j)$.

3.4 Simulation methods

In this section we describe the main aspect of our simulations that is not completely standard, namely the algorithm we used to constrain the director.

If left unconstrained, the system director will slowly reorient under the influence of thermal fluctuations. The set of wavevectors for which $\hat{\mathbf{Q}}(\mathbf{k})$ can be measured is fixed within the periodic simulation box frame, which we assume here to be cuboidal:

$$\mathbf{k} = \frac{2\pi n_x}{L_x}\hat{\mathbf{x}} + \frac{2\pi n_y}{L_y}\hat{\mathbf{y}} + \frac{2\pi n_z}{L_z}\hat{\mathbf{z}} \tag{3.10}$$

where n_x, n_y and n_z are integers and L_x, L_y and L_z are the box lengths. Therefore, in the director-based 123 frame, the components of $\mathbf{k} = (k_1, 0, k_3)$ will vary through a simulation run. To prevent this, it is convenient to fix the director by using Lagrangian constraints, and make it a constant of the motion. This approach has been used by Sarman and Evans [28] in studying transport coefficients of Gay-Berne-like systems. The effect of such a constraint on the properties of interest will be small, because the director is a quasi-conserved variable already (a Goldstone mode). Applying such a constraint allows us to measure the functions $\mathcal{W}_{\alpha\beta}(k_1, k_3) \propto \langle Q_{\alpha\beta}(\mathbf{k}) Q_{\alpha\beta}(-\mathbf{k})\rangle^{-1}$ on a fixed grid in k-space, simplifying the analysis, and allowing us to compare the fitted surfaces with the measured data points in a clear fashion. We emphasize that it is not *necessary* to use the director constraint method, and indeed many of our results are obtained from unconstrained runs, with the analysis performed in a way that takes account of director motion. We compare the two methods below.

We adopt the usual Lagrangian constraints formalism [82–84]. Taking the positions $\mathbf{r_i}$ and axis vectors $\mathbf{e_i}$ as generalised coordinates we write the Lagrangian as

$$\mathcal{L} = \frac{m}{2}\sum_{i=1}^{N}\dot{\mathbf{r}}_i^2 + \frac{I}{2}\sum_{i=1}^{N}\dot{\mathbf{e}}_i^2 - \mathcal{V}\,. \tag{3.11}$$

Keeping the director fixed is equivalent to requiring that two components of the order tensor vanish; for instance if we wish the director to lie along z, then the constraint conditions are $Q_{xz} = Q_{yz} = 0$, or

$$\begin{aligned} f^{(1)} &= \sum_{i=1}^{N} e_{ix} e_{iz} = 0 \\ f^{(2)} &= \sum_{i=1}^{N} e_{iy} e_{iz} = 0 \,. \end{aligned} \tag{3.12}$$

In addition, we constrain the orientation vectors to unit length: $|\mathbf{e}_i|^2 = 1$. These conditions become constraints on the time derivatives

$$\mathbf{e}_i \cdot \dot{\mathbf{e}}_i = 0 \qquad i = 1 \ldots N \tag{3.13}$$

$$\sum_{i=1}^{N} \mathbf{a}_i^{(1)} \cdot \dot{\mathbf{e}}_i = 0 \tag{3.14}$$

$$\sum_{i=1}^{N} \mathbf{a}_i^{(2)} \cdot \dot{\mathbf{e}}_i = 0 \tag{3.15}$$

where $\mathbf{a}_i^{(\alpha)} = \partial f^{(\alpha)} / \partial \mathbf{e}_i$ for $\alpha = 1, 2$. For director orientation along z, $\mathbf{a}_i^{(1)} = (e_{iz}, 0, e_{ix})$ and $\mathbf{a}_i^{(2)} = (0, e_{iz}, e_{iy})$.

To integrate the equations of motion numerically we use the Verlet leapfrog algorithm. The updating of the positions and velocities proceeds as usual. At each timestep, given the positions and orientations, we compute the forces at time t, $\mathbf{F}_i(t) = -\partial \mathcal{V} / \partial \mathbf{r}_i$, and use these forces to advance velocities from time $t - \frac{1}{2}\delta t$ to $t + \frac{1}{2}\delta t$:

$$\mathbf{v}_i(t + \tfrac{1}{2}\delta t) = \mathbf{v}_i(t - \tfrac{1}{2}\delta t) + \delta t \mathbf{F}_i(t)/m \,. \tag{3.16}$$

Next, the new midstep velocities are used to advance the positions from t to $t + \delta t$:

$$\mathbf{r}_i(t + \delta t) = \mathbf{r}_i(t) + \delta t \mathbf{v}_i(t + \tfrac{1}{2}\delta t) \,. \tag{3.17}$$

The equations of motion for the orientations, including terms for constraint forces, are

$$I \ddot{\mathbf{e}}_i = \mathbf{G}_i + \xi^{(1)} \mathbf{a}_i^{(1)} + \xi^{(2)} \mathbf{a}_i^{(2)} + \kappa_i \mathbf{e}_i \qquad i = 1 \ldots N \,, \tag{3.18}$$

where $\mathbf{G}_i = -\partial \mathcal{V} / \partial \mathbf{e}_i$. The Lagrange multipliers $\xi^{(\alpha)}$, $\alpha = 1, 2$ correspond to the two constrained order tensor components and the κ_i correspond to the length constraints.

At each timestep, we calculate the $\mathbf{G}_i$, $\mathbf{a}_i^{(1)}$, $\mathbf{a}_i^{(2)}$ and κ_i from the set of positions $\{\mathbf{r}_i\}$ and orientations $\{\mathbf{e}_i\}$ at time t. It is convenient to define components of $\mathbf{a}_i^{(1)}$ and $\mathbf{a}_i^{(2)}$ perpendicular to the axis vector:

$$\mathbf{b}_i^{(\alpha)} = \mathbf{a}_i^{(\alpha)} - \left(\mathbf{a}_i^{(\alpha)} \cdot \mathbf{e}_i\right) \mathbf{e}_i \,, \tag{3.19}$$

and let

$$\lambda_i = \kappa_i + \xi^{(1)} \mathbf{a}_i^{(1)} \cdot \mathbf{e}_i + \xi^{(2)} \mathbf{a}_i^{(2)} \cdot \mathbf{e}_i \,. \tag{3.20}$$

To find the Lagrange multipliers, we advance the velocities by half a timestep and solve the constraint equations at time t. The time t velocities are given by

$$I\mathbf{u}_i(t) = I\mathbf{u}_i(t - \tfrac{1}{2}\delta t) + \frac{\delta t}{2}\left\{\mathbf{G}_i + \xi^{(1)}\mathbf{b}_i^{(1)} + \xi^{(2)}\mathbf{b}_i^{(2)} + \lambda_i \mathbf{e}_i\right\} \qquad i = 1 \ldots N, \tag{3.21}$$

where all quantities on the right are evaluated at time t, and $\mathbf{u}_i \equiv \dot{\mathbf{e}}_i$. From eqns (3.13)–(3.15) we obtain

$$\lambda_i = -\left\{\frac{2I}{\delta t}\mathbf{u}_i(t - \tfrac{1}{2}\delta t) + \mathbf{G}_i\right\} \cdot \mathbf{e}_i(t) \qquad i = 1 \ldots N \tag{3.22}$$

and

$$\xi^{(\alpha)} = \sum_{\beta=1,2} [\mathsf{M}^{-1}]^{(\alpha\beta)} A^{(\beta)} \tag{3.23}$$

where

$$A^{(\beta)} = -\sum_{i=1}^{N} \left\{\frac{2I}{\delta t}\mathbf{u}_i(t - \tfrac{1}{2}\delta t) + \mathbf{G}_i + \lambda_i \mathbf{e}_i\right\} \cdot \mathbf{a}_i^{(\beta)} \tag{3.24}$$

and the 2×2 matrix M has elements

$$[\mathsf{M}]^{(\alpha\beta)} = \sum_{i=1}^{N} \mathbf{a}_i^{(\alpha)} \cdot \mathbf{b}_i^{(\beta)}. \tag{3.25}$$

Once λ_i and the $\xi^{(\alpha)}$ have been calculated, the new midstep velocities are obtained:

$$I\mathbf{u}_i(t + \tfrac{1}{2}\delta t) = I\mathbf{u}_i(t - \tfrac{1}{2}\delta t) + \delta t\left\{\mathbf{G}_i + \xi^{(1)}\mathbf{b}_i^{(1)} + \xi^{(2)}\mathbf{b}_i^{(2)} + \lambda_i \mathbf{e}_i\right\} \qquad i = 1 \ldots N. \tag{3.26}$$

The orientations are then advanced in the usual way:

$$\mathbf{e}_i(t + \delta t) = \mathbf{e}_i(t) + \delta t \mathbf{u}_i(t + \tfrac{1}{2}\delta t) \,. \tag{3.27}$$

With this dynamics, the total energy is well conserved, typically changing by less than 0.07% over a 100,000 step run, and the director is constrained to within 2×10^{-4} radians of the desired direction over the course of the entire set of runs.

We have noted occasionally an instability in the behaviour of the system in that the director field spontaneously splits into two differently-oriented domains, while the overall order tensor continues to obey the constraint condition. This has only happened twice in runs totalling over a million timesteps and needs further study. The results we present here correspond to runs in which a monodomain is stable throughout.

Finally in this section, we mention the simulation algorithms used. Some preliminary simulations using elongated periodic boxes (1:1:2 and 1:1:4) were carried out on a 1024-processor DAP computer using the Brode-Ahlrichs method to calculate the forces [42]. Advantage was taken of the relatively short interaction range by sorting the particles in the z-direction, so that it was only necessary to examine pairs whose z-coordinates were within the potential cutoff [85].

All the simulations with $\kappa = 3$, $\kappa' = 5$, $\mu = 1$, $\nu = 3$, using 8000 particles in cubic periodic boundary conditions, were carried out on 64 processors of a Cray T3D, using the domain decomposition program GBMEGA, which we decribe in chapter 2.

Lastly, most of the results for $\kappa = 3$, $\kappa' = 5$, $\mu = 2$, $\nu = 1$, in cuboidal boxes of shape 1:1:2 and 1:1:4, were obtained using a serial code running on a Silicon Graphics Power Challenge. For these simulations a simple Verlet neighbour list [86] was used, and extra efficiency was gained in the elongated boxes by using a one-dimensional link-cell structure of slices resolved in the z direction.

3.5 Data analysis

The data analysis consists of three parts. First, the instantaneous order tensor components are calculated in Fourier space for a set of wavevectors consistent with the periodic boundary conditions in the box-fixed xyz coordinate system. Secondly, these quantities are transformed to the 123 frame to obtain $|\hat{Q}_{13}|^2$ and $|\hat{Q}_{23}|^2$ as

functions of k_1^2 and k_3^2, and these quantities are accumulated in histogram bins for averaging. Finally, after the simulation is complete, the quantities, $\mathcal{W}_{13}$ and $\mathcal{W}_{23}$, defined by eqns (3.7), (3.8), are calculated and fitted to a bivariate polynomial in k_1^2 and k_3^2 whose leading coefficients furnish estimates for the elastic constants.

In the runs with **n** constrained, the transformation to the 123 frame is fixed throughout the simulation. In this case, we calculated the relevant symmetry components $\langle|\hat{Q}_{13}|^2\rangle$ and $\langle|\hat{Q}_{23}|^2\rangle$ during the course of each run, at intervals of 20 timesteps, and accumulated block averages over sub-runs of 1000 steps. Fluctuations on the block averages were used to estimate the errors on $\langle|\hat{Q}_{\alpha\beta}(\mathbf{k})|^2\rangle$. In all cases the simulation box was cuboidal, with $L_z > L_x = L_y$, and the wavevectors **k** considered were given by eqn (3.10) with n_x and n_y ranging from $0 \ldots 6$ and n_z from $0 \ldots 12$.

For the unconstrained runs, calculation of the relevant symmetry components of the order tensor fluctuations is more awkward: the slow variation in **n** over time means that the set of $\{k_1, k_3\}$ for which $\hat{Q}_{13}(k_1^2, k_3^2)$ and $\hat{Q}_{23}(k_1^2, k_3^2)$ can be calculated, change from one configuration to the next.

In order to obtain results with estimated errors ready for fitting, we calculated all six distinct components of $\hat{\mathbf{Q}}$ for **k** given by eqn (3.10) with $n_x, n_y, n_z = 0 \ldots 7$, for every stored configuration, and separately transformed the order tensor for each configuration and wavevector into the instantaneous 123 frame, thus building up histograms of $|\hat{Q}_{13}|^2$ and $|\hat{Q}_{23}|^2$ and their fluctuations on a rectangular grid of k_1^2 and k_3^2 values.

To calculate the errors in the mean for each histogram bin, it was necessary to estimate the statistical inefficiency $\mathcal{S}$, i.e. the ratio of the correlation time for these quantities to the sampling interval. $\mathcal{S}$ is not the same for all values of **k**: it is greatest for low k, reflecting correlation times as long as 20000 timesteps in some cases, but is much smaller for high k. Estimating $\mathcal{S}$ separately for every bin was not possible, because the director variation caused some bins to hold relatively few counts in particular sub-runs, but we found that $\mathcal{S}$ could be reasonably well represented by a smooth function of the form

$$\mathcal{S} = c + a/k_1^2 + b/k_3^2 \,.$$

We fitted the parameters a, b and c, using data from bins which were well sampled. Then for all bins, a value of $\mathcal{S}$ interpolated from the above formula, together with the measured mean-squared fluctuation in the counts for the bin, could be used to estimate the error. As an overall check, we found that results from two independent sets of runs could be made consistent within the errors calculated in this way, over the entire range of k values for which data is available.

A useful check on $\langle|\hat{Q}_{13}(\mathbf{k})|^2\rangle$ and $\langle|\hat{Q}_{23}(\mathbf{k})|^2\rangle$ is that in the $k \to \infty$ limit both must approach a constant value, which may be expressed in terms of Legendre moments of the one-particle orientational distribution function:

$$\mathcal{W}_\infty \equiv \lim_{k\to\infty} \mathcal{W}_{\alpha 3}(k_1, k_3) = \lim_{k\to\infty} \frac{9}{4} \frac{\overline{P}_2^2 V k_B T}{\langle|\hat{Q}_{\alpha 3}(\mathbf{k})|^2\rangle} = \frac{\overline{P}_2^2 \rho k_B T}{\frac{1}{21}\overline{P}_2 - \frac{4}{35}\overline{P}_4 + \frac{1}{15}} \,. \tag{3.28}$$

3.6 Results

In reduced units (see section 1.6), a simulation timestep of $\delta t = 0.0015$ was used for all the runs with $\mu = 2$, $\nu = 1$ [20], and $\delta t = 0.004$ for the runs with $\mu = 1$, $\nu = 3$ [23]. These values were found to give good energy conservation for all the state points considered.

Table 3.1 shows other relevant parameters of each set of simulations, and table 3.2 summarises the simulation results for each state point. We report the order parameter, calculated elastic constants K_1–K_3, and infinite-wavevector limit $\mathcal{W}_\infty$. The state points for the $\mu = 2$, $\nu = 1$ system were chosen to examine the effects of varying the state point while keeping the order parameter approximately the same. All these state points lie within the nematic region of the phase diagram [66]; it was checked that even at the highest density, the structure factor showed no strong peaks parallel to the director, which would indicate smectic ordering. As the temperature and density are both increased, the effect of the attractive part of the potential diminishes, so these results may shed some light on the role of attractive forces in determining the values of the elastic constants. For these state points, we carried out separate sequences of runs with the director constrained along the long axis (z) of the simulation box, along one of the short axes (x) of the box, and with

Table 3.1: Simulation details for calculation of elastic constants. ρ and T are the reduced density and temperature; N is the number of particles. The next column gives the relative $x : y : z$ dimensions of the simulation box. The last three columns are the total number of simulation timesteps with director constraint along x, along z, and unconstrained respectively.

ρ	T	N	Box shape	timesteps/1000 x-constrained	z-constrained	unconstrained
$\mu = 2, \nu = 1, \kappa = 3, \kappa' = 5$						
0.32	0.90	1024	1:1:2	1100	1100	—
0.33	1.00	1024	1:1:2	100	220	1100
0.35	2.00	1024	1:1:2	150	—	1350
0.38	3.00	2048	1:1:4	600	500	—
$\mu = 1, \nu = 3, \kappa = 3, \kappa' = 5$						
0.30	3.40	8000	1:1:1	—	—	110
0.30	3.45	8000	1:1:1	—	—	170

Table 3.2: Simulation results. ρ and T are the reduced density and temperature. K_1, K_2, K_3 are the Frank elastic constants; the $\{K_1, K_3\}$ pair come from the $\mathcal{W}_{13}$ surface fits the $\{K_2, K_3\}$ pair come from the $\mathcal{W}_{23}$ surface fits. $\overline{P}_2$ is the order parameter averaged over all runs; $\mathcal{W}_\infty$ is the large-k limit defined in eqn (3.28). Estimated statistical errors in the final digit(s) are given in parentheses.

ρ	T	K_1	K_3	K_2	K_3	$\overline{P}_2$	$\mathcal{W}_\infty$
$\mu = 2,\ \nu = 1,\ \kappa = 3,\ \kappa' = 5$							
0.32	0.90	0.652 (33)	2.01 (08)	0.676 (55)	2.01 (10)	0.674 (2)	2.86 (3)
0.33	1.00	0.697 (74)	2.59 (19)	0.718 (42)	2.27 (20)	0.708 (13)	2.69 (18)
0.35	2.00	1.511 (25)	4.79 (15)	1.099 (98)	5.23 (18)	0.663 (3)	4.70 (7)
0.38	3.00	3.55 (14)	13.5 (1)	2.53 (12)	13.0 (5)	0.730 (5)	10.5 (2)
$\mu = 1,\ \nu = 3,\ \kappa = 3,\ \kappa' = 5$							
0.30	3.40	2.17 (12)	3.97 (6)	1.71 (11)	3.95 (6)	0.553 (5)	4.55 (11)
0.30	3.45	1.59 (2)	2.23 (8)	1.34 (2)	2.19 (10)	0.478 (5)	3.52 (9)

no director constraint applied. The two state points for the $\mu = 1$, $\nu = 3$ system are reasonably close to the isotropic-nematic transition temperature for this system (which we estimate as lying between $T = 3.45$ and $T = 3.50$ for this system size, slightly below the estimate of reference [23], which was for a smaller system). For these runs, no director constraints were used.

The functions $\mathcal{W}_{13}(k_1, k_3)$ and $\mathcal{W}_{23}(k_1, k_3)$, defined in eqns (3.7), (3.8), are shown in Figures 3.3 and 3.4 for the four $\mu = 2$, $\nu = 1$ state points studied. We can see a significant increase in magnitude of these functions at higher densities, corresponding to larger values of K_1–K_3, and steadily developing orientational structure. Nonetheless, reasonable fits to the data can be obtained by the procedure described in section 3.5, in all cases, without introducing a large number of coefficients. Moreover, in general we found a high degree of consistency between the runs with and without director constraints applied. In addition, the results for K_3 from the fits to the $\mathcal{W}_{13}$ and $\mathcal{W}_{23}$ data are consistent with each other.

At the highest density, some systematic differences were observed at high values of k between data obtained from runs with the constraint applied in the x and z directions, and these differences are particularly apparent in figure 3.3 at high k_1 (corresponding to short-wavelength splay deformations). This appears to be a finite-size effect: the box dimensions for these runs were in the ratios 1:1:4, and constraining the director to be parallel or perpendicular to the long axis appears to have a measurable effect on orientational fluctuations. In fact, we observed a difference of 5% in the nematic order parameter between the two sets of runs, and this may be related to the high-k behaviour. Nonetheless, the $\mathcal{W}_{13}$ and $\mathcal{W}_{23}$ surfaces at low k seem to be insensitive to this, and we see no significant effect on our estimates of the elastic constants.

The values of the elastic constants quoted in table 3.2 are based on the low-order coefficients of the polynomials in k_1^2, k_3^2 used to fit the full set of data for each state point. The constrained-director runs give us the opportunity to compare slices through the fitted surfaces with measured data points along the k_1 and k_3 axes; we do this in figures 3.5–3.7, for the $\mu = 2$, $\nu = 1$, $\rho = 0.32$, $T = 0.90$ state point. It can be seen that the quality of the fit is excellent throughout, that different choices

Figure 3.3: The surface $\mathcal{W}_{13}(k_1, k_3)$ defined by eqn (3.7), which measures the inverse of the **k**-dependent orientational fluctuations, as a function of k_1^2 and k_3^2, for the system with $\mu = 2$, $\nu = 1$, at the four state points given in tables 3.1 and 3.2. We show the fitted surfaces used to estimate the elastic constants for all four cases (increasing (ρ, T), bottom to top) and our data points with estimated errors for the highest values $(\rho, T) = (0.38, 3.00)$.

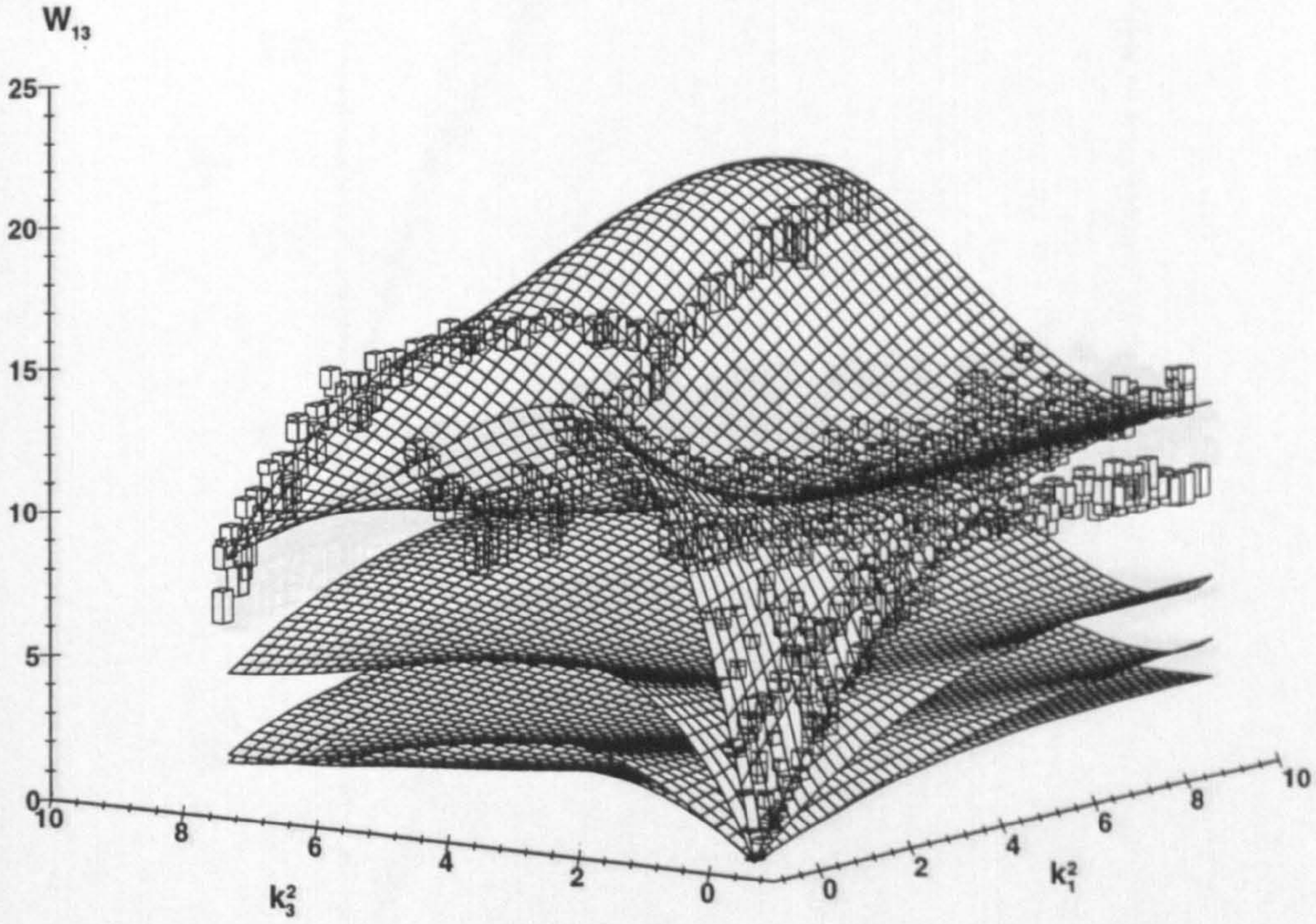

Figure 3.4: The surface $\mathcal{W}_{23}(k_1, k_3)$ defined by eqn (3.8), which measures the inverse of the **k**-dependent orientational fluctuations, as a function of k_1^2 and k_3^2, for the system with $\mu = 2$, $\nu = 1$, at the four state points given in tables 3.1 and 3.2. We show the fitted surfaces used to estimate the elastic constants for all four cases (increasing (ρ, T), bottom to top) and our data points with estimated errors for the highest values $(\rho, T) = (0.38, 3.00)$.

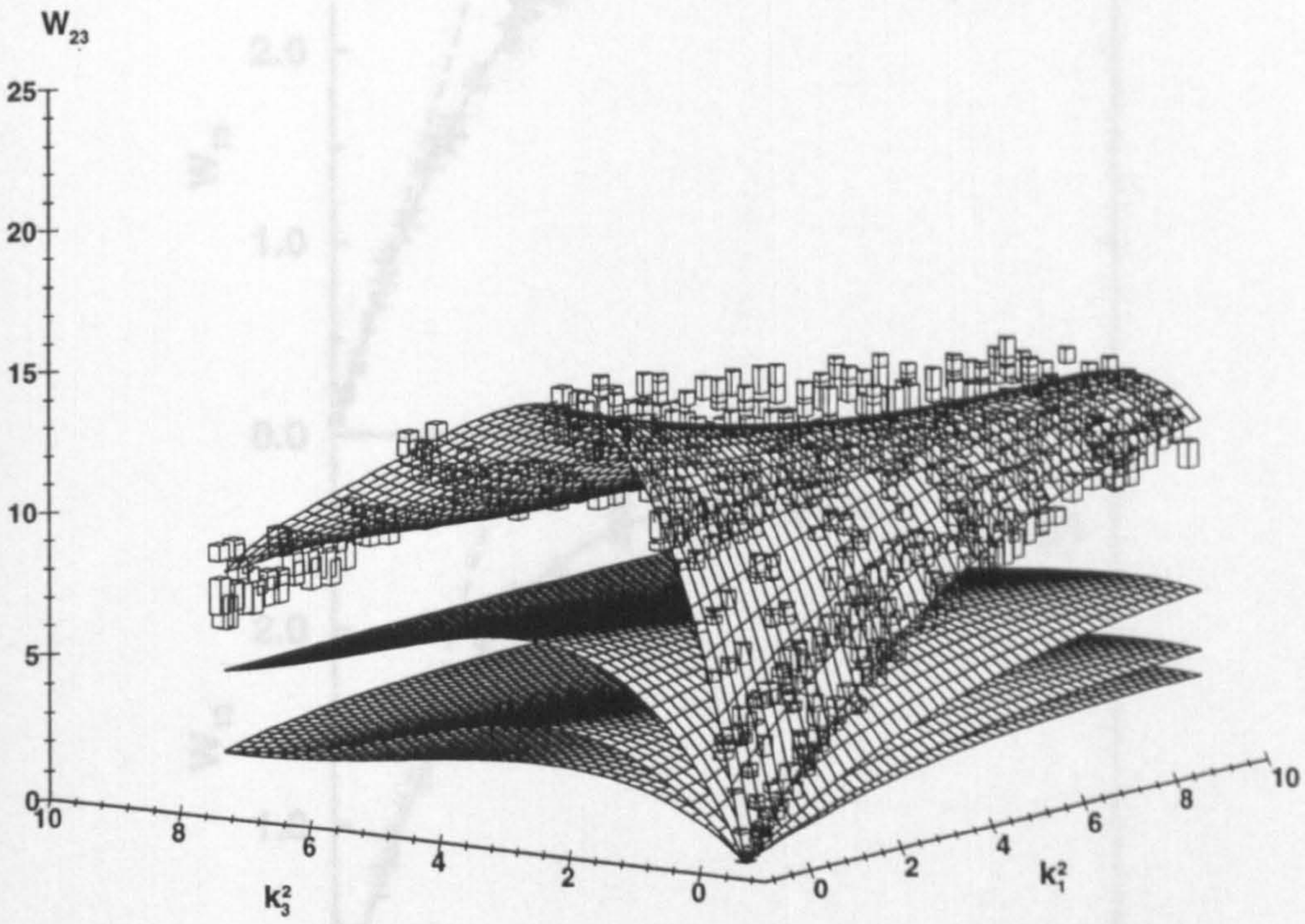

Figure 3.5: Splay fluctuations as a function of wavelength. For the $\mu = 2$, $\nu = 1$, $\rho = 0.32$, $T = 0.90$ state point we show $\mathcal{W}_{13}(k_1, k_3)$ for wavevectors in the plane perpendicular to the director $\mathbf{n}$, i.e. with $k_3 = 0$, plotted as a function of k_1^2. The error bars are the MD results for runs with $\mathbf{n}$ constrained to lie along (a) the x-axis and (b) the longer z-axis of the box respectively. The full curve shows the corresponding section of the surface $\mathcal{W}_{13}(k_1, k_3)$, which was fitted to all the data points, and the tangent at the origin is drawn with a gradient equal to the splay elastic constant K_1 calculated from the fitted surface.

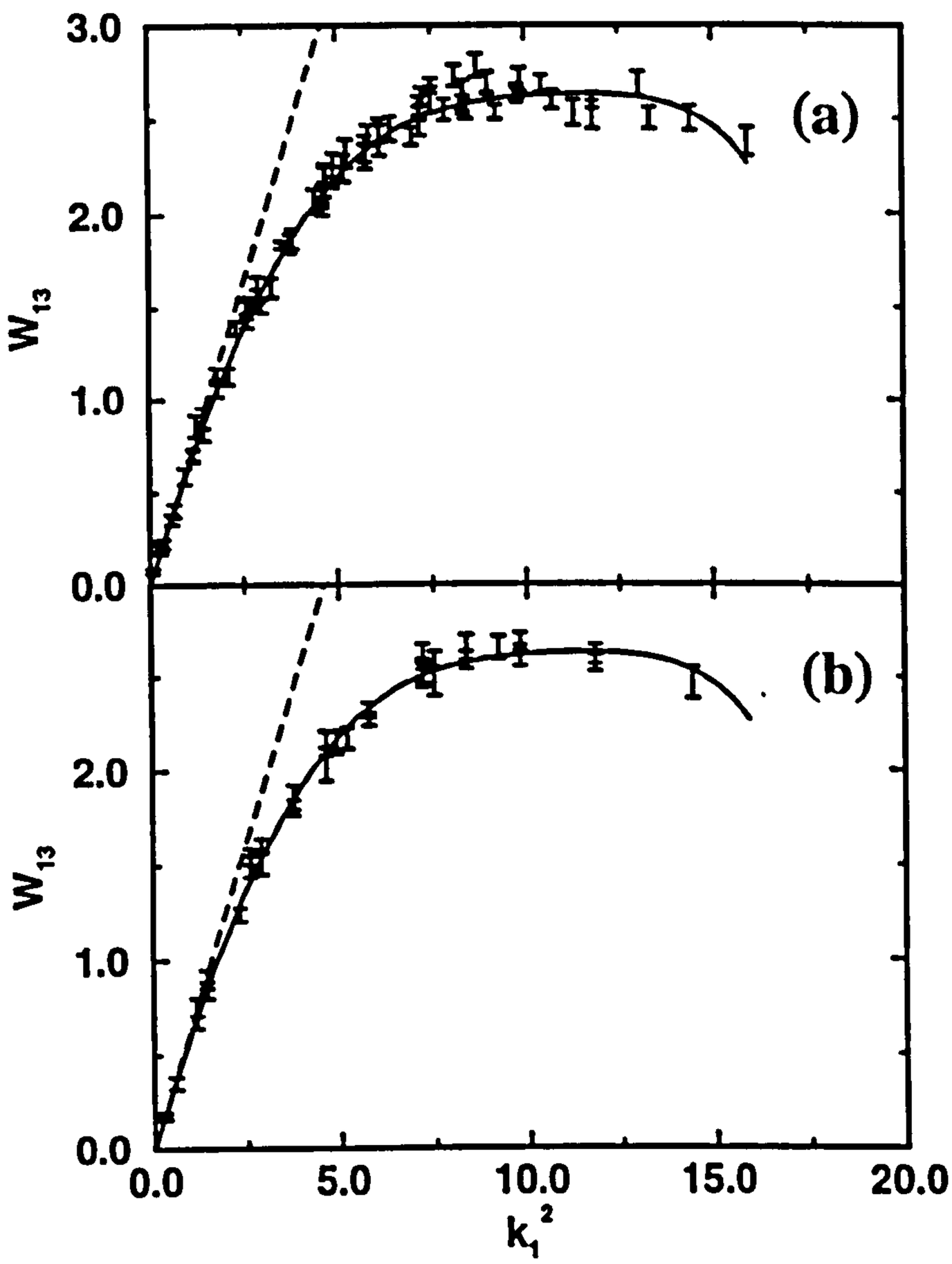

Figure 3.6: Twist fluctuations as a function of wavelength. For the $\mu = 2$, $\nu = 1$, $\rho = 0.32$, $T = 0.90$ state point we show $\mathcal{W}_{23}(k_1, k_3)$ for wavevectors in the plane perpendicular to the director $\mathbf{n}$, i.e. with $k_3 = 0$, plotted as a function of k_1^2. The error bars are the MD results for runs with $\mathbf{n}$ constrained to lie along (a) the x-axis and (b) the longer z-axis of the box respectively. The full curve shows the corresponding section of the surface $\mathcal{W}_{23}(k_1, k_3)$, which was fitted to all the data points, and the tangent at the origin is drawn with a gradient equal to the twist elastic constant K_2 calculated from the fitted surface.

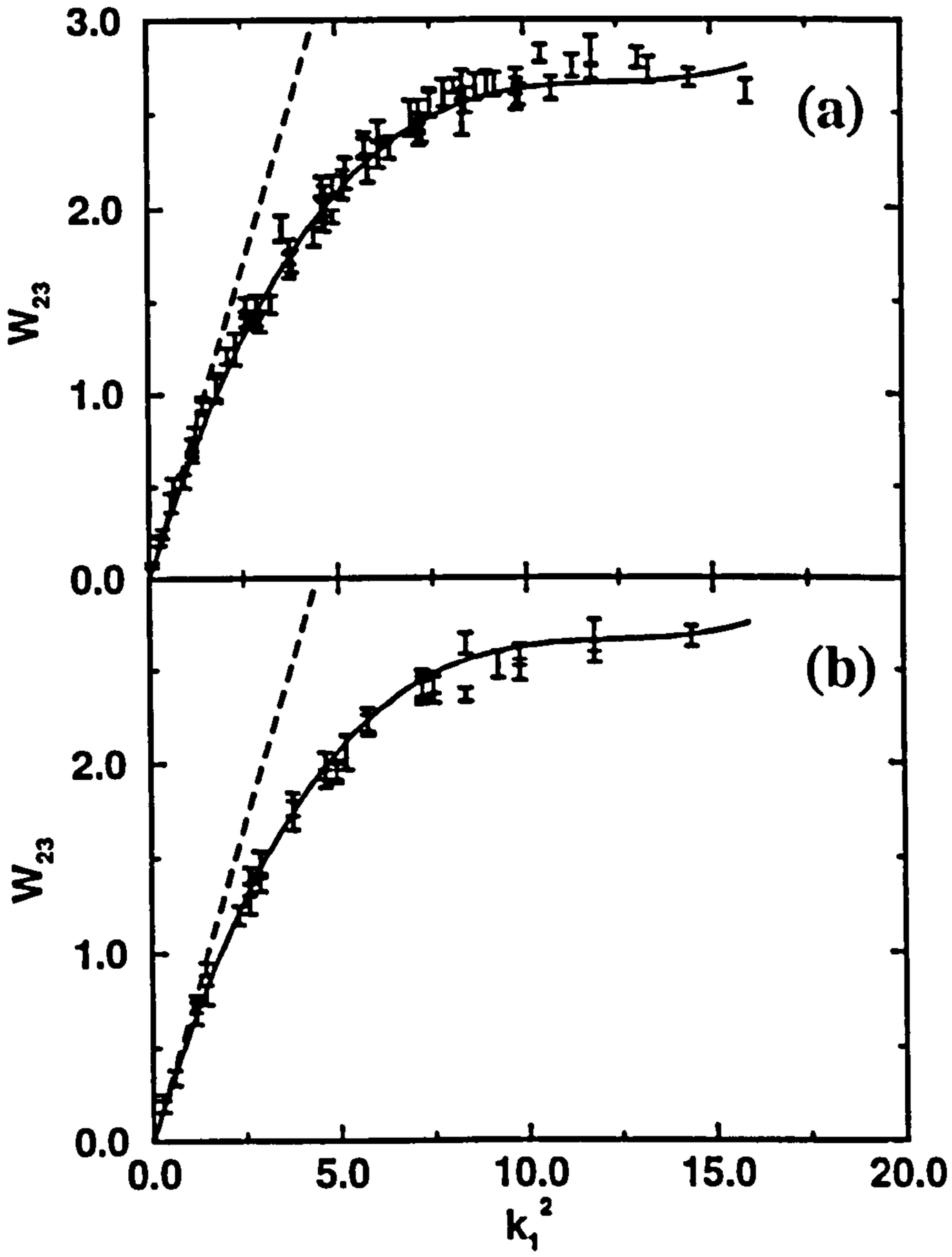

Figure 3.7: Bend fluctuations as a function of wavelength. For the $\mu = 2$, $\nu = 1$, $\rho = 0.32$, $T = 0.90$ state point we show $\mathcal{W}_{13}(k_1, k_3)$ and $\mathcal{W}_{23}(k_1, k_3)$ for wavevectors lying along the n-direction, i.e. with $k_1 = 0$, plotted as a function of k_3^2. The error bars are the MD results for runs as follows: (a) $\mathcal{W}_{13}$ with **n** constrained to lie along the x-axis; (b) $\mathcal{W}_{13}$ with **n** constrained to lie along the z-axis; (c) $\mathcal{W}_{23}$ with **n** constrained to lie along the x-axis; (d) $\mathcal{W}_{23}$ with **n** constrained to lie along the z-axis. The full curves show the corresponding sections of the appropriate surfaces, which were fitted to all the data points, and the tangent at the origin is drawn with a gradient equal to the bend elastic constant K_3 calculated from the fitted surface.

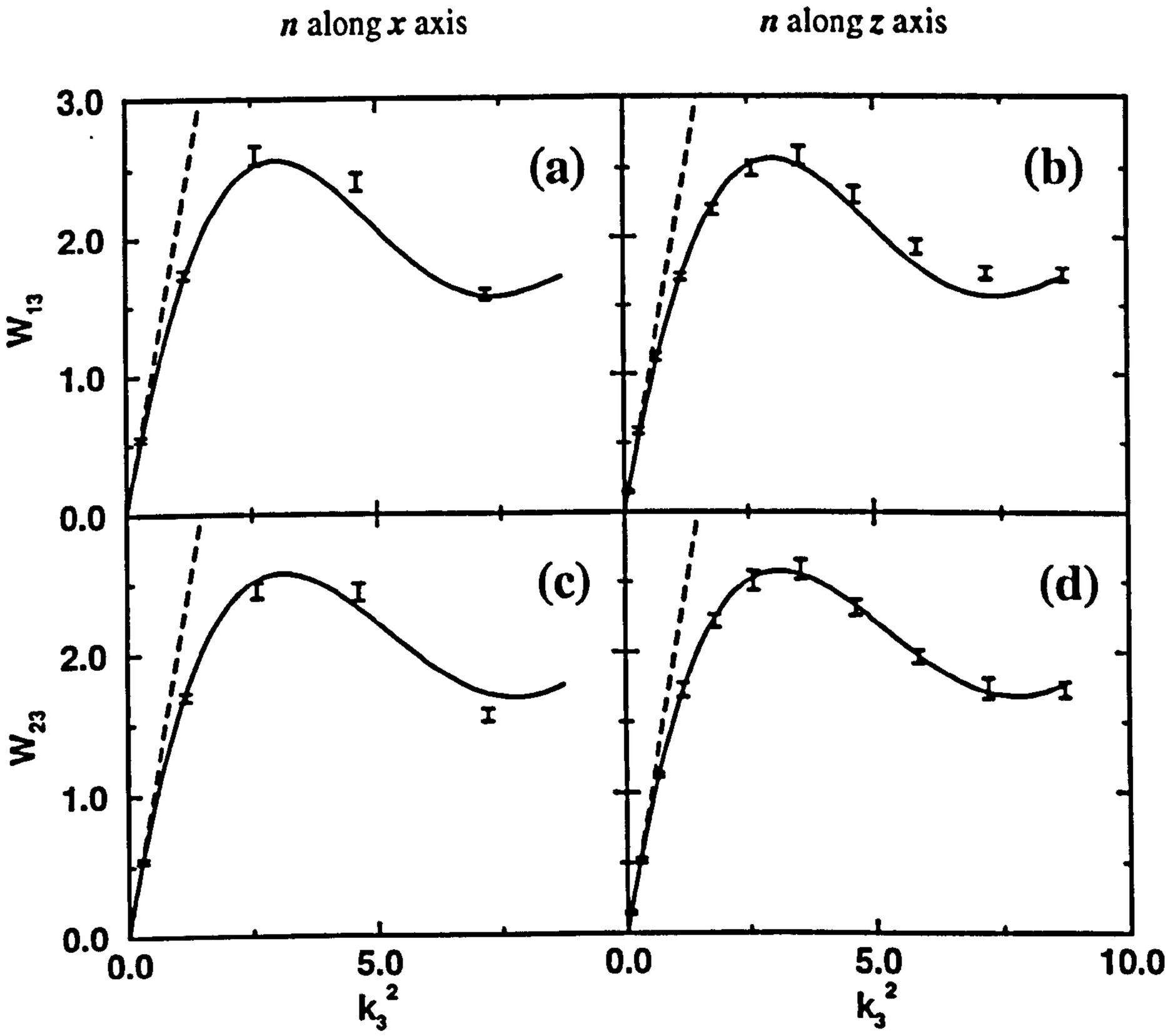

of director orientation produce consistent results, and that the two different ways of measuring K_3 (from $\mathcal{W}_{13}$ and $\mathcal{W}_{23}$) are also consistent. It is also clear from these figures that there is considerably more structure in the k-dependence of fluctuations where $\mathbf{k}$ lies along the director: there are far fewer $\mathbf{k}$-points lying in the asymptotic low-k regime in figure 3.7 than in the other cases. This makes estimating K_3 more prone to uncertainty than the other two cases, although the use of both $\mathcal{W}_{13}$ and $\mathcal{W}_{23}$ data partially offsets this factor.

For the parametrisation $\mu = 2, \nu = 1, \kappa = 3, \kappa' = 5$, we have studied state points of progressively higher density and temperature, chosen so as to maintain the nematic order parameter of the system at $\overline{P_2} \approx 0.7$. We observe a systematic increase in K_1, K_2 and K_3 with increasing density, whilst the variation in their relative magnitudes is less dramatic. In all cases we see that the inequality $K_3 > K_1, K_2$ expected for elongated molecules is obeyed, and the values of K_1 and K_2 are quite close to each other, with $K_1 > K_2$ in most cases.

Our estimates of the elastic constants for $\mu = 2, \nu = 1, \kappa = 3, \kappa' = 5$, $\rho = 0.33$, $T = 1.00$, may be compared with simulation results at the same state point by Stelzer et al. [72,73]. From Figures 6 and 9 of reference [73] their estimates of the elastic constants seem to be approximately $\{K_1, K_2, K_3\} = \{2.7 \pm 0.2, 2.5 \pm 0.2, 3.1 \pm 0.2\}$ at this state point, whereas our estimates (table 3.2) are $\{K_1, K_2, K_3\} = \{0.70 \pm 0.07, 0.72 \pm 0.07, 2.43 \pm 0.11\}$. There seem to be significant differences between these results, both in terms of the absolute values and the ratios of the elastic constants.

Our results for $\mu = 2, \nu = 1, \kappa = 3, \kappa' = 5$, $\rho = 0.35$, $T = 2.00$, may be roughly compared with data reported for systems of hard ellipsoids [58–60]. In table I of reference [60] reduced elastic constants $K_\alpha C/k_B T$ are reported (where C is the semi-minor axis) for ellipsoids of axial ratio $e = 3$, at a reduced density $\rho v_0 = 0.555$ where v_0 is the ellipsoid volume. If we approximate $v_0 = \pi\kappa\sigma_s^3/6 = 1.571$, in our units, this corresponds to a density $\rho = 0.353$, and the closest comparison density in table 3.2 is $\rho = 0.35$. The order parameter in the hard ellipsoid simulation is $\overline{P_2} = 0.7$, similar to ours. Setting $T = 2.0$ and $C = \frac{1}{2}$, the hard ellipsoid elastic constants become, in our units, $\{K_1, K_2, K_3\} = \{1.80, 1.64, 6.0\}$: these values are somewhat higher than ours, $\{K_1, K_2, K_3\} = \{1.51, 1.1, 5.0\}$ but the ratios are comparable; we emphasize that

there is no good reason to expect the two systems to match closely, because of the difference in interaction potential. If, instead, the softness of our potential function leads us to compare with slightly smaller hard ellipsoids, say 2–3% smaller in linear dimensions, the compensating change in v_0 means that the relevant comparison density in our simulations is the highest one in table 3.2, namely $\rho = 0.38$. Setting $T = 3.0$ we obtain a set of values from the hard particle simulations, $\{K_1, K_2, K_3\} = \{2.70, 2.46, 9.0\}$, to be compared with our $\{K_1, K_2, K_3\} = \{3.55, 2.53, 13.25\}$. Now our values are larger, and the ratios are again comparable.

3.7 Conclusions

We have calculated the Frank elastic constants of the Gay-Berne fluid at a number of state points and with two commonly used parametrizations of the potential, by performing molecular dynamics simulations. These results were obtained by examining the behaviour in the long-wavelength limit of fluctuations in appopriate symmetry components of the reciprocal space order tensor $\hat{Q}_{\alpha\beta}(\mathbf{k})$. We have shown that it is possible to obtain the corresponding equilibrium averages very accurately at sufficiently low k, so as to reach the regime in which the Frank expression for the free energy is valid. System sizes of the order of a few thousand molecules are perfectly adequate for this kind of calculation, but simulation run lengths of the order of hundreds of thousands of timesteps are needed, in view of the very long correlation times for long wavelength fluctuations.

In some of our simulations, a set of Lagrangian constraints was added to the equations of motion in order to keep the nematic director fixed; in others no such constraints were applied, so the director wandered slowly away from its initial direction. Constraining the director simplifies the data analysis considerably, and in particular makes it relatively simple to estimate statistical errors on each k-histogram bin. Without the director constraint, it is still possible compute the desired quantities by discretising the data onto a grid of k values, at the expense of complicating the averaging process and the estimation of statistical errors. We have shown that the results from constrained and unconstrained runs are consistent.

Our results compare reasonably well with simulation results for hard ellipsoids. In all cases, the bend elastic constant K_3 is much larger than the other two, while K_1 and K_2 adopt quite similar values to each other. All the elastic constants increase with increasing density at roughly constant order parameter (with the temperature also increasing to ensure this). Any comparison of results for different systems (for example, with and without attractive forces) must take account of the sensitivity of the elastic constants to both density and order parameter, which may complicate comparisons of one state point with another.

Our results do not agree well with those in [72,73], which proceed via calculation of the direct correlation function $C(i,j)$. There could be many reasons for this, but clearly much depends on the accuracy with which $C(i,j)$ is obtained by inverting the Ornstein-Zernike equation in the nematic phase. The integrals of eqn (3.9) include powers of separation r_{ij} that make the result very sensitive to the form of the appropriate components of $C(i,j)$. Our runs are conducted on much larger systems, and are much longer, than those of [72,73], but, of course, this does not rule out the possibility of obtaining satisfactory results by the $C(i,j)$ route using smaller systems and shorter runs. These points clearly require further study.

Chapter 4

Pretransitional effects and kinetics of the Nematic-Isotropic Transition

4.1 Introduction

In this chapter we investigate several aspects of the nematic to isotropic phase transition. This transition is known experimentally [3] to be weakly first order in character. As the isotropic phase is cooled there is an increase in the range of orientational correlations: the inverse correlation length ξ_2^{-1} can be extrapolated to zero at a temperature T^*. In fact though, this divergence is pre-empted by the occurence of the phase transition at a slightly higher temperature, $T_{\rm NI}$ - experimentally, $T_{\rm NI} - T^*$ is a fraction of a Kelvin, or $(T_{\rm NI} - T^*)/T_{\rm NI} \approx 10^{-3}$. Another well-known effect which accompanies the coarsening of correlated domains is the lengthening of relaxation times for orientational fluctuations of a given wavelength.

There have been several previous computer simulation studies of pretransitional phenomena at the NI transition. Some of these [87–89] used the Lebwohl-Lasher lattice model [11,12]. The computational simplicity of this model permits the study of large system sizes (more than 30^3 spins) and relatively long simulations. However, the absence of translational degrees of freedom means that this model corresponds

with real liquid crystals only in the most coarse grained sense. There have also been some investigations of hard particle models [90]. These provide some evidence for the growth of static correlations and slowing down of collective reorientation in the neighbourhood of the phase transition. The system sizes studied in these these early simulations were quite small, which restricted the range of correlations to a few molecular diameters. We felt it was desirable to perform simulations on a larger system, as this allows one to investigate longer ranged behaviour of the pair correlation function $h(1,2)$, to be defined in section 4.2. Another motivation for revisiting this area is that techniques have recently become available [91] for inverting the Ornstein Zernike (OZ) equation, i.e. calculating the direct correlation function $c(1,2)$ from $h(1,2)$. Whilst $c(1,2)$ cannot be measured directly in experiments, in some respects it is the more fundamental quantity, and it plays an important role in theories of liquids and liquid crystals. In particular, the condition of stability of the isotropic phase with respect to the nematic can be expressed in terms of moments of $c(1,2)$ [92–94]. The results presented in this chapter are from extensive molecular dynamics simulations of a large system of Gay-Berne particles, at temperatures in the neighbourhood of the NI phase transition $T_{\rm NI}$.†

In addition to the static correlation functions, we have also investigated the behaviour of time correlation functions describing the relaxation of long-wavelength orientational fluctuations. In a separate set of simulations, we performed a sudden quench of a larger system from the isotropic phase to a state point just inside the nematic. Whilst the system size and timescale studied were not sufficient to reach the scaling regime, we do obtain some information concerning the kinetics of nematic ordering in the early stages of the transition.

The structure of this chapter is as follows. In section 4.2 we define the correlation functions which we measure, and summarise the methods used to invert the OZ equation. In section 4.3 we give the details of our simulations. Sections 4.4 and 4.5 contain our results for static and dynamic correlations respectively. Section 4.6 briefly describes the results of our simulated quench from the isotropic to nematic

†In order to avoid confusion, we drop the suffix '*' from temperatures, density etc. when referring to our simulations. Reduced units are used throughout this chapter.

phase. We conclude in section 4.7 with a summary, comparison with Landau-de Gennes (LdG) theory and some thoughts on possible future work.

4.2 Background

4.2.1 Distribution functions

In a *simple* fluid, the static structure is completely described by the single particle density $\rho_0(r)$ and its correlation functions, defined by [7]

$$\rho_{(n)}(\mathbf{r}_1, \mathbf{r}_2, \cdots \mathbf{r}_n) = \langle \rho(\mathbf{r}_1)\rho(\mathbf{r}_2)\cdots\rho(\mathbf{r}_n)\rangle \ , \tag{4.1}$$

where the angle brackets denote an ensemble average. In a homogeneous simple fluid of average density $\rho = N/V$, two-point correlations are described by the pair distribution function,

$$g(\mathbf{r}_1, \mathbf{r}_2) = \rho_{(2)}(\mathbf{r}_1, \mathbf{r}_2)/\rho_{(1)}^2 \ , \tag{4.2}$$

which represents the conditional probability per unit volume of finding a particle at $\mathbf{r}_2$, given that there is a particle at $\mathbf{r}_1$.

In a fluid of uniaxial molecules, these definitions must be extended to include the orientational degrees of freedom [95]. The single-particle density becomes $\rho(\mathbf{r}, \Omega)$, the probability per unit solid angle and unit volume of finding a particle at $\mathbf{r}$ with orientation Ω. In the isotropic phase, $\rho(\mathbf{r}, \Omega)$, is independent of Ω. In the nematic, orientational ordering can be expressed in terms of Legendre moments of $\rho(\mathbf{r}, \Omega)$ about the director $\mathbf{n}$ [95] :

$$\langle P_l \rangle = \frac{1}{V}\int \mathrm{d}\mathbf{r}\, \mathrm{d}\Omega\ P_l(\Omega \cdot \mathbf{n})\, \rho(\mathbf{r}, \Omega) \qquad l = 2, 4, 6 \ldots \ , \tag{4.3}$$

of which the second, $S = \langle P_2 \rangle$, is the nematic order parameter. The symmetry of the nematic phase is such that all odd moments vanish, i.e. the directions $\mathbf{n}$ and $-\mathbf{n}$ are completely equivalent.† Eqn (4.2) can be similarly generalised, to define a function $g(1,2) = g(\mathbf{r}_1, \mathbf{r}_2, \Omega_1, \Omega_2)$ specifying the probability density of finding a

†This does not necessarily mean that the molecules themselves have head-tail symmetry, although in the case of the Gay-Berne model the orientations $\mathbf{e}_i$ and $-\mathbf{e}_i$ *are* indistinguishable.

particle with orientation Ω_2 at $\mathbf{r}_2$, given that there is a particle oriented along Ω_1 at $\mathbf{r}_1$. It is also useful to define the pair correlation function $h(1,2) = g(1,2) - 1$. In the homogeneous case, $h(1,2) = h(\mathbf{r}_{12}, \Omega_1, \Omega_2)$ where $\mathbf{r}_{12} = \mathbf{r}_2 - \mathbf{r}_1$. Uniaxiality of the nematic phase implies invariance of h under rigid rotations of $(\hat{\mathbf{r}}_{12}, \Omega_1, \Omega_2)$ about $\mathbf{n}$, so that $h(1,2)$ can be considered a function of five angles and the pair separation $r_{12} = |\mathbf{r}_{12}|$. In the isotropic phase, $h(1,2)$ is additionally invariant under arbitary rigid rotations of $(\hat{\mathbf{r}}_{12}, \Omega_1, \Omega_2)$, as well as rotations of Ω_1 and Ω_2 through a common angle about $\hat{\mathbf{r}}_{12}$, leaving three angular degrees of freedom (see figure 4.1).

4.2.2 Basis functions

In the molecular frame ($\hat{\mathbf{r}}_{12} = \mathbf{z}$) we can expand $h(1,2)$, or indeed any pair function, in terms of a complete set of angular functions of the coordinates shown in figure 4.1:

$$h(\Omega_1, \Omega_2, r, \hat{\mathbf{r}}) = \sum_{m,\chi_1} \sum_{n,\chi_2} h_{mn\chi_1\chi_2}(r)\, Y^m_{\chi_1}(\theta_1, \phi_1)\, Y^n_{\chi_2}(\theta_2, \phi_2)\,. \tag{4.4}$$

The abovementioned symmetries of pair functions in the isotropic phase restrict the

Figure 4.1: Molecular frame coordinates for the calculation of the pair correlation function $h(\mathbf{r}_{12}, \Omega_1, \Omega_2)$

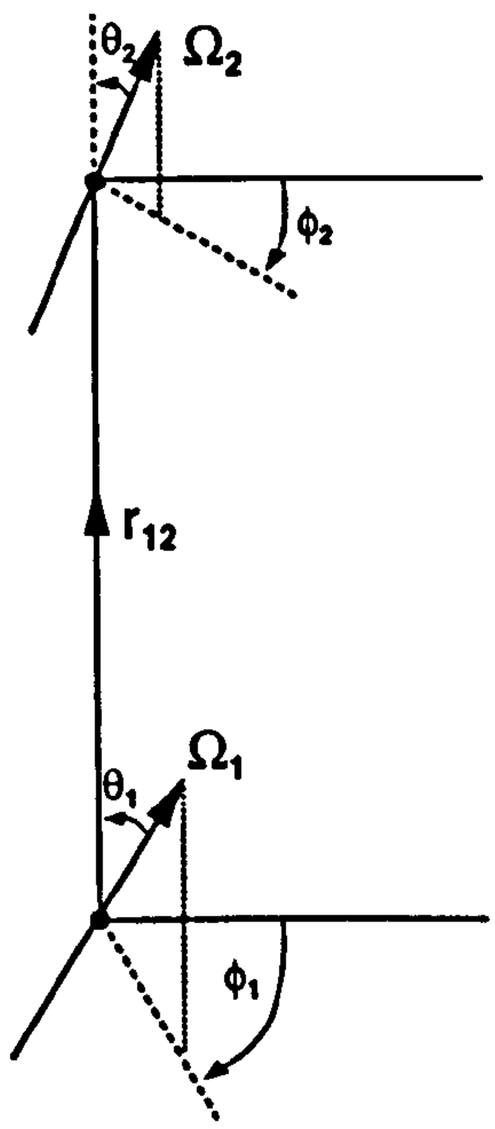

values of m, χ_1, n and χ_2: m and n must be even (head-tail symmetry), $\chi_1 + \chi_2 = 0$ (rotational invariance about **z**) and we can also take $m \geq n$ without loss since $h(2,1) = h(1,2)$. We therefore set $\chi_1 = -\chi_2 = \chi$ and write the coefficients in the molecular frame as $h_{mn\chi}(r)$.

It is also convenient to introduce an orthogonal set of *rotational invariants* in the laboratory frame [96]:

$$\Phi^{mnl}(\Omega_1, \Omega_2, \hat{\mathbf{r}}) = 4\pi \sum_{\mu\nu\lambda} \sqrt{\frac{2\pi}{2l+1}} \begin{pmatrix} m & n & l \\ \mu & \nu & \lambda \end{pmatrix} Y_\mu^m(\Omega_1)\, Y_\nu^n(\Omega_2)\, Y_\lambda^l(\hat{\mathbf{r}})\,, \qquad (4.5)$$

where the $\begin{pmatrix} m & n & l \\ \mu & \nu & \lambda \end{pmatrix}$ are Wigner $3j$ symbols. Pair functions can also be expanded in terms of this basis set:

$$h(r, \hat{\mathbf{r}}, \Omega_1, \Omega_2) = \sum_{mnl} h^{mnl}(r) \Phi^{mnl}(\hat{\mathbf{r}}, \Omega_1, \Omega_2)\,. \qquad (4.6)$$

These expansions are completely equivalent, and the mnl and $mn\chi$ sets of coefficients are trivially related, via the χ-transform (see table 4.1).

4.2.3 Inverting the OZ equation

The direct correlation function $c(1,2)$ is related to $h(1,2)$ via the Ornstein Zernike (OZ) equation [7] :

$$h(1,2) = c(1,2) + \frac{1}{4\pi} \int \mathrm{d}\mathbf{r}_3\, \mathrm{d}\Omega_3\, \rho_0(\Omega_3)\, h(1,3)\, c(3,2)\,. \qquad (4.7)$$

Since we are concerned solely with the isotropic phase, $\rho_0(\Omega) = \rho$, a constant. The solution of this integral equation can be carried out either in reciprocal space or in real space using the Baxter factorisation method. The k-space inversion method relies on an elegant factorisation of the OZ equation, the result of early work by Blum [97–99]. This is formally a matrix equation relating the $mn\chi$ coefficients of the Hankel transforms of c and h:

$$\tilde{h}_{mn\chi}(k) = \tilde{c}_{mn\chi}(k) + (-1)^\chi \rho \sum_p \tilde{h}_{mp\chi}(k) \tilde{c}_{pn\chi}(k)\,. \qquad (4.8)$$

The Hankel transforms are most conveniently carried out in the *mnl* basis. In practice we make use of the fact that the l^{th} order Hankel transform is equivalent to a *hat* transform (defined in table 4.1) followed by a Fourier-Bessel (FB) transform. Splitting the calculation up in this way does not appear to introduce any numerical difficulties, and is more efficient computationally since the FB transform can be calculated using an FFT.

The real space inversion is based on the Baxter factorisation method [100] which is valid for finite-ranged direct correlation functions. Again, the generalisation to molecular liquids is due to Blum [99]. Briefly, it involves solving (independently for each χ) a pair of simultaneous matrix equations

$$2\pi r \mathbf{c}_\chi(r) = -\mathbf{Q}'_\chi(r) + (-1)^\chi \rho \int_r^R \mathrm{d}s\, \mathbf{Q}'_\chi(s)\mathbf{Q}^{\mathrm{T}}_\chi(s-r) \tag{4.9}$$

$$2\pi r \mathbf{h}_\chi(r) = -\mathbf{Q}'_\chi(r) + (-1)^\chi \rho \int_0^R \mathrm{d}s\, 2\pi(r-s)\hat{\mathbf{h}}_\chi(r-s)\mathbf{Q}_\chi(s)\,, \tag{4.10}$$

for the unknowns $\mathbf{Q}_\chi$ and $\mathbf{c}_\chi(r)$. In these expressions, $\mathbf{c}_\chi$ etc. are square matrices with elements $c_{mn\chi}$, both m and n running from 0 to l_{max}, primes indicate differentiation, and $\mathbf{X}^T$ denotes the transpose. These equations are solved iteratively.

The two methods are shown schematically in figure 4.2. In both cases, we truncate at some upper value of l - we found that $l_{\text{max}} = 8$ was adequate.

We note in passing that to date, no attempt has been made to calculate the direct correlation function in the *nematic* phase from simulations - this is more complicated, since many more symmetry components are involved.

Figure 4.2: The sequence of transformations used in the real-space and reciprocal-space solution of the Ornstein-Zernike equation. The various transforms involved are defined in table 4.1.

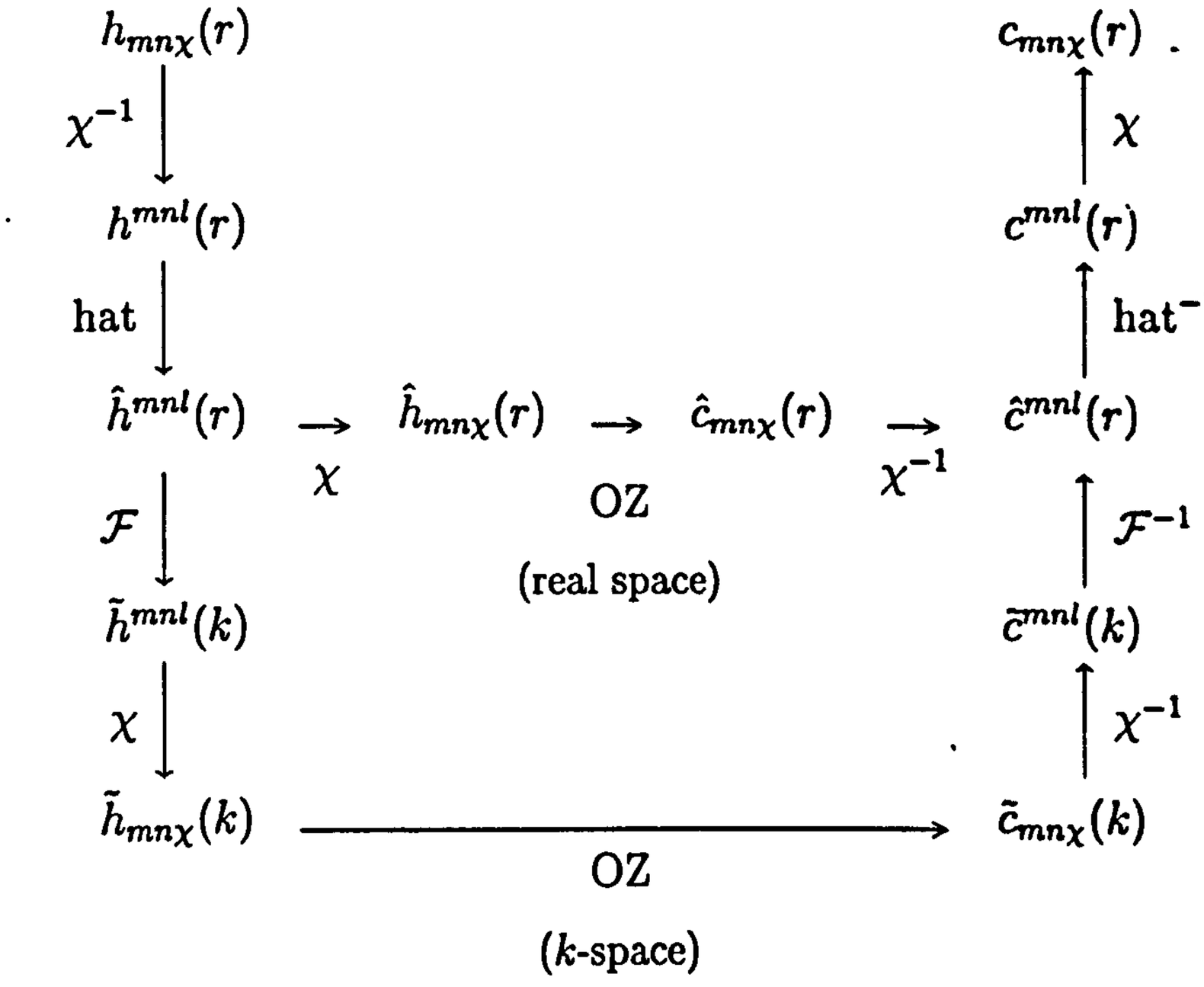

Table 4.1: Transforms used in the inversion of the OZ equation.

χ	Chi transform	$f_{mn\chi} = \sum_l \begin{pmatrix} m & n & l \\ \chi & -\chi & 0 \end{pmatrix} f^{mnl}$
χ^{-1}	Inverse chi	$f^{mnl} = (2l+1) \sum_\chi \begin{pmatrix} m & n & l \\ \chi & -\chi & 0 \end{pmatrix} f_{mn\chi}$
hat	order-l hat transform	$\hat{f}_l(r) = f_l(r) - \int_r^\infty \frac{f_l(s)}{s} P_l^e(\frac{r}{s})\, \mathrm{d}s$
hat^{-1}	Inverse hat	$f_l(r) = \hat{f}_l(r) - \frac{1}{r^3} \int_0^r s^2 \hat{f}_l(s) P_l^e(\frac{s}{r})\, \mathrm{d}s$
		where $P_l^e(x) = \frac{1}{x} \frac{\mathrm{d}P_l(x)}{\mathrm{d}x}$,
		$P_l(x)$ Legendre polynomials.
$\mathcal{F}$	Fourier-Bessel transform	$\tilde{f}(k) = \int_0^\infty \frac{\sin kr}{kr} f_l(r)\, r^2 \mathrm{d}r$
$\mathcal{F}^{-1}$	Inverse Fourier-Bessel	$f(r) = \frac{1}{2\pi} \int_0^\infty \frac{\sin kr}{kr} \tilde{f}_l(k)\, k^2 \mathrm{d}k$

4.3 Simulation details

The techniques used for these simulations are completely standard - i.e. constant NVE molecular dynamics, with periodic rescaling of velocities to maintain the desired kinetic temperature. All the simulations were carried out on the T3D machines at Bologna and Edinburgh, using the GBMEGA domain decomposition program described in chapter 2. The variant of the Gay-Berne potential used was the one first studied by Berardi *et al* [23]. Other relevant parameters of the simulation are listed in table 4.2. The length of the equilibration run in each case was judged by examining the evolution of the pair distribution function $h^{220}(r)$. During each run, we stored the configurations at intervals of either 20 or 100 timesteps, and monitored the nematic order parameter P_2. As illustrated in figure 4.3, we found spontaneous ordering on cooling from $T = 3.50$ to $T = 3.45$; however, at $T = 3.47$, P_2 fluctuated over a very large timescale. We therefore estimate that $T_{\mathrm{NI}} \approx 3.47$ lies between $T = 3.45$ and $T = 3.50$, compared with a value of 3.57 for the smaller system size studied in reference [23].

Figure 4.3: Evolution of the nematic order parameter in runs (i) cooled from $T = 3.50$ to $T = 3.45$, (ii) cooled from $T = 3.50$ to $T = 3.47$.

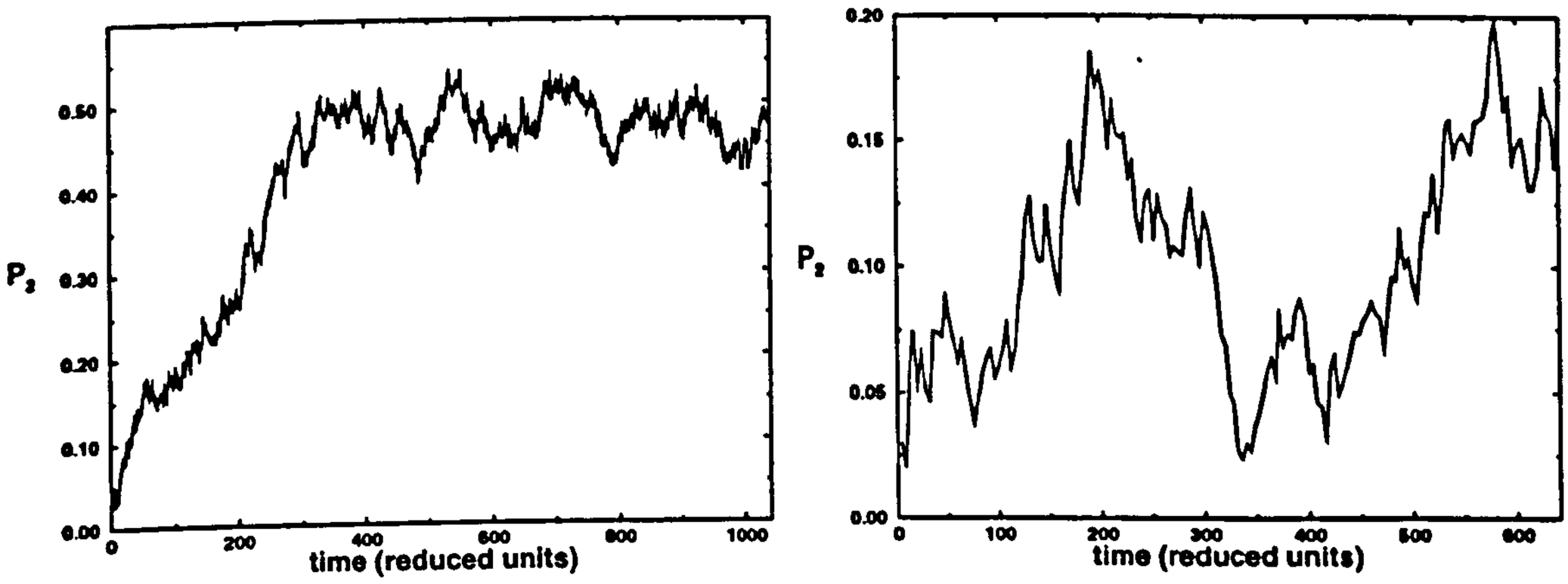

(i) (ii)

Figure 4.4: Temperature dependence of (top) the correlation length, and (bottom) the $c^{(m)}$ functions, in the vicinity of the phase transition.

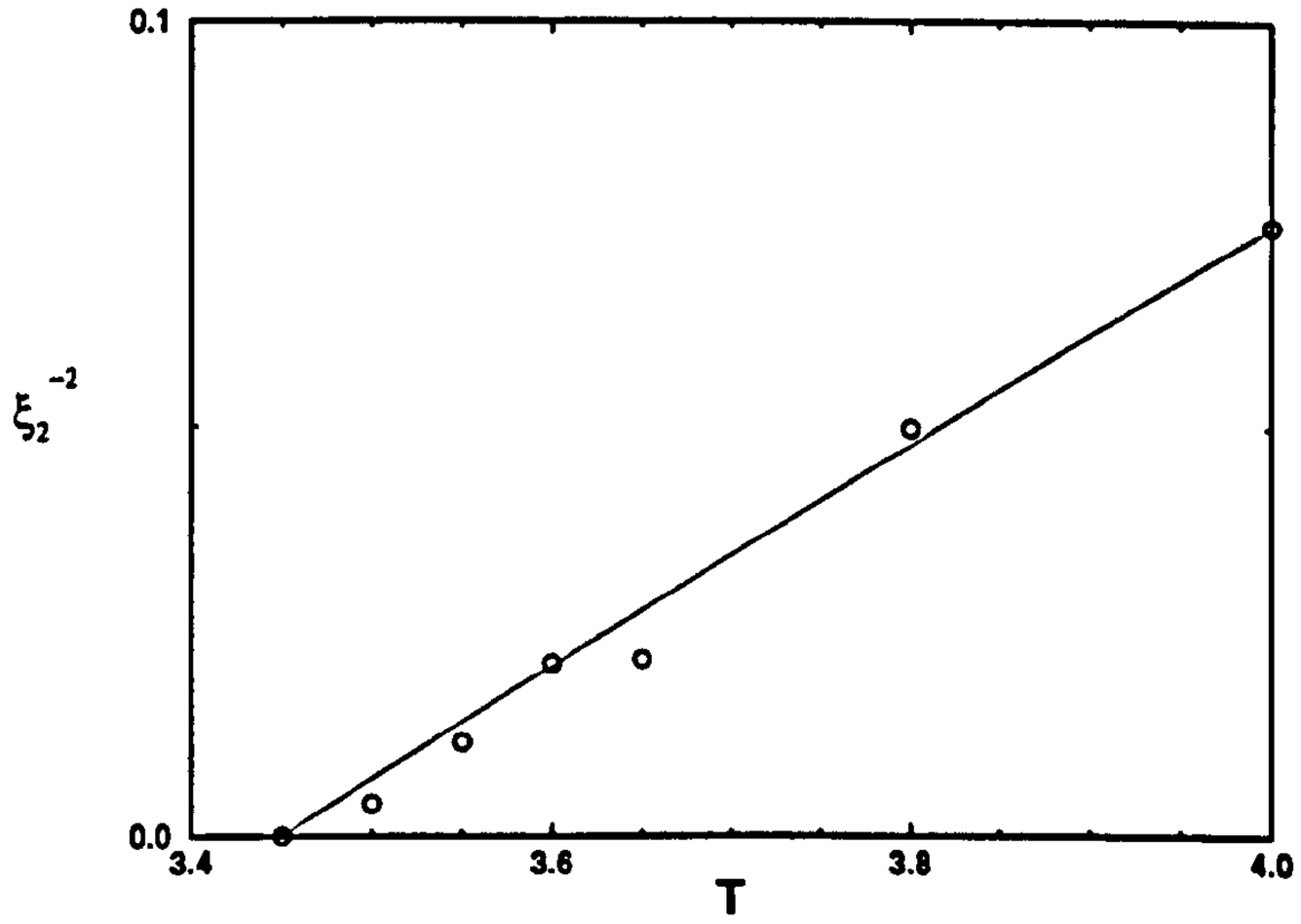

(i)

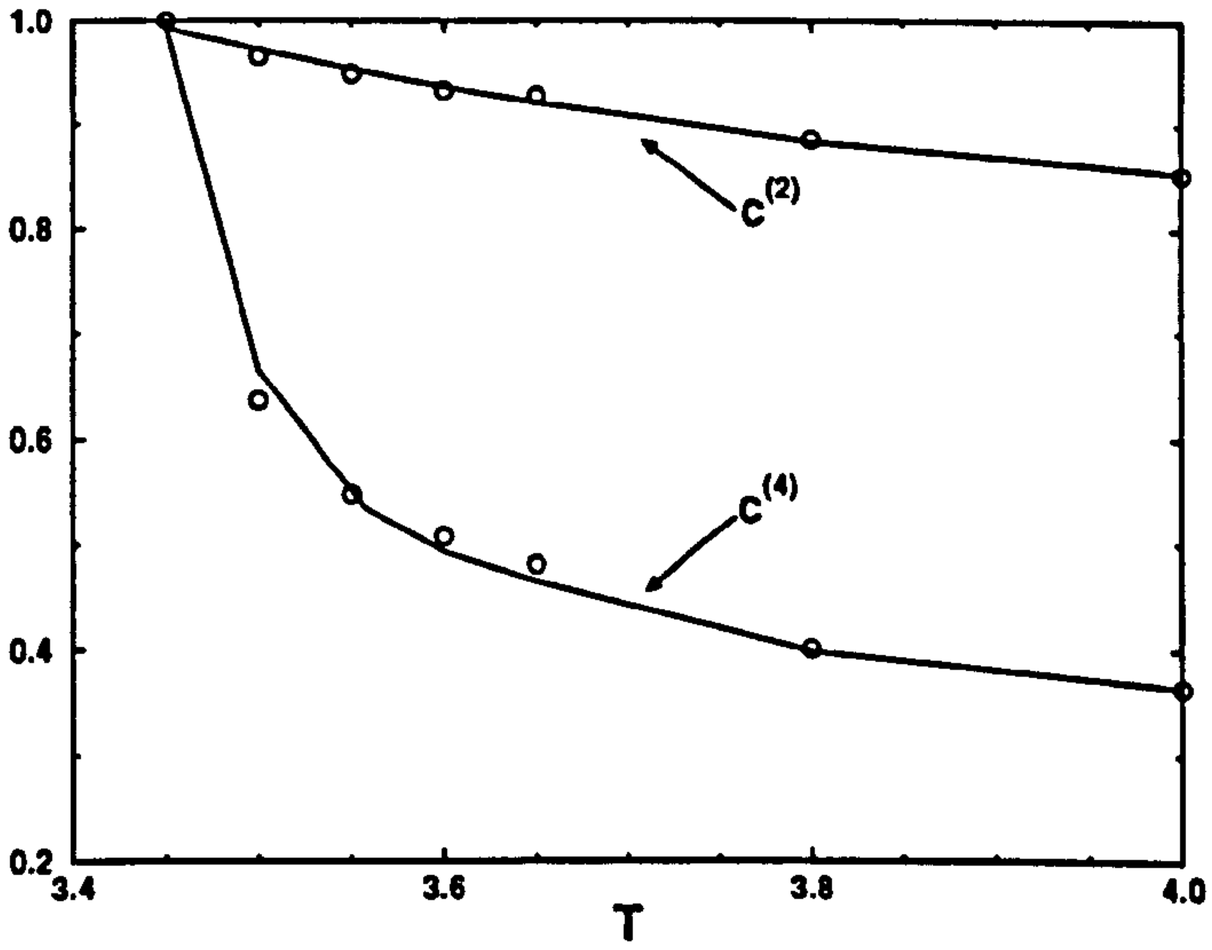

(ii)

Table 4.2: Run parameters for investigating correlations in the neighbourhood of T_{NI}.

Potential parameters	$\kappa = 3$, $\kappa' = 5$, $\mu = 1$, $\nu = 3$
Simulation timestep	$\Delta t = 0.004$
Moment of inertia	$I = 1.0$
Density	$\rho = 0.3$
Simulation algorithm	Domain decomposition (GBMEGA)

	Run length (reduced units)	
Temperature	Equilibration	Production
$T = 4.00$	20	20
$T = 3.80$	20	20
$T = 3.70$	20	20
$T = 3.60$	120	50
$T = 3.55$	260	200
$T = 3.50$	260	260
$T = 3.47$	150	–
$T = 3.45$	160	100

4.4 Static orientational structure

We calculated the spherical harmonic components $h_{mnx}(r)$ in the molecular frame up to order $l_{\max} = 8$. This involved accumulating histograms over all pairs of molecules, out to a cutoff distance of approximately half the box length L. In practice, the all-pairs sum for this long range calculation is rather expensive, so we only analysed every 1000th timestep. The short range correlation functions, for $r < 5\sigma_0$ were computed at intervals of 100 timesteps for better statistics, using a link cell algorithm. After combining short- and long-ranged histograms and averaging over the entire production run, we used the methods outlined in section 4.2.3 to calculate the direct correlation function.

Several components of the the pair correlation function $h(1,2)$ are shown in figure 4.5 (i)-(iii). The orientationally averaged centre-centre pair function $h^{000}(r)$ varies only slightly as the transition is crossed. Of more interest is the laboratory-frame $h^{220}(r)$ component, which measures correlations of the $P_2(\mathbf{e}_1 \cdot \mathbf{e}_2)$ type. As expected, within the isotropic phase this function decays to zero at $r = \infty$, and as the transition is approached its range increases; below T_{NI}, the range becomes infinite. The long range decay at the isotropic state points fits well to an Ornstein-Zernike form $h^{220} \propto \exp(-r/\xi_2)/r$. Correlation lengths ξ_2 extracted from this expression for each temperature are plotted in figure 4.4 (i). We find that the apparent divergence of the correlation length agrees quite well with Landau-de Gennes theory $\xi_2^{-2} \propto (T - T^*)$, with $T^* = 3.47 \pm 0.02$.

The higher order components such as $h^{440}(r)$ also become more long ranged as the transition is approached, although the amplitude of the long range decay is smaller. They also exhibit more short-range structure.

In figure 4.6 we show the behaviour of corresponding moments of the direct correlation function $c(1,2)$. The most important point is that all the $c^{mnl}(r)$ remain finite in range through the transition. In fact, the changes in c^{220} and c^{440} in the temperature range $3.45 \cdots 4.00$ are quite small - the values at $r = 0$ become more negative and the first peaks more pronounced with decreasing temperature. These small changes alone are responsible for the dramatic increase in the range of $h(1,1)$.

We can understand this as follows. Defining suitably normalised integrals

$$h^{(l)} = \rho(2l+1)^{-1/2} 4\pi \int_0^\infty \mathrm{d}r\; r^2\; h^{ll0}(r) \tag{4.11}$$

$$c^{(l)} = \rho(2l+1)^{-1/2} 4\pi \int_0^\infty \mathrm{d}r\; r^2\; c^{ll0}(r) \tag{4.12}$$

the instability criterion for the isotropic phase [92–94] may be expressed as $c^{(l)} \to 1$, $l = 2, 4, 6 \ldots$. This is related to an *exact* factorisation of the Ornstein-Zernike equation at zero wave-vector [95] which may be expressed

$$h^{(l)} = \frac{c^{(l)}}{1 - c^{(l)}} \,. \tag{4.13}$$

Thus, $c^{(l)} \to 1$ coincides with the divergence of the integral in eqn (4.11), and hence divergence of the range of $h^{ll0}(r)$. The dependence of $c^{(2)}$ and $c^{(4)}$ on temperature is shown in figure 4.4 (ii). Again, these functions are consistent with T_{NI} lying between $T = 3.45$ and $T = 3.50$.

Figure 4.5: Behaviour of selected components of the pair correlation function, at temperatures close to T_{NI}.

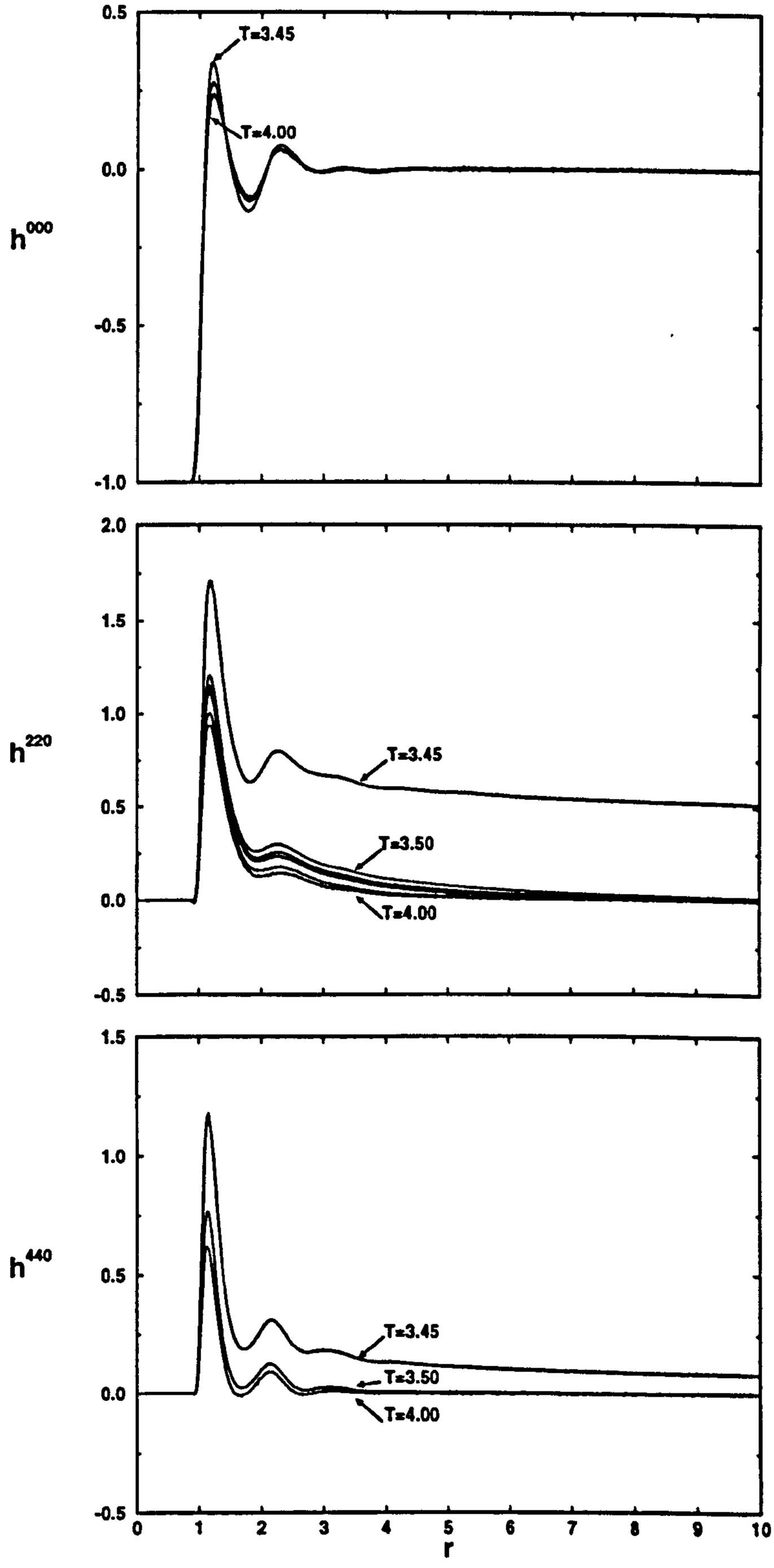

Figure 4.6: Behaviour of selected components of the direct correlation function, c^{mnl} at temperatures near T_{NI}.

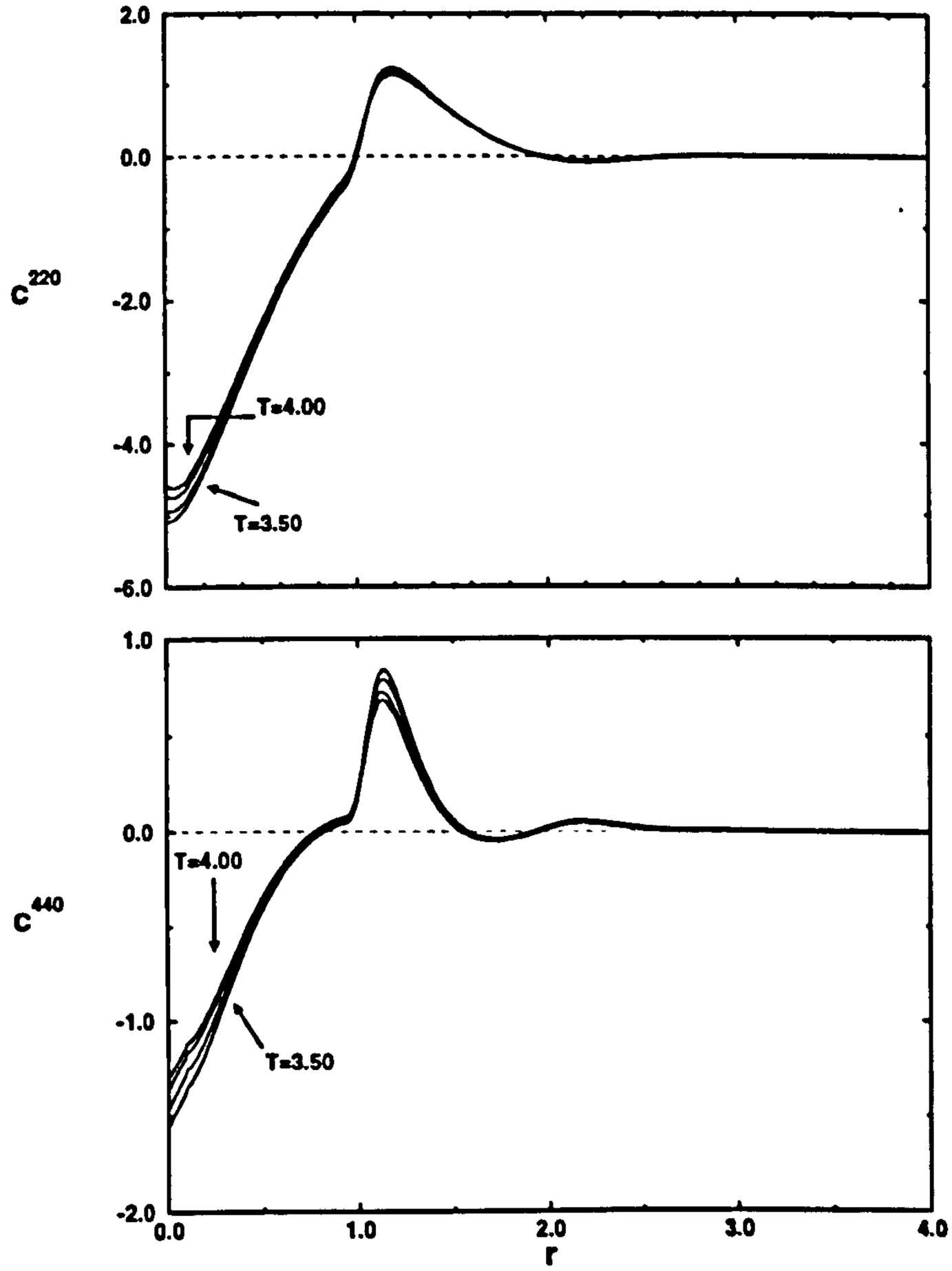

4.5 Reorientation dynamics

In our calculations of the elastic constants (chapter 3), we measured static fluctuations in the reciprocal space order tensor. Collective reorientation is described by the dynamics of this tensor, i.e. by

$$C(\mathbf{k},t) = \sum_{\alpha,\beta} \langle Q_{\alpha\beta}(-\mathbf{k},0) Q_{\alpha\beta}(\mathbf{k},t) \rangle \ , \tag{4.14}$$

where

$$Q_{\alpha\beta}(\mathbf{k},t) = \sum_{i=1}^{N} \frac{3}{2} \left(e_{i\alpha} e_{i\beta} - \frac{1}{3}\delta_{\alpha\beta} \right) \exp(i\mathbf{k}\cdot\mathbf{r}_i) \ . \tag{4.15}$$

Summation over indices is appropriate, provided we restrict our attention to the isotropic phase. In this case, $C(\mathbf{k},t)$ is radially symmetric with respect to $\mathbf{k}$. We compute $C(k,t)$ in the following way:

- We first compute components of the reciprocal space order matrix, $Q_{\alpha\beta}(\mathbf{k})$ for each configuration, for the set of wavevectors $\mathbf{k} = (n_x\mathbf{x} + n_y\mathbf{y} + n_z\mathbf{z})2\pi/L$, where $n_x = -10\cdots10$, $n_y = -10\cdots10$, $n_z = 0\cdots10$.

- For each $\mathbf{k}$, we calculate the correlation function $C(\mathbf{k},t)$, accumulating over a number of statistically independent time origins.

- By averaging over equivalent $\mathbf{k}$ vectors, we obtain estimates of the errors on $C(k,t)$.

Except at large values of k we find that $C(k,t)$ decays exponentially with time:

$$C(k,t) = A(k) \exp\left[-t/\tau(k)\right] \ , \tag{4.16}$$

and that both τ and A are proportional to k^{-2}, for k not too large. The proportionality constants are quite insensitive to temperature, except at very low values of k, where the decay times increase as the temperature is lowered. In particular, at $k = 0$, we find that $\tau(0) \propto (T - T^*)^{-2}$, in agreement with Landau-de Gennes theory. These results, which we represent graphically in figure 4.7, lead us to conclude that reorientational dynamics is unaffected by the transition, except at the very longest wavelengths.

Figure 4.7: Correlation times for the relaxation of orientational fluctuations. (i) shows the inverse correlation time as a function of k^2 for $T = 3.50$; the results for the higher temperatures are very similar when plotted this way. Dynamical slowing down in the neighbourhood of the transition is seen only at the lowest wavevectors. This is made clearer in (ii), which shows the wavevector dependence of the correlation time, for temperatures $T = 3.60$ (diamonds), $T = 3.55$ (squares) and $T = 3.50$ (circles).

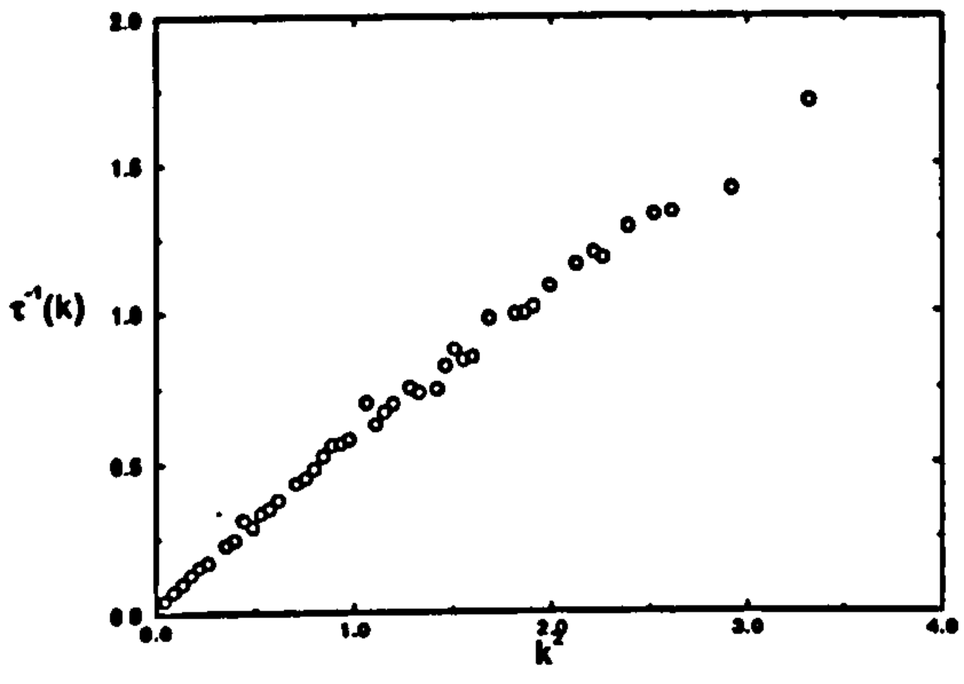

(i)

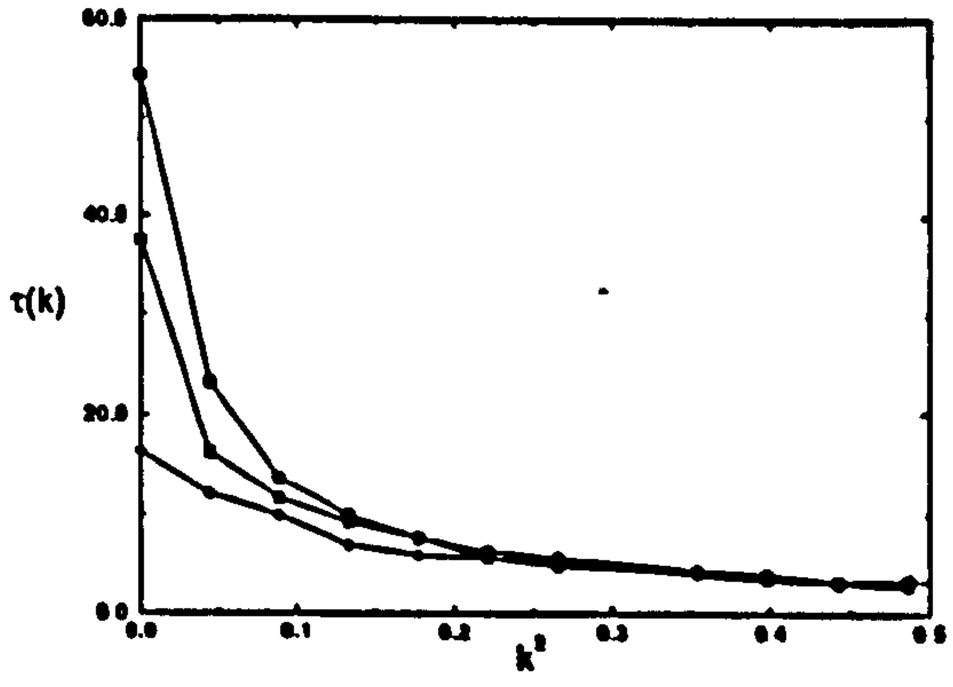

(ii)

4.6 Kinetics of a nematic-isotropic quench

Recently, dynamic scaling theories have been developed [101] which describe the growth of correlations when a system whose order parameter has a continuous symmetry is quenched from the disordered into the ordered phase, for example from the isotropic into the nematic. A key prediction of these theories is that at sufficiently large times, the correlation functions obey scaling relations:

$$C(r,t) = f(r/\xi(t)) \tag{4.17}$$

where f is a scaling function. The evolution of $C(r,t)$ at late times is thus characterised by the increase of a single length scale, ξ.

The observation of the true scaling limit is all but out of reach in molecular scale simulations, since it depends on the nature of the topological excitations which can

Figure 4.8: The correlation function h^{220} at several stages of the quench of the $N = 64000$ system. The times are in reduced units.

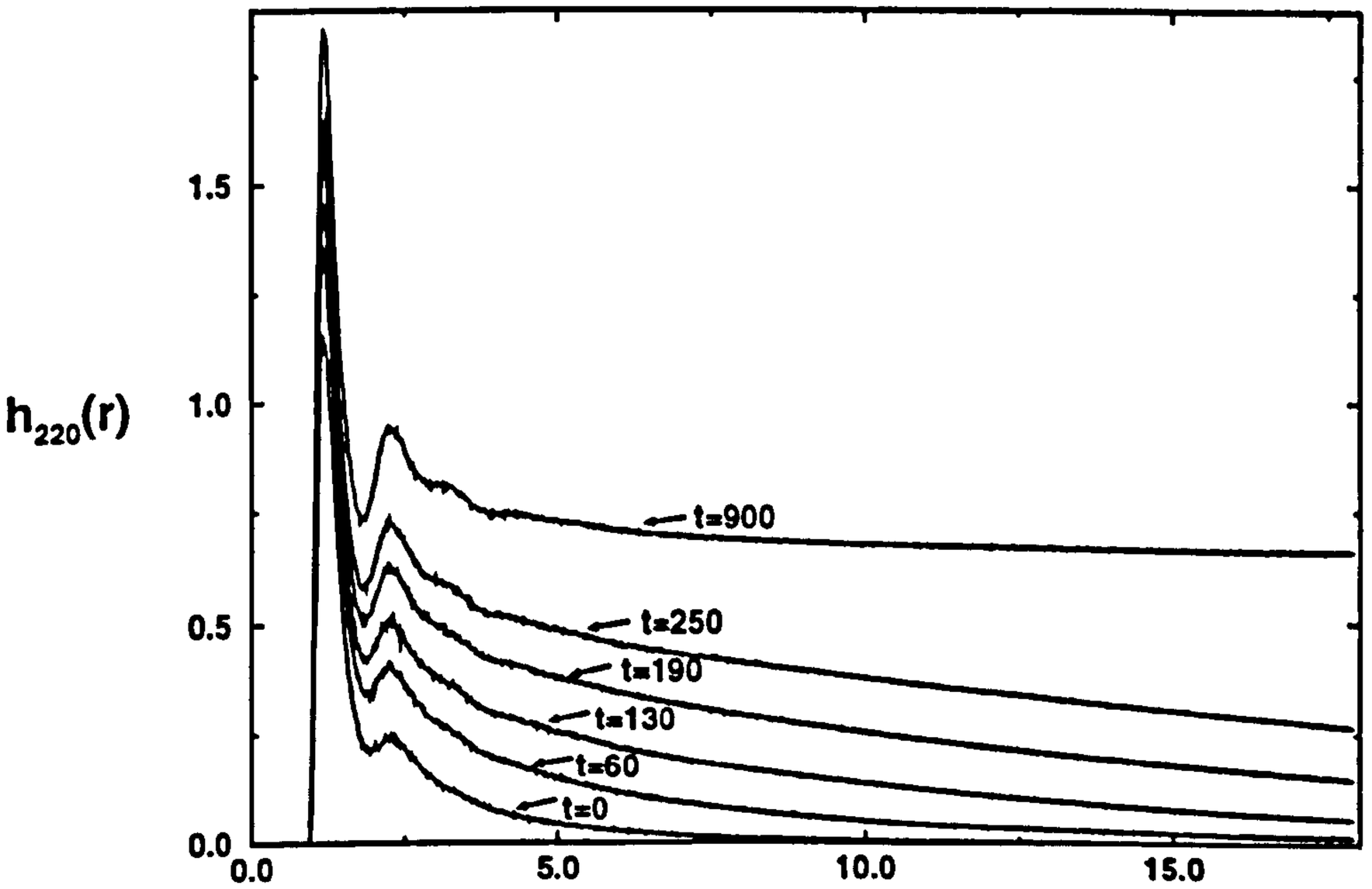

occur in the ordered phase. In a nematic, for instance, these are the disclination lines which give the phase its turbid appearance. Very large system sizes and lengths of run are needed to observe these objects, and so far, studies on this scale are only possible in lattice systems. However, it is still interesting to investigate the timescales associated with growth of structure in a molecular model, and we have made a modest attempt at doing this.

We used a system size of 64000 molecules, subject to the usual periodic boundary conditions. The potential, timestep and other simulation parameters were exactly as in the equilibrium simulations reported above. After an equilibration run of length 50000 timesteps in the isotropic, at the temperature 3.65, we quenched the system suddenly to the nematic state point $T = 3.40$. In figure 4.10, we plot two measures of the degree of orientational ordering, namely the nematic order parameter for

the whole system, and the average of the order parameter computed separately for $5 \times 5 \times 5$ subcells and then averaged. The former remains very small throughout the equilibration period, but the non-vanishing subcell average shows that on the scale of a single subcell (about the same as the system size studied by Berardi *et al* [23]), there is some orientational order even at this temperature. Both quantities rise steadily after the quench, and they reach the same plateau value of around 0.55 after around 125000 timesteps, indicating that even this large system rapidly reaches a monodomain state. This is the case, as the snapshot of the final configuration, figure 4.9 shows. The monodomain state is reached quite rapidly, as can be seen in the time evolution of the second rank correlation function $h^{220}(r)$, plotted in figure 4.8.

4.7 Conclusions

Our simulations of a large system of Gay-Berne particles have shown that, close to the phase transition, system size effects are important. In particular, the nematic-isotropic transition appears at a lower temperature than in a smaller system. We have studied the behaviour of both the pair correlation function $h(1,2)$ and the direct correlation function $c(1,2)$ in the vicinity of T_{NI}. We find that the range of orientational correlations grows as T_{NI} is approached, and that the temperature dependence is consistent with the Landau-de Gennes picture. However, even in the large system size studied, we were not able to determine the apparent divergence temperature T^* sufficiently accurately to distinguish it from T_{NI}. The dramatic increase in the correlation length is the result of quite subtle changes in the *direct* correlation function.

Our measurements of collective orientational correlation functions demonstrate that pretransitional slowing down of reorientation does occur, but at least at the temperatures we studied, this effect was seen only at wavelengths of order $10\sigma_0$. The decay times for fluctuations with shorter wavelengths than this obeyed the law $\tau^{-1} \propto k^2$. Our preliminary simulations of the kinetics of an isotropic $\rightarrow$ quench do not allow us to make contact with scaling theories. They show that even for large

system sizes there is no splitting into domains with slowly evolving boundaries. In much larger systems, we might expect to see this behaviour. In this event, it would be very interesting to use techniques such as those employed in chapter 5 in order to characterise the structure and dynamics of the topological defects.

Figure 4.9: Snapshot of the final configuration of the quench. Colour coding represents orientation, with molecules lying along the system director coloured red.

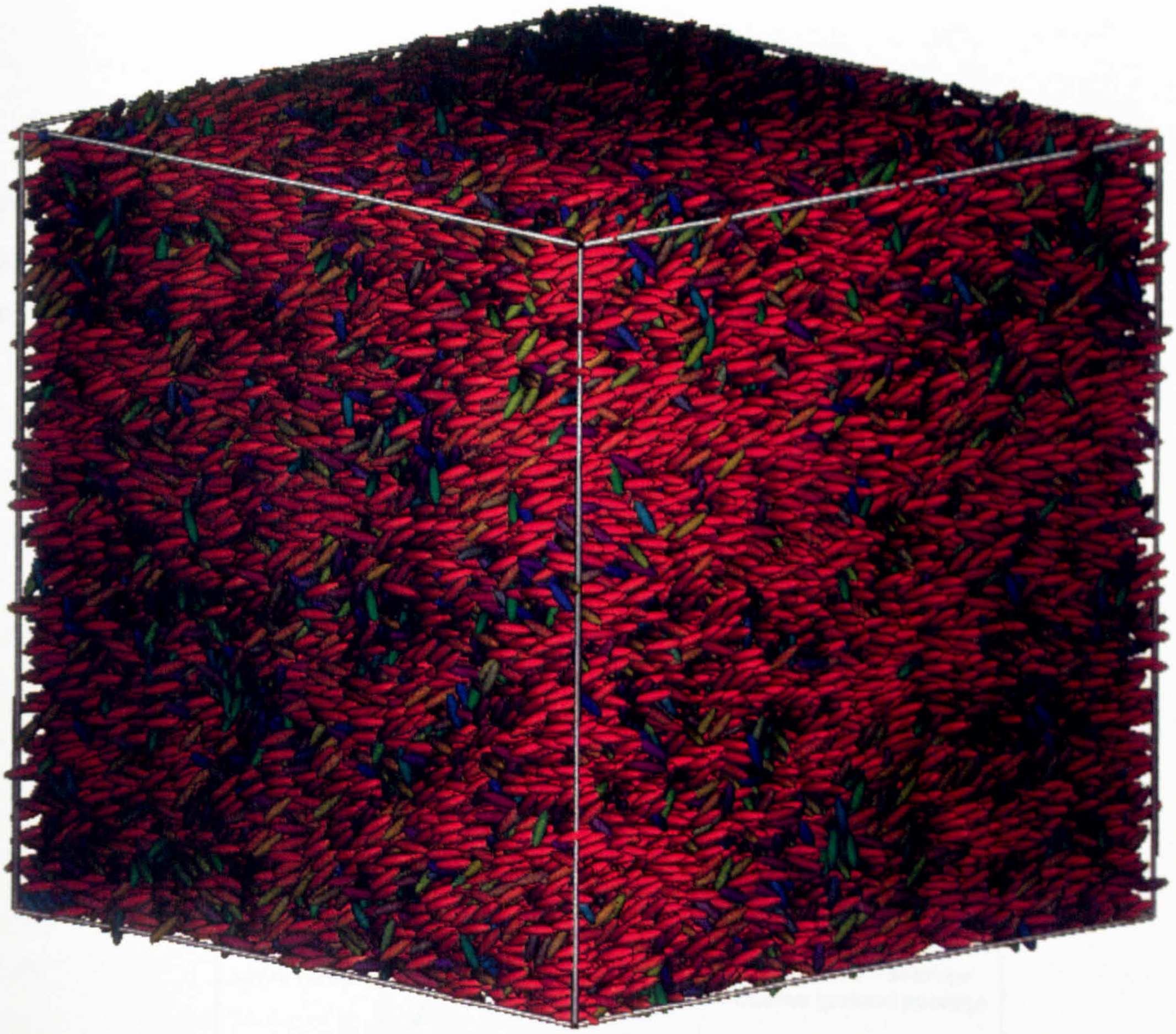

Figure 4.10: Graph showing the growth of nematic order in the $N = 64000$ system. We show the order parameter for the entire system, and also the average value of P_2 calculated for individual subcells of side $\approx 12\sigma_0$.

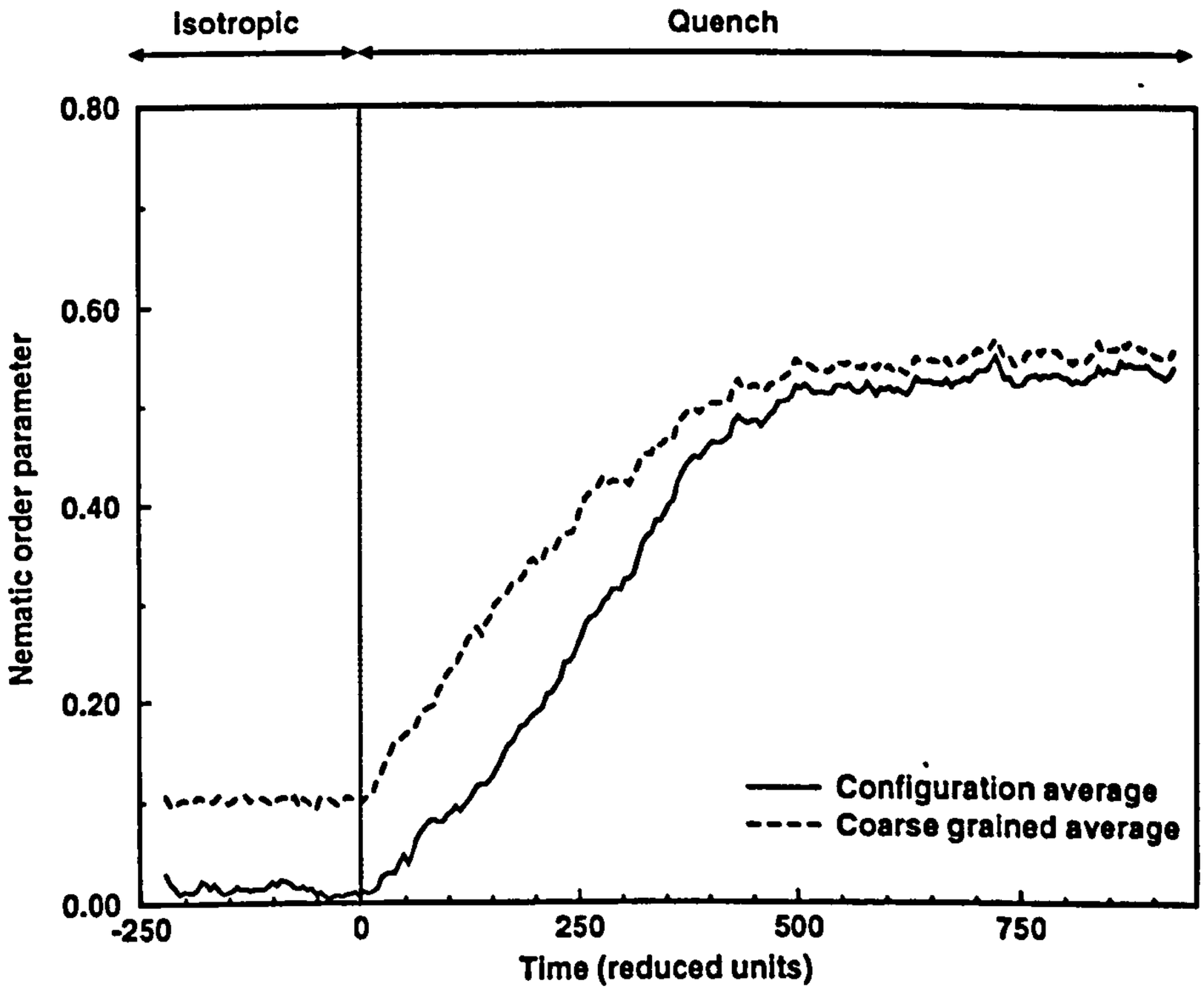

Chapter 5

Computer Simulation of the Twist Grain Boundary Phase

5.1 Introduction

In 1989, Renn and Lubensky (RL) predicted the occurrence of a novel liquid crystalline phase in systems of chiral mesogens, the twist grain boundary, TGB phase [102]. This discovery, together with the first experimental observation of the phase which was made at around the same time, generated a great deal of interest, both for their own sake and because of a close analogy between these systems and superconductors. In this chapter we present the results of extensive molecular dynamics simulations of a system of Gay-Berne molecules subject to twisted periodic boundary conditions. The translational and orientational ordering we observe in our system correspond qualitatively with the RL picture, and so we believe that this work represents the first computer simulation of the twist grain boundary phase. A particularly interesting aspect of the TGB structure is the topology of the smectic layers at the interface between regions of different smectic orientations. In the RL theory, each interface contains a regular array of twist defects. We have developed a novel technique for searching through molecular configurations for this kind of defect, and have found several convincing examples in configurations at the lowest two temperatures we studied. We have attempted to characterise the ordering in the neighbourhood

of these defects, and to estimate the defect core radius.

The organisation of this chapter is as follows. In section 5.2 we give an outline of the RL theory, qualitatively describe the TGB structure and comment briefly on the relationship with superconductivity. Section 5.3 introduces the model and simulation techniques used. The TGB phase is distinguished by the behaviour of the molecular orientation and smectic layer normal as a function of distance along the twist direction. In section 5.4 we define the profiles of nematic order parameter and structure function which we use to characterise this behaviour, and present these results for each of the statepoints studied. This is followed in section 5.5 by a discussion of diffusion profiles, which we measure primarily to check that no parts of the system have solidified. In section 5.6 we describe our simulated annealing technique for finding defects in molecular configurations, and apply this to investigating the structure of the domain boundaries. We conclude in section 5.7 with a summary of our results, some comparisons with experiment, and possible directions for future work.

5.2 Theoretical and experimental background

The Renn-Lubensky theory [102] was motivated by a close correspondence between the mathematical description of the normal-metal to superconductor transition and that of the nematic to smectic *A*. This correspondence, which was first noted by de Gennes [1] arises from the common character of the symmetry breaking in the two transitions. In the superconducting case the ordering field is the complex amplitude of Cooper pairs, $\psi(\mathbf{r})$. In a smectic, the ordering field represents the periodic modulation along the layer normal N of the nematogen density. This too is complex, since the modulation has both an amplitude and a phase; the deviation of the local single-particle density from its average value is

$$\rho(\mathbf{r}) - \langle\rho\rangle = \psi(\mathbf{r}) + \psi^*(\mathbf{r})\,. \tag{5.1}$$

Phenomenological mean field theories of a superconductor in zero magnetic field and the N-Sm A transition for uniaxial molecules are based on a free energy func-

tional $\mathcal{F}$ of the ordering field. Imposing the relevant symmetry on this functional (gauge invariance in the case of superconductivity, rotational invariance in liquid crystals) leads to identical mathematical forms for $\mathcal{F}[\psi(\mathbf{r})]$, so there is complete correspondence between the theories. RL extended the superconducting analogy to include the effects of molecular chirality. They modelled this by including a term in the free energy density coupling to the twist in the director field, $\mathbf{n} \times (\nabla \times \mathbf{n})$. The superconducting analogue of this term is the coupling between the vector potential and an external magnetic field. In superconductors, two regimes of behaviour can result when such a field is introduced. Which regime is followed depends on the ratio of two length scales, namely the correlation length ξ and the penetration depth λ_2 - these in turn depend on the phenomenological constants in the free energy. In strongly correlated (type I) superconductors, where the Ginzburg parameter $\kappa_G = \lambda_2/\xi < 1/\sqrt{2}$, there is just one critical magnetic field h_c. Below h_c, in the Meissner state, the magnetic field is *expelled*, and decays exponentially over a distance λ_2 inside the superconductor. At $h = h_c$ there is a first order transition to the normal state, and fields above this value are able to penetrate the material completely and uniformly. In weakly correlated (type II) superconductors, for which $\kappa_G > 1/\sqrt{2}$, the behaviour is entirely different: there are now two critical fields, h_{c1} and h_{c2}. For $h < h_{c1}$ we have the Meissner state, and above h_{c2} the normal metal. There is now a new intermediate state between lower and upper fields h_{c1} and in which there is partial penetration of magnetic flux. Unlike in the normal metal however, the magnetic field in this state is not uniform; but is concentrated on lines running parallel to the applied field. These lines, or vortices, are topological defects in the order parameter field: the density of Cooper pairs $|\psi|^2$ goes to zero over a length $\approx \xi$, and the phase of ψ undergoes a rotation of 2π around each vortex. When interactions between vortices are taken into account, the most energetically favourable arrangement is found to be the *Abrikosov state* in which the line defects lie on a triangular lattice.

In the RL theory, all these ideas carry over to the liquid crystal case. The concepts of flux expulsion and penetration have straightforward interpretations: in the presence of molecular chirality the thermodynamically favoured disordered phase is

no longer an untwisted nematic, but a cholesteric phase N^* in which the director rotates helically with a pitch determined by the rotatory power of the constituent molecules. This twist cannot penetrate very far into a homogeneously ordered smectic A since this would involve a large bending energy of the smectic layers - for this reason the smectic is said to *expel twist*. As the chirality is increased (for instance by increasing the concentration of chiral solute) then eventually the cost of destroying the translational ordering is outweighed by the free energy gained by reintroducing twist. In type I systems there is just one critical chirality, h_c, above which the N^* phase is regained. RL predicted the possibility of a liquid crystal analogue of type II behaviour, and hence an intermediate *twist grain boundary* state in which the twist is only partially expelled and a degree of translational ordering remains. Sketches of the phase diagrams in the type I and type II cases are shown in figure 5.1.

The structure of the *twist grain boundary* phase, which we illustrate in figure 5.2, consists of a set of domains along the twist axis. Within each domain there is smectic-like 1D translational order, and the director **n** lies almost parallel to the layer normal N. At each domain boundary though, both **n** and N undergo a discrete rotation through an angle $\Delta\theta$. This rotation is mediated by a set of equispaced, parallel twist dislocations with orientation between the layer normals on the two sides of the interface. As in the superconducting case, these are topological defects in the ordering field ψ; on encircling one of the defects one picks up a phase change of 2π in ψ, so that the arrangement of the smectic layers in the vicinity of each defect resembles a spiral. In the RL theory, the system is assumed infinite in the directions perpendicular to the twist, and the defects form a regular array of infinite lines distance l_d apart. The layer spacing away from the defects is d_0.

As the defect line is approached, the degree of translational ordering $|\psi|^2$ tends to zero over some radial distance $\approx \xi$. An idealised representation of the geometry of a single interface is shown in figure 5.3.

Just at the same time that the theory of the TGB phase was proposed, Goodby and coworkers [103] discovered a novel chiral smectic phase in the series of chiral mesogens nP1M7, which have the general formula:

Figure 5.1: Schematic phase diagrams in the temperature T chirality h plane. In a type I smectic, the effect of molecular chirality is to postpone the cholesteric-smectic transition; for a given temperature $T < T_{NA}$ there is a critical chirality h_c above which the smectic ordering is destroyed. In type II materials, the TGB phase intervenes between the cholesteric and the smectic, and is bounded by lower and upper critical chiralities, h_{c_1} and h_{c_2}.

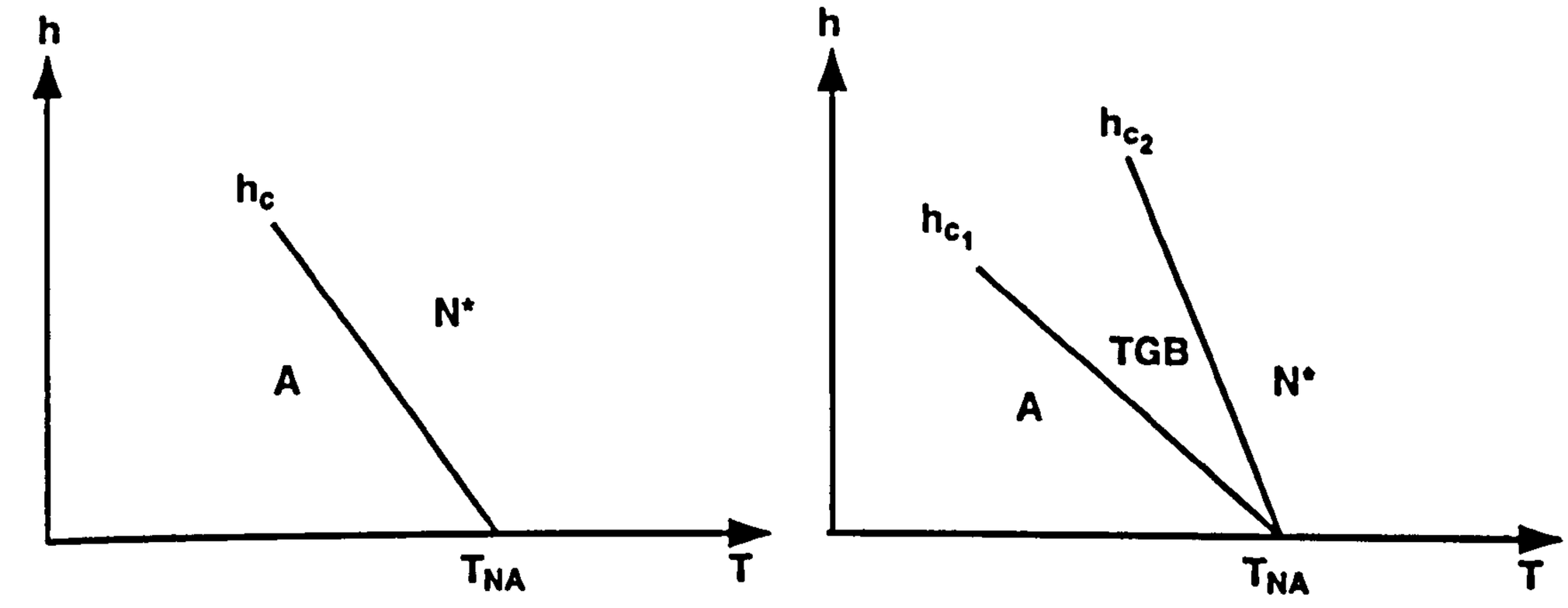

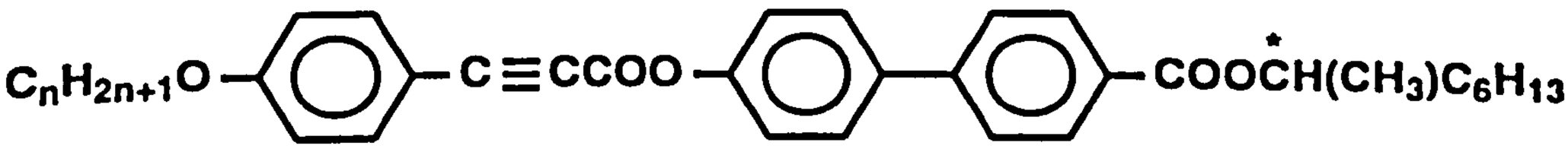

The asterisk indicates the position of the chiral centre. Optical micrographs of textures and small angle X ray scattering measurements indicated that several homologues of this series undergo a phase transition from a smectic-C^* into a phase with both helical orientational order and smectic order, which led to speculation that this was the first experimental observation of the TGB phase. Subsequently the structure of the new phase was investigated more thoroughly: the variation of chiral pitch with temperature was determined from the position of troughs in the transmission spectra for circularly polarised light. High resolution X-ray diffraction studies were able to measure the static structure factor, and hence provide an estimate of the smectic layer spacing, a lower bound on the range of translational correlations within smectic domains, and the width of domain boundaries [104–106].

Figure 5.2: Domain structure of the TGB phase, showing the grain boundary angle $\Delta\theta$, and domain width l_s.

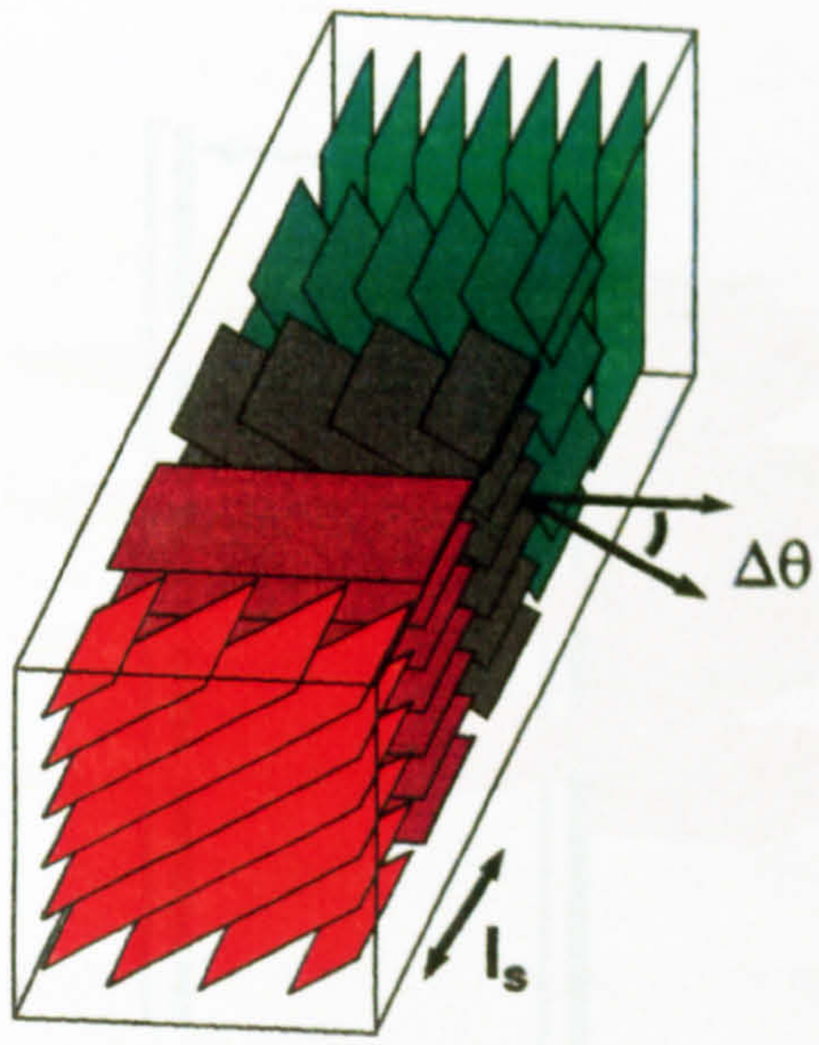

Finally, electron micrographs of freeze fracture specimens [107] provided estimates of the grain boundary angle $\Delta\theta$ and the defect spacing l_d. Cumulatively, these results confirmed the TGB structure as a convincing model of the new phase. The possibility of TGB-like structures in *achiral* liquid crystals was first put forward by Patel [108] in relation to experiments on a liquid crystal in a twist cell, i.e. in a sample bounded by plates favouring molecular alignment along the x direction on the top surface and along y on the bottom. The twist in the director field about the z axis induced by the director pinning can be detected as a non-zero transmitted intensity when the cell is placed between crossed polarisers. Patel found that the twist persists below T_{NA}, whilst at the same time the presence of focal conic textures suggests smectic like ordering. Strain-induced TGB structures have also been observed in suspensions of the bacteriophage fd [109]. The comparatively large length of fd particles in this case - about $8800\mathring{A}$ - allows direct observation of the block domains via differential interference contrast microscopy.

Figure 5.3: Idealised structure of an interface between two domains in the TGB phase.

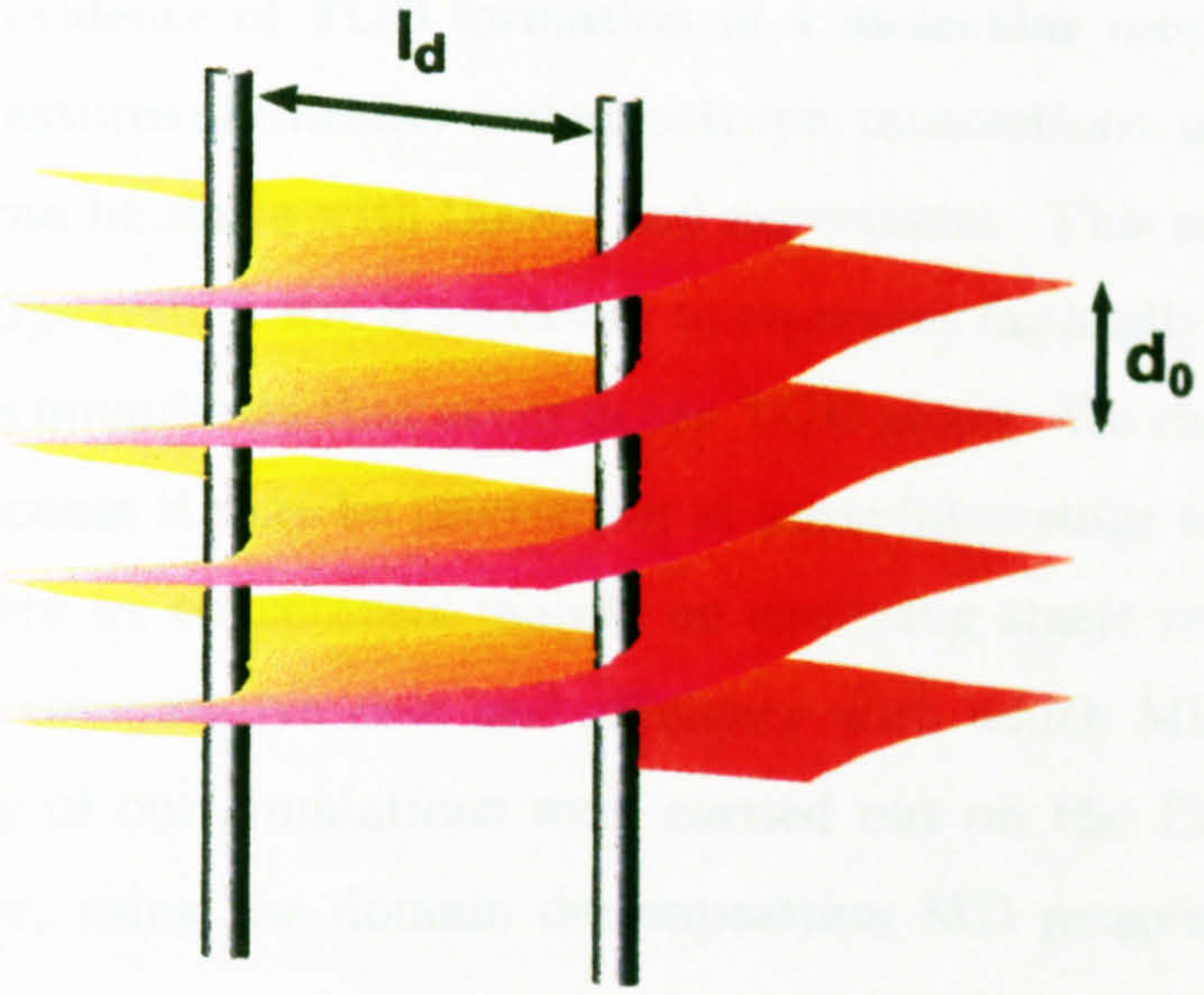

5.3 Simulation method

Several approaches to the modelling of the TGB system might be considered. One possible avenue of study would be to attempt an exact numerical solution of the mean field theory, i.e. minimisation of the RL free energy functional $\mathcal{F}[\psi, \mathbf{n}]$, without any of the simplifying assumptions made in the analytical treatment, such as confinement of the director to the xy plane, and equality of the splay and bend elastic constants. Such calculations might be able to establish how significant an effect these assumptions have on the behaviour of the system. The reasonableness of the assumptions is not in doubt however, given the qualitative agreement between the theory and experimental results. A far more interesting topic is the question of how the TGB region is divided into states with different grain boundary angles $\Delta\theta$ and domain lengths l_d. This is a subtle issue, since the lock-in corrections which occur when $\Delta\theta$ is a rational multiple of 2π are difficult to treat analytically. Physically, these lock-in effects can be thought of as small terms in the free energy which favour states where the cholesteric pitch is commensurate with the rotation of the smectic

domains. A thorough numerical investigation of these effects would probably be very computationally expensive, even within a coarse-grained lattice model approach.

Rather than beginning with a phenomenological free energy functional, in the present work we look for evidence of TGB formation in a molecular model which incorporates the essential features of chirality and anisotropic interactions, and see to what extent comparisons can be made with theory and experiment. This represents quite a challenge, since a large system size is necessary to represent faithfully complex structures such as the grain boundaries that occur in the TGB phase. We choose MD rather than MC, partly because it may be interesting at some later stage to look at the dynamics (although here we concentrate mainly on analysing static structure), and partly because of the comparative ease and efficiency with which MD can be parallelised. The majority of our simulations were carried out on the Edinburgh t3d parallel supercomputer, using the domain decomposition MD program which we describe in chapter 2.

5.3.1 Definition of model

A fully atomistic simulation of a chiral mesogen as complex as nP1M7 is clearly out of the question, at least at the system size we need in order to study the TGB phase. The use of a soft potential is preferred over reference hard-particle systems such spherocylinders, since parallelisation of hard-particle MD is difficult. We therefore use another parametrisation of the Gay-Berne model, this time with $\kappa = 4.4, \kappa' = 20, \mu = 1, \nu = 1$, and a spherical cutoff at $r_c = 5.5$. Diagrams showing the the dependence of this potential on the pair-pair separation for four relative orientations of the molecules are shown in figure 5.4. It is worth remarking that this particular parametrisation is somewhat peculiar in that the well depth at the equilibrium separation in the side by side arrangement is less than for the end to end and tee configurations. We choose this model since previous studies [110] have shown that there is a large region in the phase diagram where the smectic A phase is stable. At a reduced density of $\rho^* = 0.16$, the phase transitions occur at the following temperatures:

T_{IN}	Isotropic	$\rightarrow$	nematic	$T^* = 1.6$
T_{NA}	Nematic	$\rightarrow$	smectic	$T^* = 1.1$
T_{AS}	Smectic	$\rightarrow$	solid (?)	$T^* = 0.6$

The Gay-Berne potential itself is achiral: for any fixed $\mathbf{e}_i$ and $\mathbf{e}_j$, the isopotential surfaces of $U_{ij}^{GB}(r, \hat{\mathbf{r}}, \mathbf{e}_i, \mathbf{e}_j)$ have $D_{\infty h}$ symmetry. Clearly this potential on its own will not lead to any chiral phases. In order to make contact with the TGB theory and experiment we need some way of modelling molecular chirality. One approach is to add a suitable term to the pair potential, and indeed this method has been used in some simulation studies of chiral systems. From our point of view, this technique has the distinct advantage that the chirality can be adjusted continuously. Another method is to connect two or more Gay-Berne particles together with rigid bonds to form achiral "molecules". The introduction of chirality at the microscopic level is not the only issue in computer simulations however - another point which needs to be considered is the question of how the spatial dependence of the orientational ordering is constrained by the boundary conditions. Suppose for example that at a certain density, temperature and chirality the thermodynamically stable state of the model is a cholesteric, so that in equilibrium the director field is of the form

$$\mathbf{n} = \hat{\mathbf{a}} \cos(\mathbf{q} \cdot \mathbf{r}) + \hat{\mathbf{b}} \sin(\mathbf{q} \cdot \mathbf{r}) \,, \tag{5.2}$$

where $\mathbf{q}$ is the twist axis, $\lambda = 2\pi/|\mathbf{q}|$ is the equilibrium pitch, and $\hat{\mathbf{a}}$ and $\hat{\mathbf{b}}$ are mutually perpendicular to $\mathbf{q}$. The periodic modulation in the director field must be commensurate with the periodic boundary conditions: in a cuboidal box this means that λ is restricted to the discrete set of values

$$\lambda = \frac{1}{\sqrt{\left(\frac{n_x^2}{L_x^2} + \frac{n_y^2}{L_y^2} + \frac{n_z^2}{L_z^2}\right)}} \,. \tag{5.3}$$

The equilibrium pitch will not in general be accessible to a computer simulation with fixed box dimensions. Moreover, states with different twist wavevectors are separated by a large free energy barrier, and so transitions between them are rare events. One way in which these problems can be overcome is to conduct the simulations at constant pressure, and allow the dimensions of the simulation box

to change, in order to introduce continuous paths between states of different pitch. Typically, this is done by incorporating constant-pressure Monte-Carlo moves into the dynamics [34]. At regular intervals, one attempts a uniform expansion or compression of the configuration along a randomly chosen axis. The change in potential energy $\Delta\mathcal{V}$ resulting from the attempted move is calculated, and the move accepted with a probability

$$P_{\text{accept}} = \begin{cases} 1 & \Delta H \leq 0 \\ e^{-\Delta H/k_B T} & \Delta H > 0 \end{cases} \tag{5.4}$$

where the change in enthalpy,

$$\Delta H = \Delta\mathcal{V} + P\Delta V - Nk_B T \log(1 + \Delta V/V). \tag{5.5}$$

These Monte-Carlo style volume moves in conjunction with molecular dynamics steps generate a phase space trajectory which correctly samples the NPT ensemble, and at least in principle they allow the director field to reach a thermodynamically stable state. In practice though, this state may still be reached only very slowly if the acceptance rate for the MC moves is very low. We expect this to be the case in the TGB phase, where reorientation of the chiral pitch axis involves thermodynamic forces coupling to both orientational and translational degrees of freedom. The MC moves also suffer from two other disadvantages. Firstly, the fictitious moves in phase space mean that we lose the real dynamics of the system. For our present purposes, this would not be too much of a problem, since we are interested primarily in static structure. Secondly, and more inconveniently, it is difficult to define and average the spatial profiles we shall be using to characterise the ordering in the twisted system, if the box shape and chiral axis are continually changing.

For these reasons, we abandon the idea of trying to reach an equilibrium state at constant ρ, T and h. Instead, we prepare a configuration with a chiral pitch consistent with the periodic boundary conditions, and conduct the simulation at constant L_x, L_y and L_z. We anticipate that the chiral axis and pitch will be stable over any reasonable length of run. In fact, a twisted state can usually be maintained indefinitely even when the potential is achiral, since escape of the director field

towards uniform alignment involves crossing a free energy barrier of states with large splay/bend energy. As we shall see, this stability holds for the variant of the Gay-Berne potential we use here.

Figure 5.4: The cut and shifted Gay-Berne potential used in the TGB simulations. The graphs show $V_{ij} = v^{\mathrm{GBc}}(\mathbf{e}_i, \mathbf{e}_j, \mathbf{r}_{ij})$, with molecule i at the origin and molecule j in the xy plane, (i) for $\mathbf{e}_i = \mathbf{e}_j = \mathbf{x}$, (ii) for $\mathbf{e}_i = \mathbf{z}$ and $\mathbf{e}_j = \mathbf{x}$.

(i)

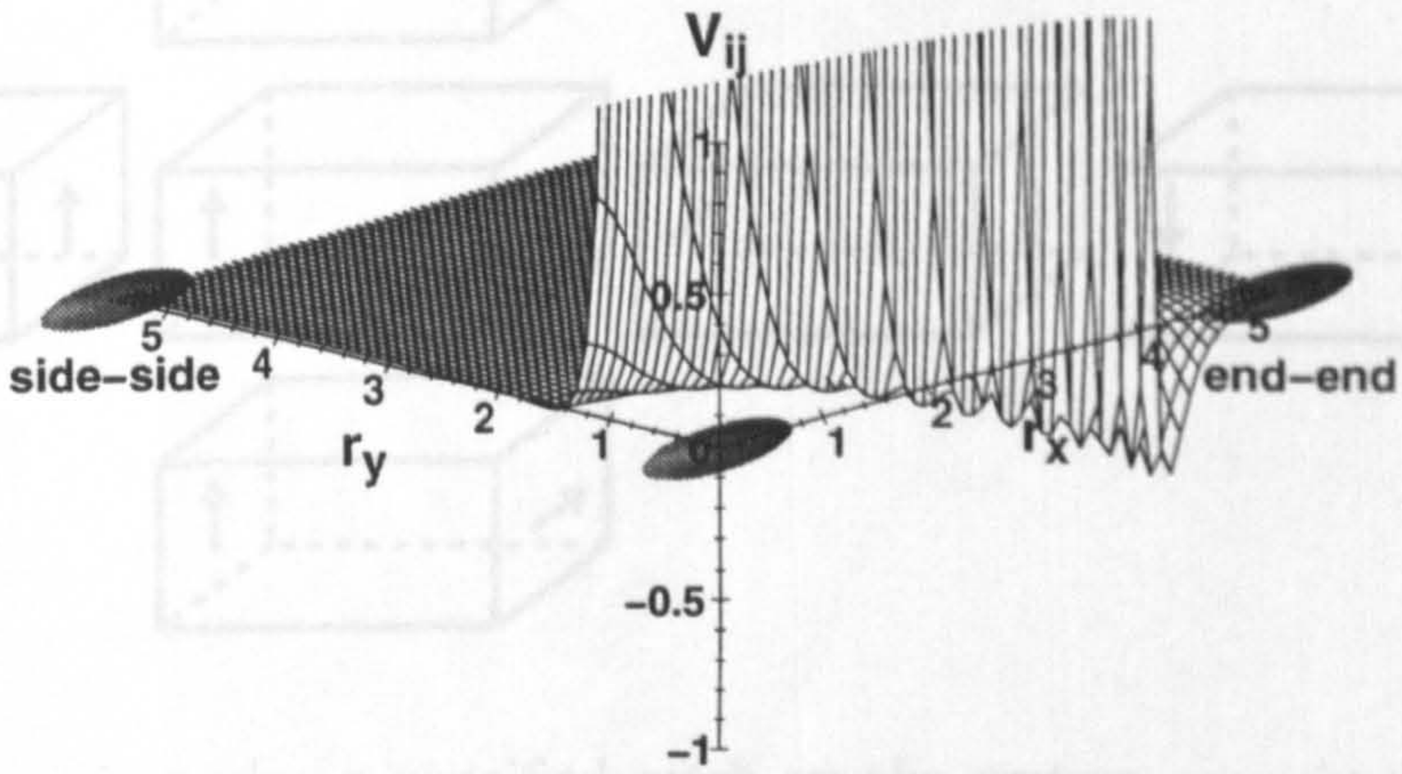

(ii)

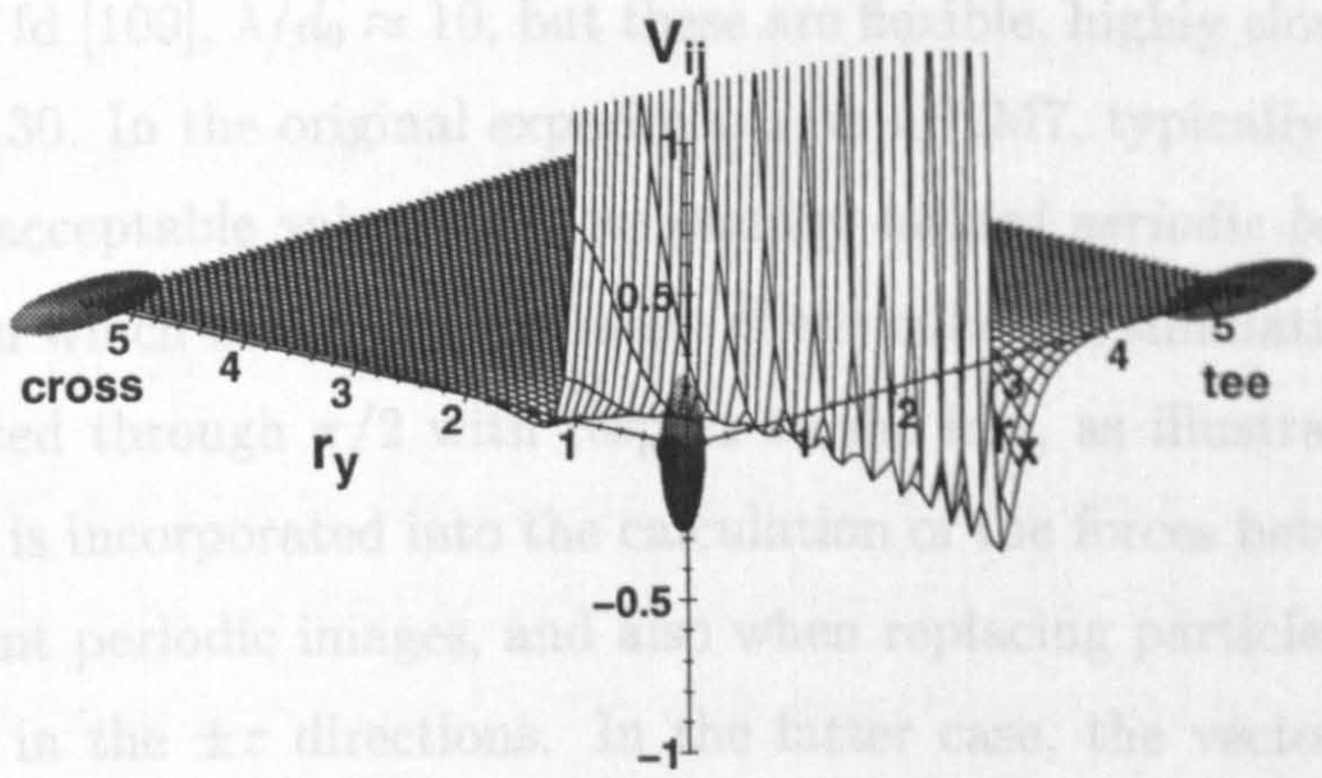

Figure 5.5: Twisted periodic boundary conditions. Periodic images displaced in the z direction with respect to the original simulation box, shown in bold, are rotated a quarter turn about z. In the x and y directions, the usual boundary conditions apply.

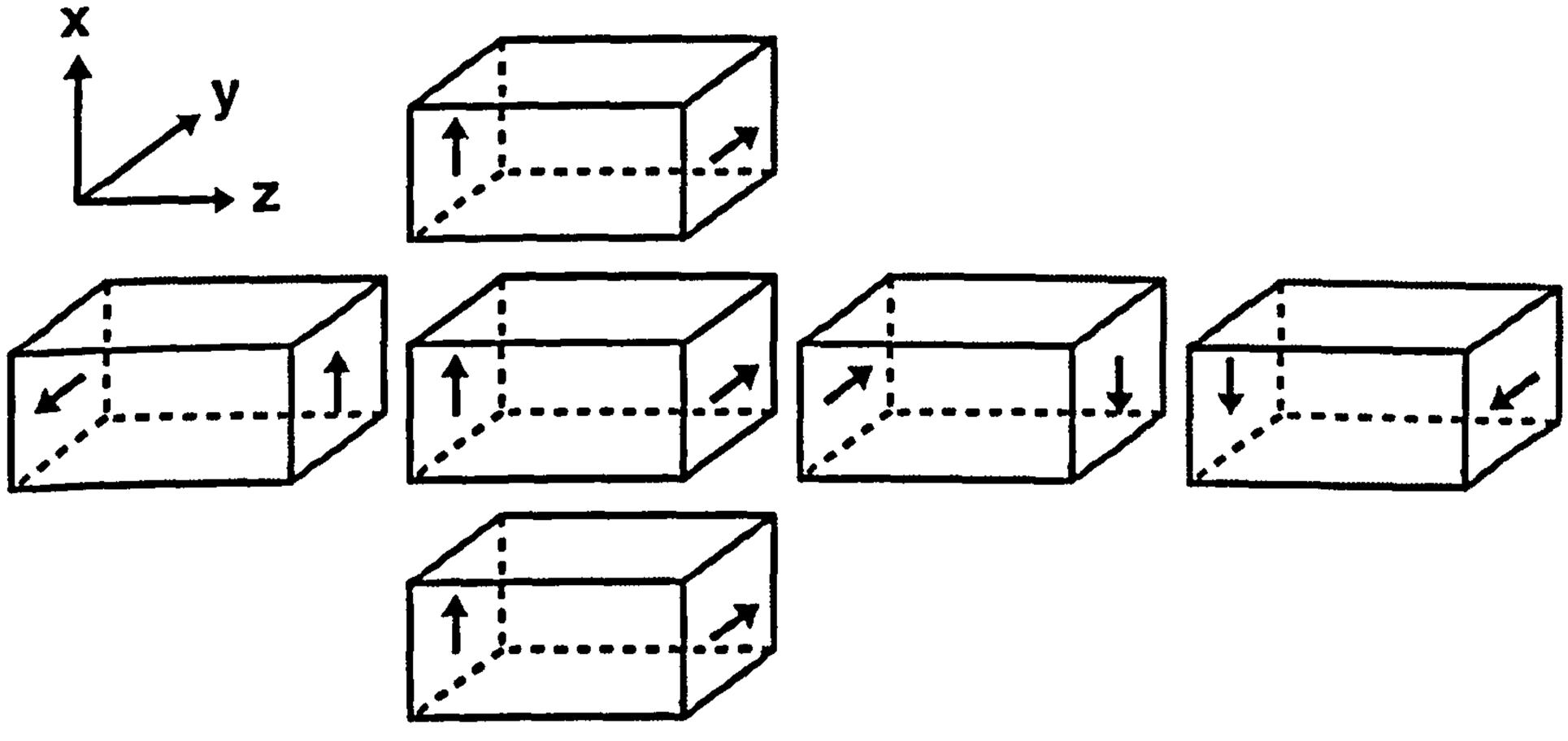

Insofaras we are imposing a specified pitch on the system, our simulations are analogous to the twist cell experiments referred to in section 5.2. The main determinant of the physical realism of our model is the ratio of the pitch to the smectic layer spacing, λ/d_0. This quantity varies widely among different experimental systems. In the DIC studies of fd [109], $\lambda/d_0 \approx 10$, but these are flexible, highly elongated particles with $L/D \approx 130$. In the original experiments on nP1M7, typically $\lambda/d_0 \approx 100$. In order to reach acceptable values of λ, we employ *twisted periodic boundary conditions* (TPBC), in which each periodic image of the cuboidal simulation cell along the z axis is rotated through $\pi/2$ with respect to the last, as illustrated in figure 5.5. This rotation is incorporated into the calculation of the forces between pairs of particles in different periodic images, and also when replacing particles which have left the basic cell in the $\pm z$ directions. In the latter case, the vectors describing the particle velocity and angular velocity are rotated, as well as the position and orientation, as illustrated in figure 5.6. The modified boundary conditions do not introduce any pathological effects - there are no stresses at the boundaries between

Figure 5.6: Replacement of a particle A leaving the simulation box in the $+z$ direction. It reenters as particle B, with its position, orientation, velocity and angular velocity rotated clockwise through one quarter about z. The helical twist in the director field, $\mathbf{n}$, is also shown.

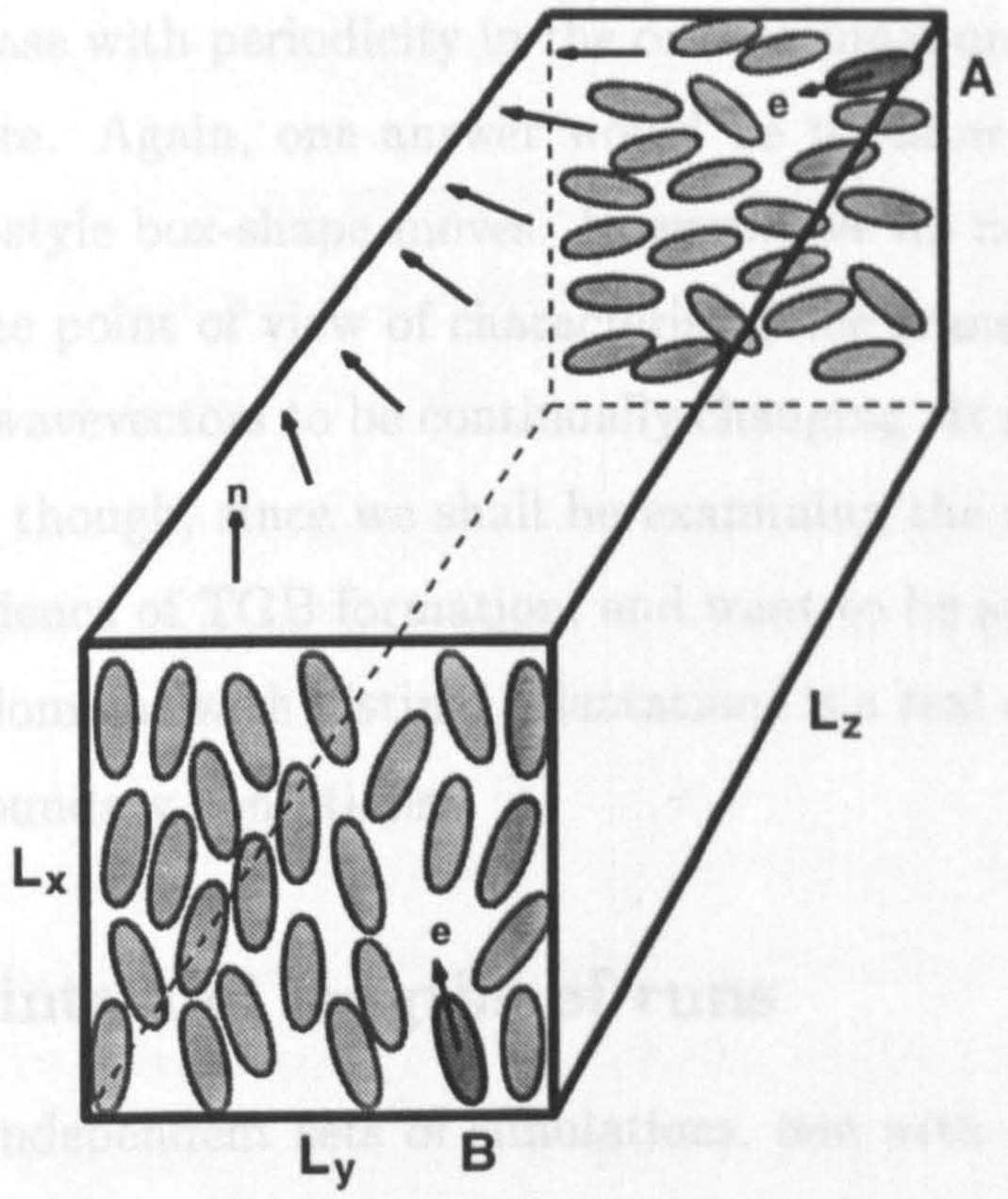

the images, total energy is still conserved, and translational momentum is conserved in the composite system consisting of four successive periodic images. In order for the images to match up, we must have $L_x = L_y = L_\perp$.

5.3.2 Choice of system size

As described above, the size of the system along the twist axis z determines the pitch. We set $L_z \approx 80\sigma_0$, so that the pitch is $320\sigma_0$ or approximately 80 smectic layer spacings, in reasonable correspondence with experimental values. The principal effect of finite $L_\perp$ is to restrict the number of accessible smectic layers to a discrete set. With $L_x = L_y = L_\perp$, the transverse wavevectors $\mathbf{k}_\perp$ consistent with the periodic

boundary conditions are

$$k_\perp = \frac{2\pi}{L_\perp}(mx + ny) \tag{5.6}$$

where m and n are integers. In the RL theory, $L_\perp$ is assumed infinite, and the set of accessible wavevectors is a continuum. This is also a good approximation for all the experiments mentioned, in which $L_\perp \gg d_0$. We have discussed the difficulties of equilibrating a phase with periodicity in the orientational order, and similar considerations apply here. Again, one answer would be to allow the box dimensions to fluctuate via MC-style box-shape moves. However, we do not do this, since it is inconvenient from the point of view of characterising the translational ordering for the set of accessible wavevectors to be continually changing. It is important to make $L_\perp$ reasonably large though, since we shall be examining the structure factor as a function of z for evidence of TGB formation, and want to be sure that any division we see into smectic domains with distinct orientations is a real effect and not simply an artefact of the boundary conditions.

5.3.3 Statepoints and lengths of runs

We performed two independent sets of simulations, one with $L_\perp = L_z/2$, and the other doubled in the x and y directions, i.e. with $L_\perp = L_z$. We studied two temperatures above the T_{NA} of the untwisted system, and three below it. A summary of the run parameters and lengths of these runs is shown in table 5.1. In the original set of runs with $N = 21000$, the simulations at $T^* = 0.8$ and $T^* = 0.9$ were both started from the final configuration at $T^* = 1.0$. With this exception, the runs were contiguous in order of decreasing temperature. During each run, the temperature was maintained constant by periodically rescaling translational and angular velocities. We monitored the evolution of the orientational and structure profiles, to be defined in the next section, and allowed the profiles to relax to a state from which there did not seem to be any further qualitative change. This does not necessarily imply that an equilibrium state has been reached: as we shall see, the time scale for the motion of boundaries between differently ordered regions is very long. Ideally, to check equilibration one would carry out several independent quenches from the

twisted nematic phase, but this is of course very expensive. A measure of confidence in the validity of our results can be obtained by comparing the independent simulations of the two different sized systems.

5.3.4 Preparation of starting configuration

The starting configurations for the runs were prepared using the following procedure:

- We started with 5250 particles partially filling a simple cubic lattice at a low density ($\rho = 0.02$) in a box with relative dimensions $1:1:4$, their orientations uniformly twisting along the z axis.

- The particles were each given random initial displacements of 0.1 lattice spacing, and a rotation about a random direction through an angle up to 0.3 radians.

- The system was gradually compressed to the required density. This was done using an MD run, with isotropic rescaling of coordinates at regular intervals. A constant kinetic temperature $T^* = 1.4$ was maintained through scaling of angular and translational velocities at each timestep. Throughout this procedure, the twisted orientational ordering was maintained using an extra field,

$$\mathcal{V}_{\text{align}} = \mathcal{V}_0 \sum_{i=1}^{N} \left\{ \frac{3}{2} \left[\mathbf{e}_i \cdot \mathbf{n}(r_{zi}) \right]^2 - \frac{1}{2} \right\} , \tag{5.7}$$

with

$$\mathbf{n}(z) = \cos\left(\frac{\pi z}{2L_z}\right) \hat{\mathbf{x}} + \sin\left(\frac{\pi z}{2L_z}\right) \hat{\mathbf{y}} . \tag{5.8}$$

The magnitude of the field was progressively reduced so as to maintain the *local* nematic order parameter within 10% of the known value for the untwisted system at this statepoint.

- The system was equilibrated for a further 50000 steps with no external field, to check for any instability towards an untwisted state.

Table 5.1: Simulation details.

Potential parameters	$\kappa = 4.4, \kappa' = 20, \mu = 1, \nu = 1, r_c = 5.5$	
Simulation timestep	$\Delta t = 0.0025$	
Density	$\rho^* = 0.16$	
	Original system	Extended system
System size	$N = 21000$	$N = 84000$
Box dimensions		
Transverse	$L_\perp = 40.34$	$L_\perp = 80.67$
Along twist axis	$L_\parallel = 80.67$	$L_\parallel = 80.67$
Run lengths (/1000 timesteps)		
$T^* = 1.4$	40	50
$T^* = 1.2$	—	40
$T^* = 1.0$	120	60
$T^* = 0.9$	230	65
$T^* = 0.8$	100	—

- $2 \times 2 \times 1$ periodic images were concatenated to produce a configuration of 21000 particles with box sides in the ratio 1 : 1 : 2, which was used as the starting configuration for the original set of runs.

- The final configuration from the original runs at $T^* = 1.4$ was doubled up again in the xy directions to produce the starting configuration for the 84000-particle runs.

5.4 Orientational and translational order

5.4.1 Definitions

We now define the functions we use to characterise the variation of the orientational and translational ordering along the twist direction, z. We assume that any domain boundaries that form are oriented perpendicular to z, in accordance with theory and experiment - our results will show that this is the case.

To characterise the orientational order, we use profiles of the order tensor. These are calculated in the usual way as second rank averages over the orientations of particles within each profile bin (a slab perpendicular to z):

$$Q_{\alpha\beta}(z_{\text{bin}}) = \frac{1}{N_{\text{bin}}} \sum_{i=1}^{N_{\text{bin}}} \left\{ \frac{3}{2} e_{i,\alpha} e_{i,\beta} - \frac{1}{2} \delta_{\alpha\beta} \right\} . \tag{5.9}$$

We then diagonalise $Q_{\alpha\beta}(z)$ to obtain a director profile $\mathbf{n}(z)$ and nematic order parameter $S(z)$. Generally, $\mathbf{n}$ is close to the xy plane. The orientation within this plane is defined by

$$\theta_{\mathbf{n}}(z) = \tan^{-1}\left(\frac{n_y}{n_x}\right) . \tag{5.10}$$

The definition of profiles for characterising translational ordering is slightly more subtle. In an untwisted smectic, the appropriate quantity to measure would be the structure factor,

$$S(\mathbf{k}) = \left\langle |\rho(\mathbf{k})|^2 \right\rangle \tag{5.11}$$

$$\rho(\mathbf{k}) = \frac{1}{\sqrt{N}} \sum_{i=1}^{N} \exp\left(i\mathbf{k} \cdot \mathbf{r}_i\right) . \tag{5.12}$$

In a well ordered smectic, this function has a large peak at the wavevector $\mathbf{k} = (2\pi/d_0)\mathbf{N}$, where $\mathbf{N}$ is the layer normal, and d_0 is the smectic layer spacing. We are interested in how $\mathbf{N}$, d_0, and the height of the peak vary along the twist direction. In the TGB A phase, we expect $\mathbf{N}$ in each domain to be colinear with the director, and so we confine our attention to transverse wavevectors $\mathbf{k}_\perp$. We calculate the structure factor within profile bins perpendicular to z:

$$S(\mathbf{k}_\perp; z_{\text{bin}}) = |\rho(\mathbf{k}_\perp; z_{\text{bin}})|^2 \tag{5.13}$$

$$\rho(\mathbf{k}_\perp; z_{\text{bin}}) = \frac{1}{\sqrt{N_{\text{bin}}}} \sum_{i=1}^{N_{\text{bin}}} \exp(i\mathbf{k}_\perp \cdot \mathbf{r}_i), \tag{5.14}$$

for a grid of transverse wavevectors compatible with the periodic boundary conditions,

$$\mathbf{k}_\perp = \frac{2\pi}{L_\perp}(n_x\hat{\mathbf{x}} + n_y\hat{\mathbf{y}}), \qquad n_x, n_y = 1 \cdots \left[\frac{L_\perp}{\sigma_0}\right], \tag{5.15}$$

where $[\cdots]$ indicates the integer part. The structure profiles $S(\mathbf{k}_\perp; z_{\text{bin}})$ are rather difficult to visualise. Within well ordered domains, the first order peaks lie on a ring of radius $k_0 = 2\pi/d_0$, and we are interested mainly in their angular position. In order to represent this dependence, we map our data from the k_x, k_y plane to polar coordinates k, θ, and integrate over a range about k_0, to get a layer orientation profile $S(\theta; z)$. The average of S over all profile bins

$$\langle S(\mathbf{k}_\perp)\rangle_{\text{bins}} = \frac{1}{n_{\text{bins}}} \sum_{\text{bin}=1}^{n_{\text{bins}}} S(\mathbf{k}_\perp; z_{\text{bin}}) \tag{5.16}$$

is also informative. This is *not* the same as the structure factor for the whole system, eqn (5.11), but gives qualitatively similar information on the prevalence of fluctuations towards smectic ordering at different wavevectors.

We use 40 bins for all our profiles, so that each bin is approximately $2\sigma_0$ in width and contains on average around 500 particles (2000 for the extended system runs). To obtain improved statistics, we averaged the profiles over several successive configurations.

Figure 5.7: Director profile at $T^* = 1.4$, from the $N = 21000$ run.

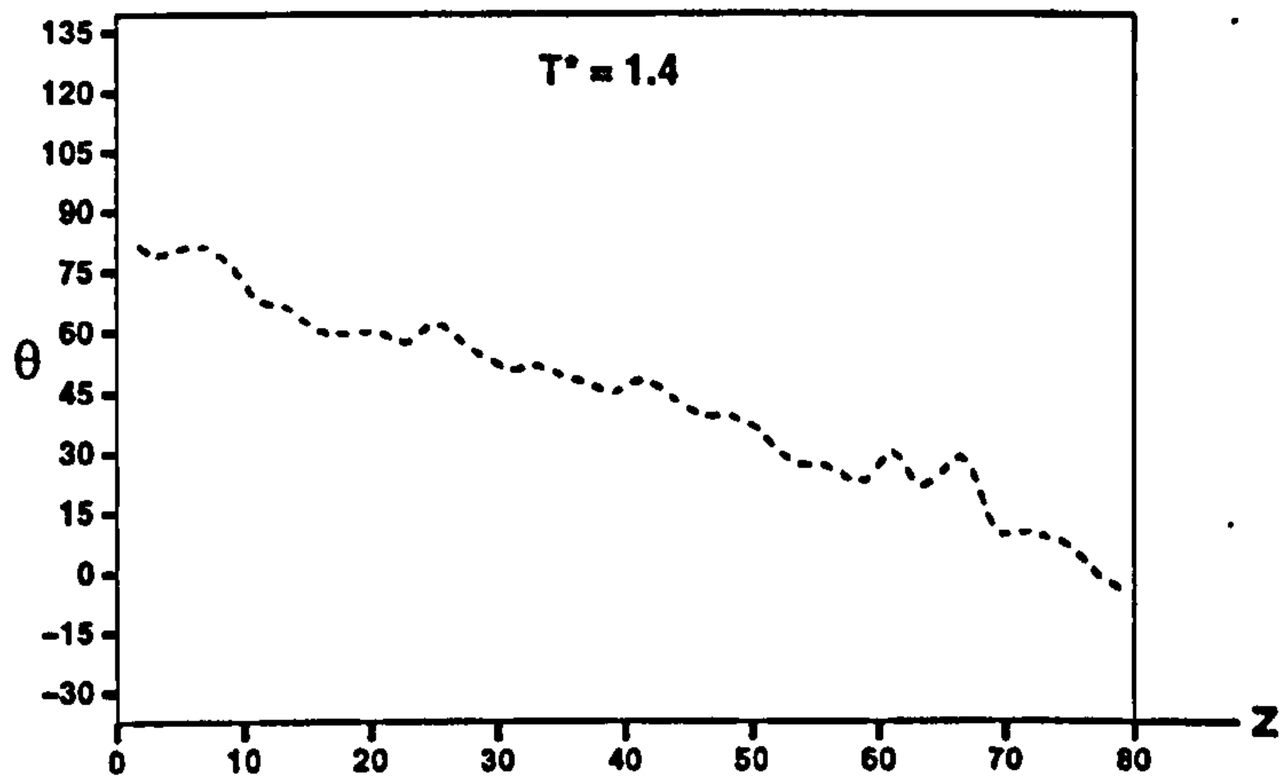

5.4.2 Results

Results at $T^* = 1.4$

This is well above the N→A transition of the untwisted system, and so we expect to observe twisted nematic order, but no long range smectic-like order. This is indeed the case. Profiles of the director orientation $\theta(z)$, figure 5.7, show that $\mathbf{n}(z)$ rotates uniformly from one end of the simulation box to the other. The degree of nematic ordering is quite low: the average order parameter $\langle S(z) \rangle_{\text{bins}}$ is approximately 0.40. There is no sign of any escape of the director towards a uniformly aligned state $\mathbf{n} = \mathbf{z}$; on average the absolute angle $\mathbf{n}(z)$ makes with the xy plane is $\approx 9°$ or less throughout the runs for both system sizes. The absence of well ordered smectic regions is revealed in the bin-averaged structure factor, figure 5.8 (i). At this statepoint, the function is radially symmetric, with a broad, low peak at around $|\mathbf{k}| = 1.7$. As the latter figure shows, at this statepoint, the radial dependence for the two system sizes is the same.

Results at $T^* = 1.2$

On cooling to this temperature, the qualitative behaviour of the director profile remains unaltered, although now the profile average of the nematic order parameter has increased to 0.59. The profile-averaged structure factor $\langle S(\mathbf{k}_\perp) \rangle_{\text{bins}}$, shown in

figure 5.8 (ii), retains its axial symmetry but the the peak is markedly narrower and higher than at $T^* = 1.4$. We also observe a slight shift of the peak towards lower k. Whilst the bin-averaged structure factor is independent of θ, at a given z the fluctuations towards translational ordering are predominantly along the local director. This correlation between local translational and orientational ordering can be seen in figure 5.10, in which the colour shading shows the orientational dependence of the structure profile $S(\theta; z)$, the dotted line is the transverse director profile $\theta(z)$.

Results at $T^* = 1.0$

At this temperature, just below T_{NA}, there is a definite change in the structure. The profile averaged structure factor, figure 5.9 (i), no longer has axial symmetry. Instead, we see the emergence of sharp peaks at specific wavevectors, whose heights fluctuate slowly during the course of the run. This suggests that the system is attempting to form smectic domains. In the $N = 21000$ system, we see some evidence of domain formation in the structure factor and director profiles, figure 5.10. The angular variation of $\mathbf{n}$ and $\mathbf{N}$ with z is no longer uniform, however there are no sharp domain interfaces. Examination of slices through the configurations shows that there are three fairly well ordered smectic regions of distinct layer orientations, interspersed with regions where the ordering is more nematic-like, which take up the twist. In each of these domains, the layer spacing $d_0 \approx 4.3\sigma_0$.

In the $N = 84000$ system, the height of the structure peaks grows more slowly, but after around 40000 steps the results resemble those of the smaller system.

Results at $T^* = 0.9$ and $T^* = 0.8$

At $T^* = 0.9$, the peaks in the bin-averaged structure factor which we observed at $T^* = 1.0$ grow in height, as shown in figure 5.9 (ii). Much more interestingly, though, the director and structure profiles for the $N = 21000$ runs, figure 5.10, reveal very clear domain boundaries. At the particular timestep shown here, there are four domains, with boundaries at $z = 8, 25, 33$ and 60; at other parts of the

run the smaller of these is not visible. The results from the independent quench from $T^* = 1.0$ to $T^* = 0.8$ (not shown) are rather similar, except that the maximum values of $S(k_x, k_y)$ in the center of the domains are somewhat higher. The profiles for the $N = 84000$ system, figure 5.11, also show some non-uniformity in the director, although the boundaries are not so clearly delineated. These results are consistent with a TGB-like structure.

Figure 5.8: The bin averaged structure factor $S = \langle S(\mathbf{k}_\perp) \rangle_{\text{bins}}$, at temperatures $T^* = 1.4$ and $T^* = 1.2$. In (i) we show the run average of S for the $N = 21000$ system, and also its radial dependence for both $N = 21000$ (circles) and $N = 84000$ (triangles). The results for the $N = 84000$ system at $T^* = 1.2$ are shown in (ii).

(i) $T^* = 1.4$

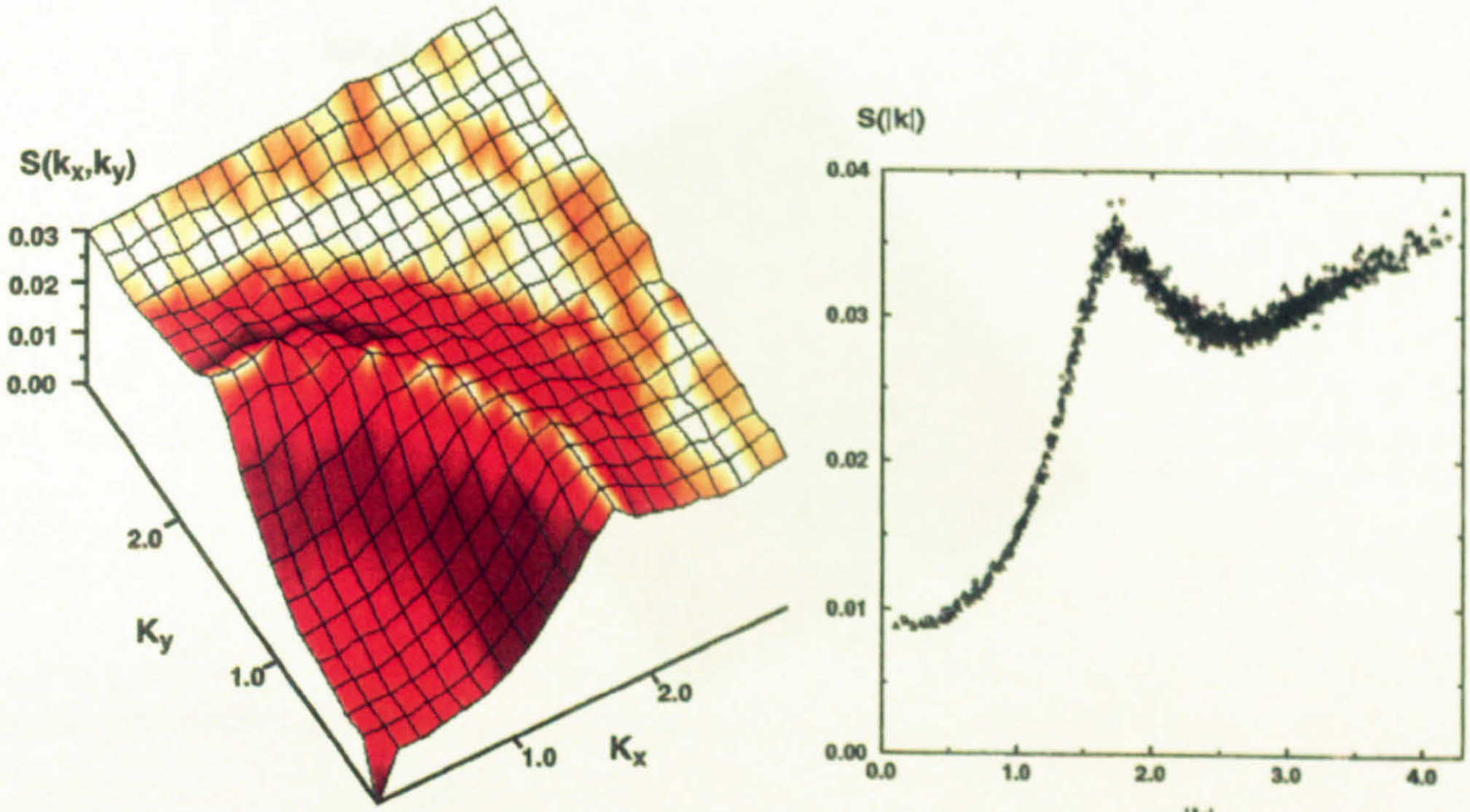

(ii) $T^* = 1.2$

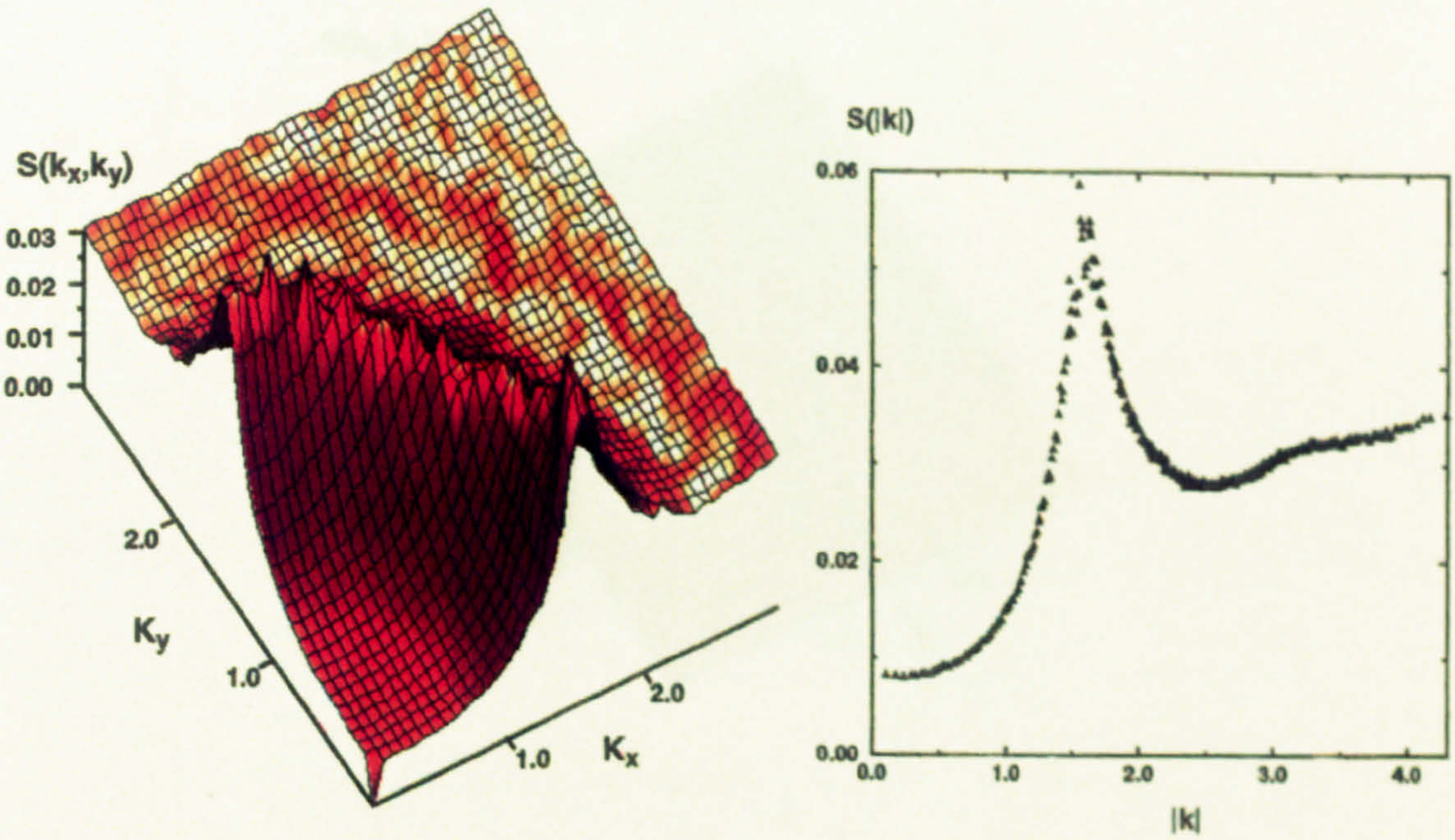

Figure 5.9: The bin averaged structure factor $S = \langle S(\mathbf{k}_\perp) \rangle_{\text{bins}}$, at temperatures $T^* = 1.0$ and $T^* = 0.9$, for the $N = 21000$ system.

(i) $T^* = 1.0$

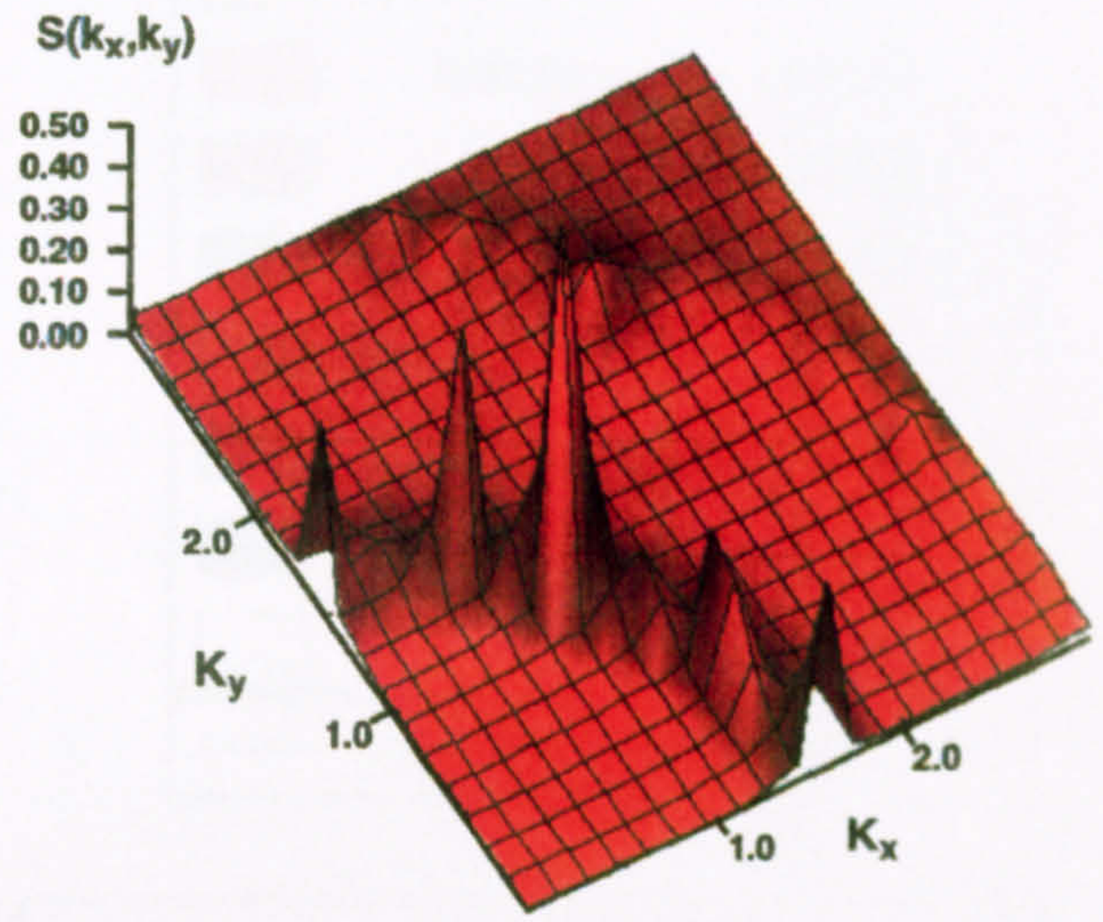

(ii) $T^* = 0.9$

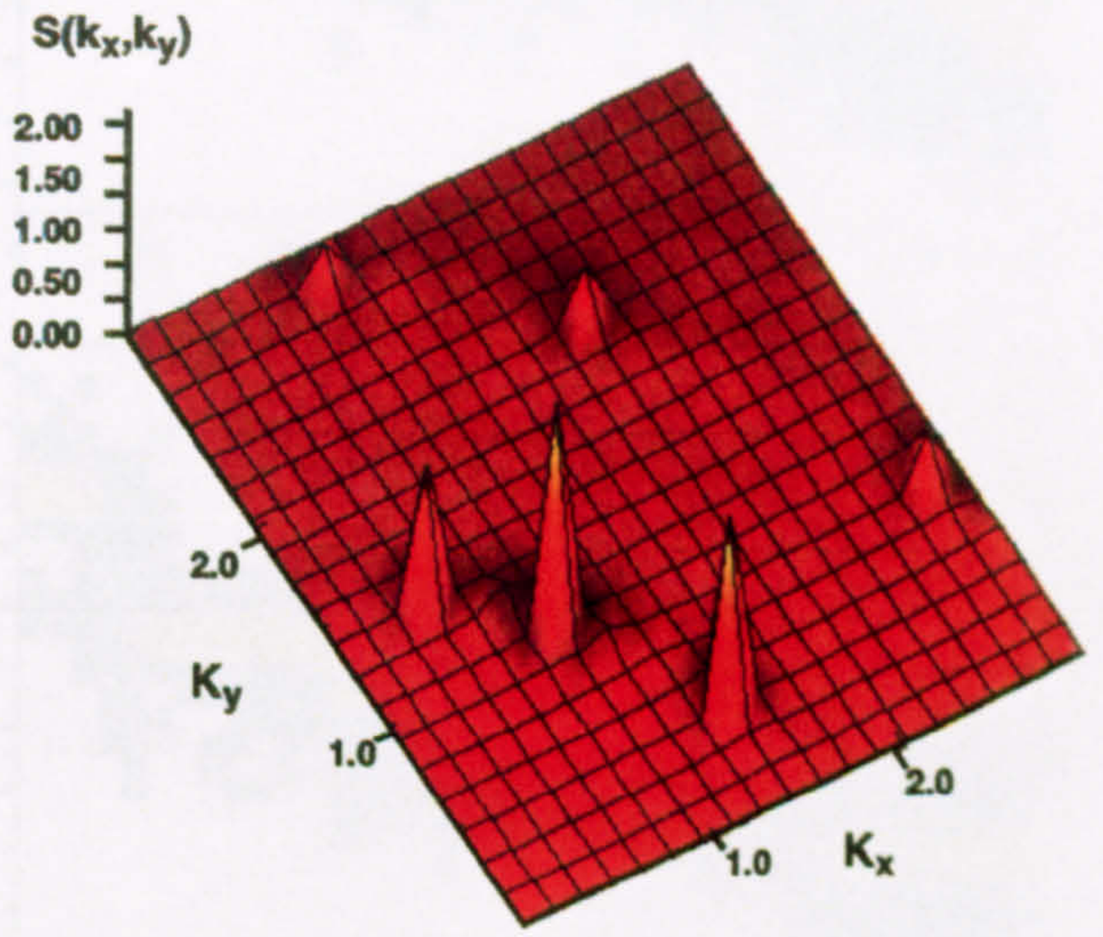

Figure 5.10: Profiles showing the orientational dependence of the structure factor, $S(\theta; z)$ and the director profile, $\mathbf{n}(z)$. These results are for the simulations with $N = 21000$. In each case, the profiles are averaged over 1000 timesteps, near the end of the run concerned.

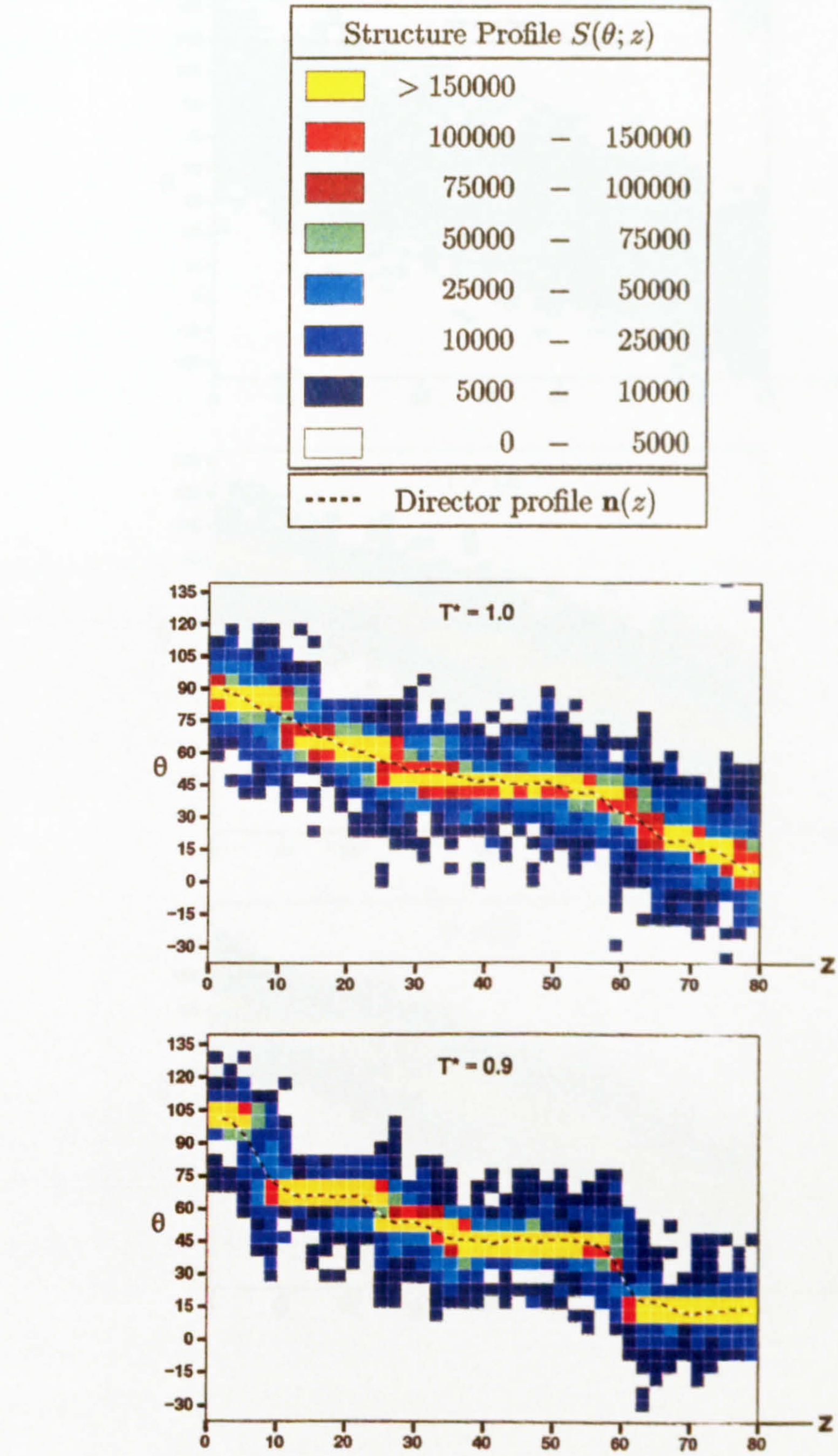

Figure 5.11: Profiles from the $N = 84000$ simulations. For key, see figure 5.10.

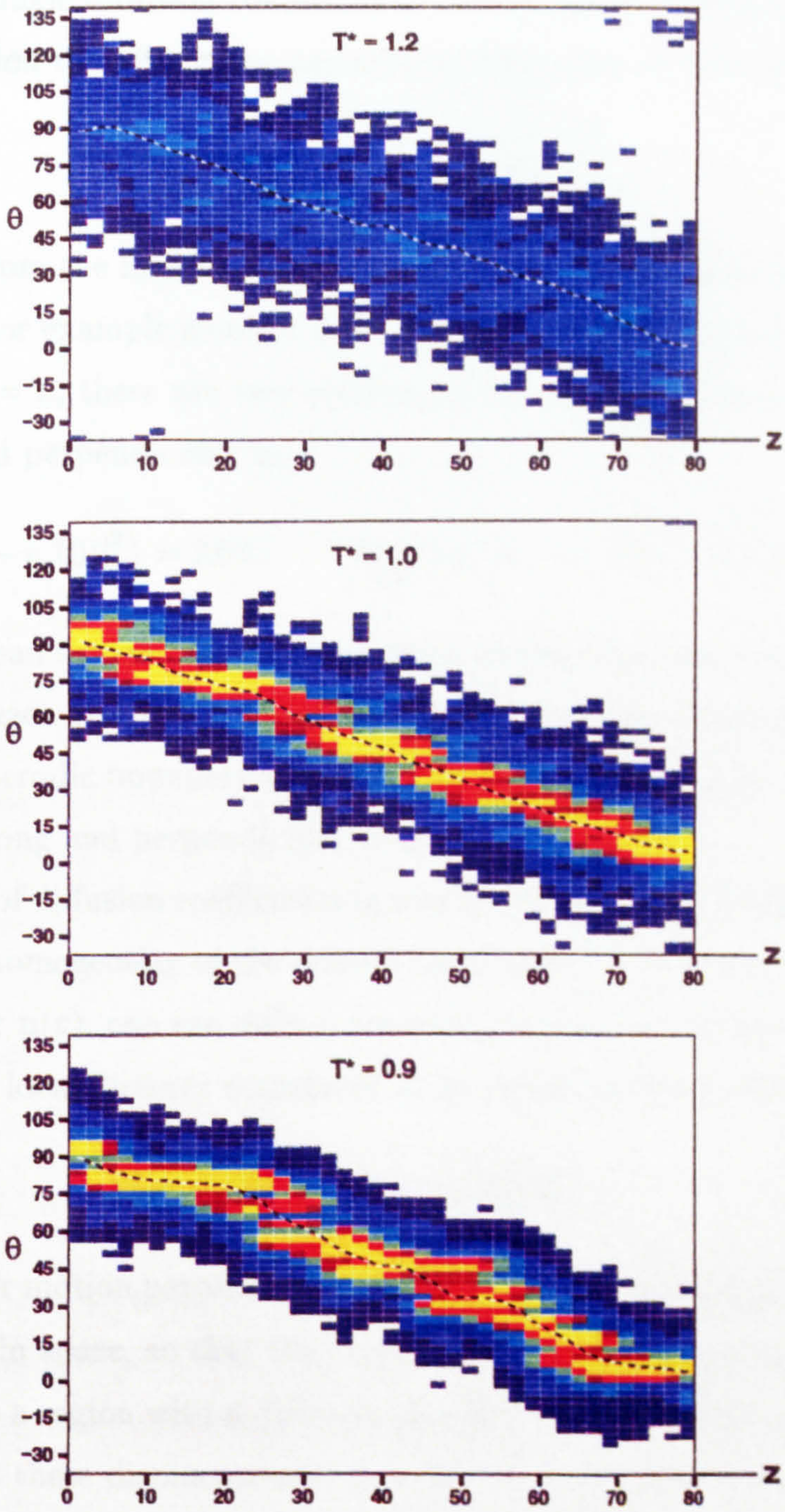

5.5 Diffusion

Our principal motivation for studying single-particle dynamics is to verify that the ordered domains we observe are smectic-like, and not crystalline. The diffusion rate is a useful indicator of whether or not the system has solidified. In an isotropic phase, there is a single diffusion coefficient D, which can be defined either through the Einstein relation describing the asymptotic behaviour of the mean square displacement,

$$\lim_{t\to\infty} \left\langle |\mathbf{r}(t) - \mathbf{r}(0)|^2 \right\rangle = 6Dt\,. \tag{5.17}$$

or, equivalently, from the infinite time integral of the velocity autocorrelation function. In a phase, for example smectic A or nematic, with uniaxial symmetry about some direction $\mathbf{n} = \mathbf{z}$, there are two coefficients $D_\perp$ and $D_\parallel$, which correspond to diffusion along and perpendicular to $\mathbf{z}$:

$$\lim_{t\to\infty} \left\langle |r_z(t) - r_z(0)|^2 \right\rangle = 2Dt\,, \qquad \lim_{t\to\infty} \left\langle |\mathbf{r}_\perp(t) - \mathbf{r}_\perp(0)|^2 \right\rangle = 4Dt\,. \tag{5.18}$$

Calculating the mean square displacements from simulation data is straightforward: the trajectory of each particle is unfolded from some chosen time origin, undoing the effects of the perodic boundary reboxings, and the displacement of each particle is then resolved along and perpendicular to $\mathbf{n}$.

The definition of diffusion coefficients in a twisted nematic or TGB phase is complicated by the inhomogeneity of the orientational order. In a system with spatially dependent director $\mathbf{n}(\mathbf{r})$, one can define, for each particle, the square displacements resolved along the local director evalulated at its initial position $\mathbf{r}(0)$,

$$r_\parallel^2 = \left\langle |[\mathbf{r}(t) - \mathbf{r}(0)] \cdot \mathbf{n}\,[\mathbf{r}(0)]|^2 \right\rangle\,, \tag{5.19}$$

and similarly $r_\perp^2$ for motion perpendicular to the director. In principle, if $\mathbf{n}(\mathbf{r})$ varies sufficiently slowly in space, so that the linear diffusive regime is reached before the particle strays into a region with a different director, then values for $D_\perp$ and $D_\parallel$ can be calculated from these displacements. In order to demonstrate that the particles are diffusing, though, it is sufficient to calculate a profile of $|\mathbf{r}(t) - \mathbf{r}(0)|^2$, i.e. the average total mean square displacement of particles which were in each of the 40

Figure 5.12: Profiles of total mean squared displacement, at the temperature $T^* = 0.9$, from the $N = 84000$ run. Distances are in units of σ_0, and t in timesteps, $\Delta t = 0.0025$.

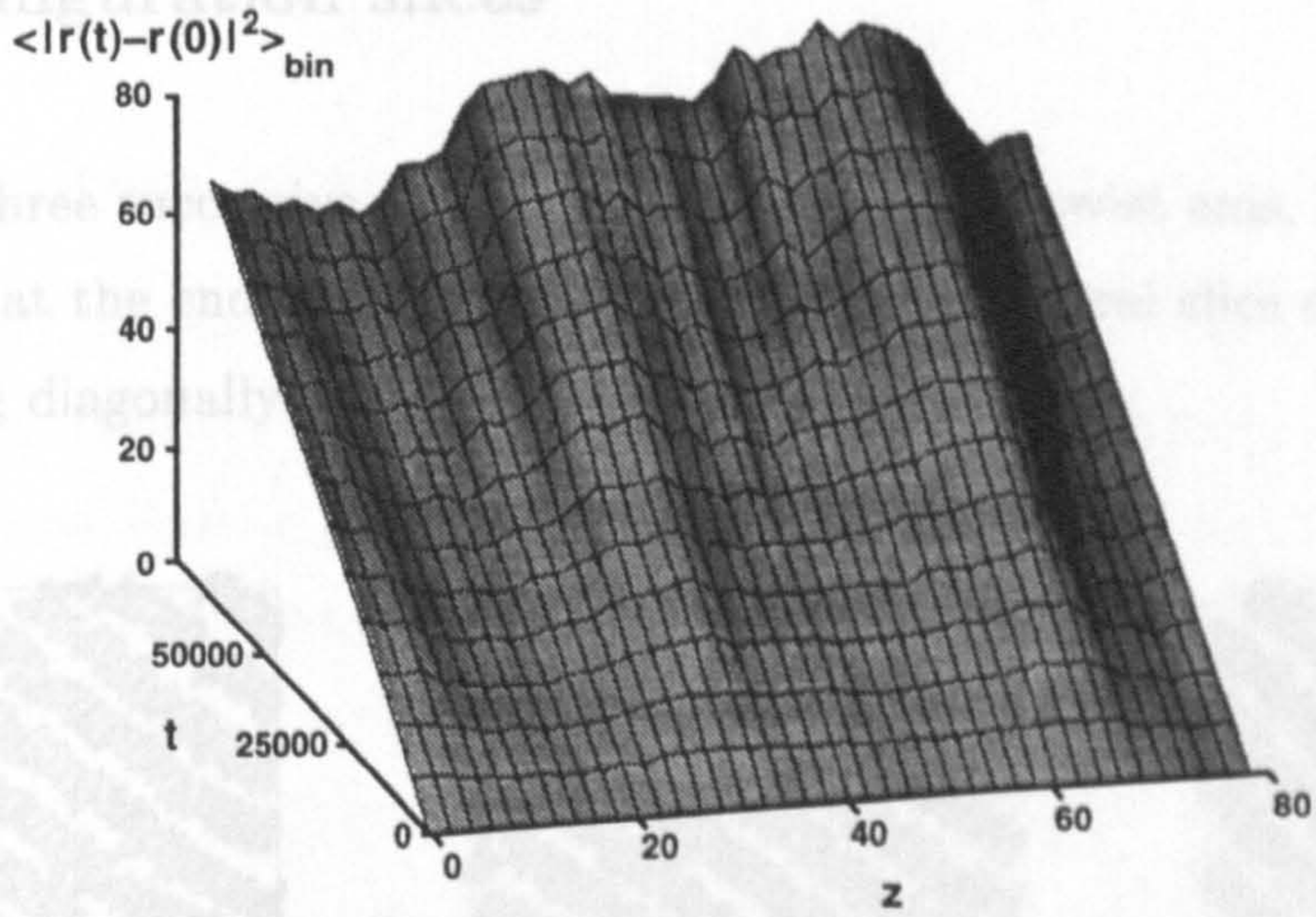

slabs at time $t = 0$. The results for the $N = 84000$ system at $T^* = 0.9$ are shown in figure 5.12. The root mean square displacement over the entire run of 65000 timesteps ($t_{\max} = 160$ in reduced units) is greater than $8\sigma_0$ in all of the profile bins, and the average over the bins is $8.8\sigma_0$. Since this is more than twice our estimated value of d_0, we conclude that although the diffusion is quite slow, the system is certainly not a solid.

5.6 Structure of interfacial regions

Our orientational and structure profiles are consistent with the TGB structure, but they do not shed much light on the structure of the domain interfaces. Since these interfaces occupy only a small fraction of the sample volume, it is difficult to probe their structure in X-ray scattering experiments, and to date no direct experimental evidence for the presence of *the twist defects* predicted in the RL theory exists.

Computer simulation allows us to investigate the domain boundaries much more closely. In this section we describe the techniques we use to search for defects, and compare the nature and distribution of defects seen in our simulations with the RL theory.

5.6.1 Configuration slices

Figure 5.13: Three successive slices perpendicular to the twist axis, from one of the configurations at the end of the run at $T^* = 0.8$. The central slice contains a twist defect, running diagonally through the box.

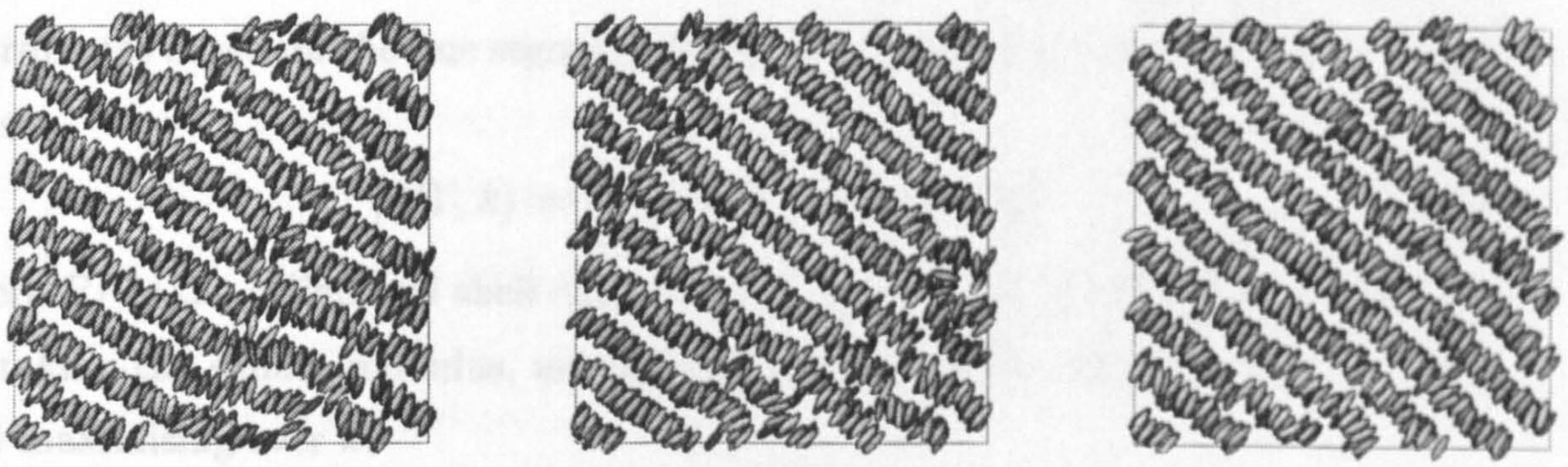

(i) $-14.52 < z < -11.29$ (ii) $-11.29 < z < -8.07$ (iii) $-8.07 < z < -4.84$

Our first method for finding defects was inspecting images of slices through the configurations. Twist defects lying in the plane of the slices can be seen directly. In figure 5.13 for example, we show three successive slices perpendicular to the z axis, taken from the final configuration of the runs at $T^* = 0.8$. Slices (i) and (iii) both show more or less uninterrupted smectic ordering, in two different orientations, and a twist defect can be clearly seen running diagonally through the central slice (ii). The orientations of the smectic layers above and below the layer are approximately 117° and 126°, so this defect creates a grain boundary with $\Delta\theta \approx 9°$.

Identifying defects in this way is tedious, and is particularly difficult if the defects do not lie in the plane of the slices. To overcome this problem, and allow a

more systematic investigation of the defect distribution, we developed a method for searching for them automatically. Briefly, this works as follows: we define a *goal function* which gives a numerical measure of how well the ordering in the neighbourhood of a given line segment conforms to the topology of twist defects shown in figure 5.3, and then seek to maximise this goal function over the space of possible segments.

5.6.2 Definition of goal function

In the RL theory, the defects are infinite straight lines in the xy plane, but we do not assume this. Rather, we represent them as chains of connected line segments. The first step is to define a goal function for a single segment, $G(\Gamma)$. In cylindrical coordinates based on the line segment, (r, ϕ, ζ), with the ends of $G(\Gamma)$ at $\zeta = \pm l_\Gamma/2$, we set

$$\rho^d(\Gamma, k) = \int_{\mathcal{R}_\Gamma} \mathrm{d}\mathbf{r}\rho(\mathbf{r}) \exp[i(k\zeta - \phi)] \,, \tag{5.20}$$

where $\mathcal{R}_\Gamma$ is the cylindrical shell $r_{\min} < r < r_{\max}$, $|\zeta| < \pm l_\Gamma/2$. We then define $G(\Gamma)$ by taking the square modulus, normalising by the number of particles within $\mathcal{R}_\Gamma$, and maximising over k:

$$S^d(\Gamma, k) = \frac{|\rho^d(\Gamma, k)|^2}{\int_{\mathcal{R}_\Gamma} \mathrm{d}\mathbf{r}\rho(\mathbf{r})} \tag{5.21}$$

$$G(\Gamma) = \max S^d(\Gamma, k) \,. \tag{5.22}$$

It is intuitively reasonable that for a segment of fixed length, $G(\Gamma)$ is greatest when Γ lies along a twist defect. In appendix A we confirm this by considering the behaviour of Γ for various idealised density distributions, and for portions of actual configurations in which defects have been found by eye.

The single particle density which appears in eqn (5.20) is obtained by averaging over a number of successive configurations, for improved statistics. The rate of single particle diffusion gives a conservative estimate of the length of time over which we can perform this averaging without smearing out the density modulation. In practice the number of configurations is limited by the computational expense of calculating G, although this was reduced considerably by using a linked cell search to extract molecules lying within $\mathcal{R}_\Gamma$.

The arrangement of defects in the system is described as a set of chains of segments, or *conformation*, Ω. The *global goal function* $\mathcal{G}(\Omega)$ consists mainly of a sum of single-segment terms,

$$\mathcal{G}_{\text{ssgf}} = \sum_{i=1}^{n_{\text{segs}}} G(\Gamma_i) \,. \tag{5.23}$$

In order to obtain a well-defined optimisation problem the following points must be considered:

- Although the lengths of segments l_i need not be fixed, the evaluation of $G(\Gamma)$ is clearly meaningless if the segment is too short (comparable with the smectic layer spacing). We insist that every segment be longer than some minimum length, l_{min}.

- $G(\Gamma)$ is always non-negative, so we must include an additional term in the goal function to prevent the total length of the chains from growing without bound. Whilst we do not know *a priori* the total length of defect, we estimate that it will be of the order $\pi L_\perp^2/2d_0$. This is the total length predicted on the basis of a regular network of twist defects producing a $\pi/2$ twist in the box. We therefore place an upper bound, $L_{\text{max}} \approx \pi L_\perp^2/2d_0$, on the total segment length.

- If the chains do not interact in any way, then several may choose to lie along the same defect. To inhibit this, we impose a limit on how close the line segments may approach each other. We imagine a hard spherocylinder $\mathcal{S}_\Gamma$ of radius r_{max} and length l_Γ, coaxial with each Γ. Pairs of spherocylinders $(\mathcal{S}_i, \mathcal{S}_j)$ are permitted to overlap only if the corresponding (Γ_i, Γ_j) are neighbouring segments on the same chain.

- Since our aim is to describe the defects in terms of *connected* line segments, we need another term in the global goal function which will favour longer chains over a large number of isolated segments. This is accomplished by adding a term $-\lambda n_{\text{chains}}$. In the limit $\lambda \to \infty$, this will result in one long chain. In the limit $\lambda \to 0$, the conformation will consist of isolated segments.

A precise definition of our problem is now possible: we must maximise

$$\mathcal{G}(\Omega) = \mathcal{G}_{\text{ssgf}} - \lambda n_{\text{chains}} \,, \tag{5.24}$$

subject to the spherocylinder overlap constraint, along with the conditions

$$\sum_{i=1}^{n_{\text{segs}}} l_{\Gamma_i} \leq L_{\max} \tag{25a}$$

$$l_{\Gamma_i} < l_{\min}, \text{ for all } i \,. \tag{25b}$$

5.6.3 Maximisation of goal function

Figure 5.14: These diagrams show variants of the annealing moves for maximising the goal function for detecting defects. A *displacement* consists of moving a node joining two segments; this move can be applied to (i) an interior node, or (ii) an endpoint. The second kind of move is a *segment transfer*. The transfer can be from one chain to another (iii), or to the opposite end of the same chain, if it contains two or more segments (iv). Transfer from a one-segment chain results in its destruction (v). In a *disconnection* move (vi) a chain is broken at one of its interior nodes. None of the segment conformations are changed, but there is a decrease in the goal function since n_{chains} increases by one.

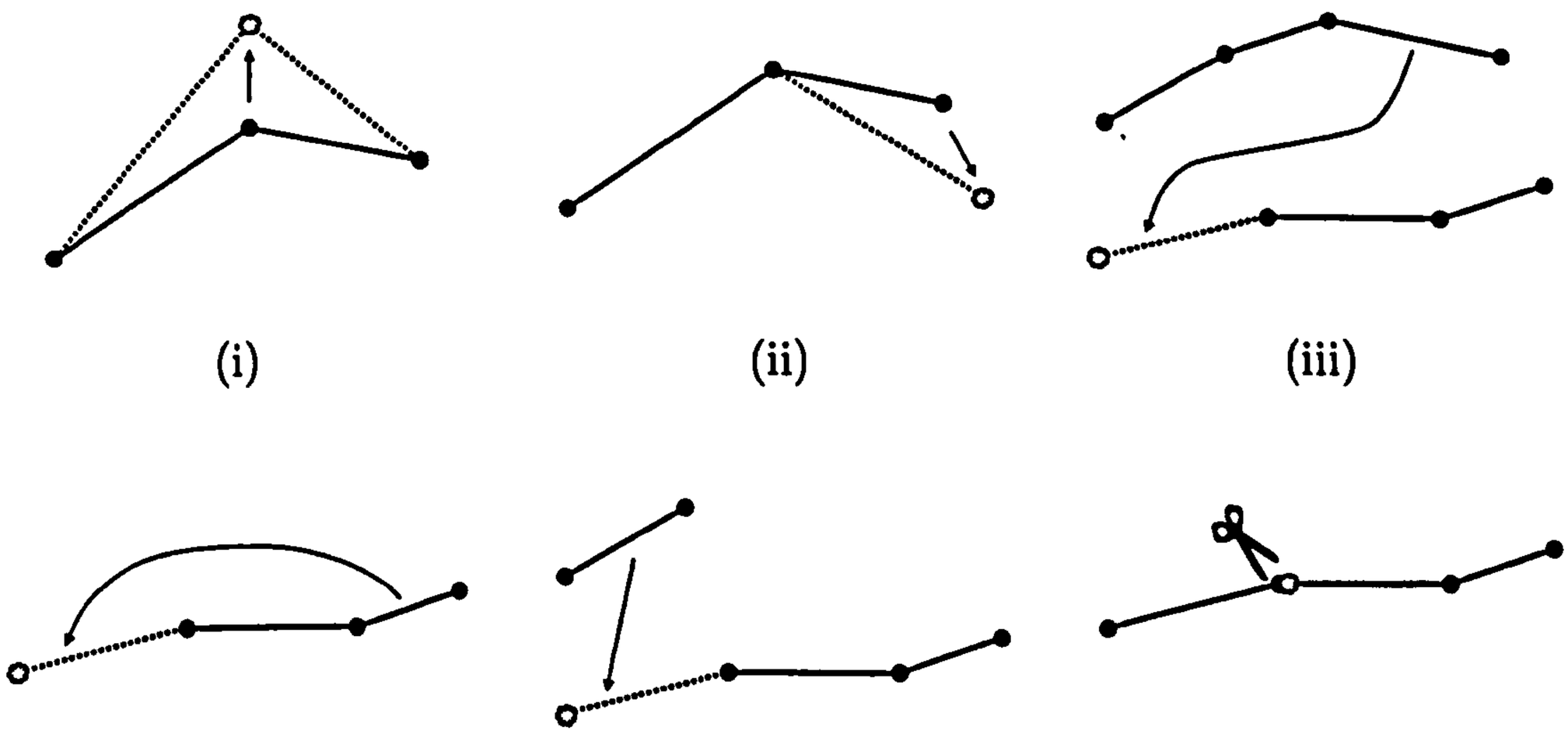

We use the *simulated annealing* method [111] to maximise $\mathcal{G}(\Omega)$ subject to the constraints, since Ω has both discrete and continuous degrees of freedom: the partitioning of segments among chains, and the positions of the nodes at which segments are connected. We choose a set of *annealing moves* $\mathcal{M}_1, \mathcal{M}_2 \cdots \mathcal{M}_n$, each of which modifies the conformation in some way. We begin with a random conformation Ω_0, and set the *annealing temperature* τ to some $\tau_0 > 0$. At each step s of the annealing process, we select one of the moves, $\mathcal{M}_i$ at random, and apply it to the current conformation, generating a *trial* conformation $\Omega_s^{\text{trial}} = \mathcal{M}_i\Omega_s$. We then calculate the change in the goal function,

$$\Delta\mathcal{G} = \mathcal{G}(\Omega_s^{\text{trial}}) - \mathcal{G}(\Omega_s)\,. \tag{26}$$

If $\Delta\mathcal{G} > 0$ then we accept the move, i.e. we set $\Omega_{s+1} = \Omega_s^{\text{trial}}$. If the trial conformation has a lower goal function, then we accept the move with a probability $\exp(\Delta\mathcal{G}/\tau)$, and retain the unmodified conformation, $\Omega_{s+1} = \Omega_s$. Over the course of the run, the 'temperature' τ is gradually reduced to zero, so that eventually only moves which increase the goal function are accepted. This procedure is guaranteed to find the global maximum provided that τ_0 is large enough, the moves are sufficiently general to allow exploration of the entire space of conformations consistent with the constraints, and τ is reduced sufficiently slowly.

The annealing moves we use, shown in figure 5.14, involve displacement of a node joining two segments, transferral of a segment from the end of one chain to another, and breaking a chain at a node. These three types were attempted with relative frequencies 10 : 1 : 1 respectively. The size of displacement moves was reduced adaptively as the temperature was lowered to maintain a constant acceptance rate of around 30%. The other relevant parameters in the simulated annealing process were as follows:

Initial conformation	Randomly placed unisegment chains
Number of attempted moves	$n_{\text{steps}} = 10^6$
Number of segments	22
Maximum total defect length	$600\sigma_0$
Bounds on segment length l_{min},l_{max}	$10\sigma_0 < l_\Gamma < \frac{L_\perp}{2}$
Chain weight λ	40
Initial annealing temperature	$\tau_0 = 40$
Annealing schedule	$\tau_s = \tau_0(1 - s/n_{\text{steps}})$
Cutoff radii for $\mathcal{R}_\Gamma$	$r_{\text{min}} = 2\sigma_0$, $r_{\text{max}} = 5.5\sigma_0$

5.6.4 Results

The method outlined above successfully locates the defect which we found by eye, and many others. Moreover, independent annealing runs on a given density distribution starting from two different random conformations of unisegment chains give fairly repeatable results: the final conformations differ only in the positions of a few segments, and most of these clearly do not correspond to well defined defects.

The simulated annealing results for the final configurations at $T^* = 0.8$ from the $N = 21000$ simulations are shown in figure 5.15. There is qualitative agreement with the TGB defect structure in the following repects:

- In the majority of cases, the distribution of molecules around each segment corresponds with the twist defect structure.

- All of the segments found all lie approximately in the xy plane, and their orientations follow the position of the peaks in the structure profile.

- The three defects at the bottom of the picture correspond to the domain boundary at $z \approx 10$, seen in figure 5.10, and are oriented along y. A grain boundary consisting of defects with separation $l_d = L_\perp/3$ and $d_0 = 4.3\sigma_0$ would give a $\Delta\theta \approx 19°$, whereas the structure and director profiles show that the actual grain boundary angle is nearer 28°. This discrepancy is presumably due to other less well defined defects, or nematic regions, involved in this boundary that are not seen by our program.

- Considering only segments whose ordering is convincingly helical, the total length of defect segments found in this particular configuration is $295\sigma_0$, compared to $\pi L_\perp^2/2d_0 = 570\sigma_0$, i.e. a fair fraction of the total amount of twist in the simulation cell is explained by the presence of well defined twist defects found by our annealing program.

We also analysed the final configurations from the $N = 84000$ runs at $T = 0.9$, and here too we found many segments which correspond to well defined defects. The distribution of these segments, and the molecular arrangement in the neighbourhood of a typical example, are shown in figure 5.16. The results are qualitatively similar to those described above. Interestingly, in this case however the distribution of defects along the z axis is more uniform. This is consistent with the structure profiles in figure 5.11, where we see that there is a large degree of local smectic ordering and yet it is difficult to identify grain boundaries at specific values of z.

Figure 5.15: The final chain conformation Ω, obtained by running the simulated annealing program on the last five configurations of the $T^* = 0.8$ run, in the $N = 21000$ system. For each segment, we show the goal function G_Γ, and the distribution of molecules within $\mathcal{R}_\Gamma$. This is plotted as a function of ϕ, running from 0 to 2π horizontally, and ζ, running from $-l_\Gamma/2$ to $+l_\Gamma/2$ vertically. For clarity, twisted periodic boundary conditions have been applied to some segments to return them to the basic simulation cell: solid lines indicate segments which are actually joined, dotted lines segments which are almost joined. Free ends of chains are shown with lines terminating in a point.

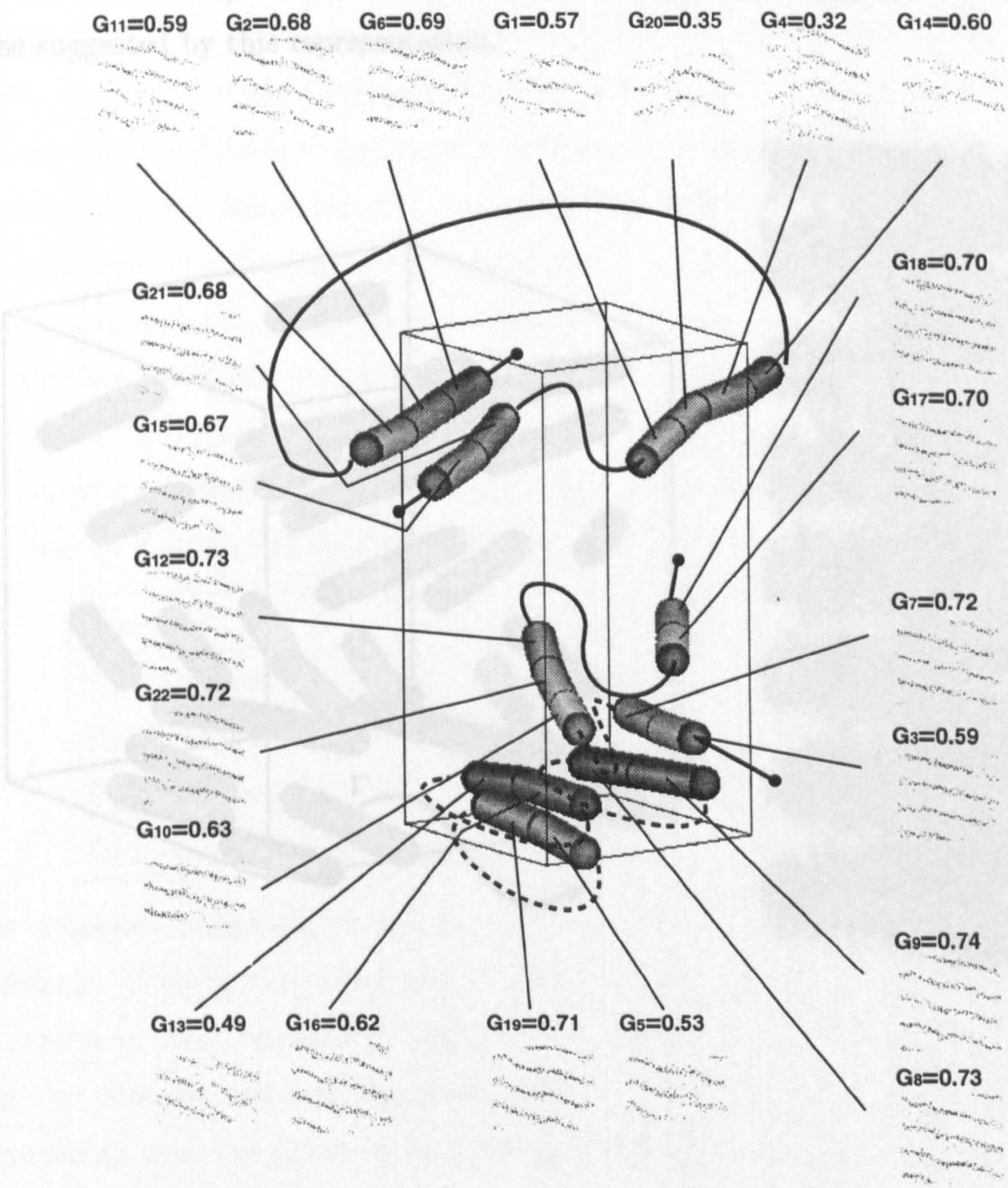

Figure 5.16: The distribution of segments from the simulated annealing analysis of configurations from the end of the $T^* = 0.9$, $N = 84000$ run. Only segments which clearly correspond to defects are shown. We also illustrate the arrangement of molecules within a cylinder of radius $7\sigma_0$ coaxial with a typical segment. To show their orientations and positions clearly, we have depicted the molecules as depth-shaded ellipsoids; it should be noted however that the potential minima for end-end and side-by-side orientations occur at separations approximately double those suggested by this representation.

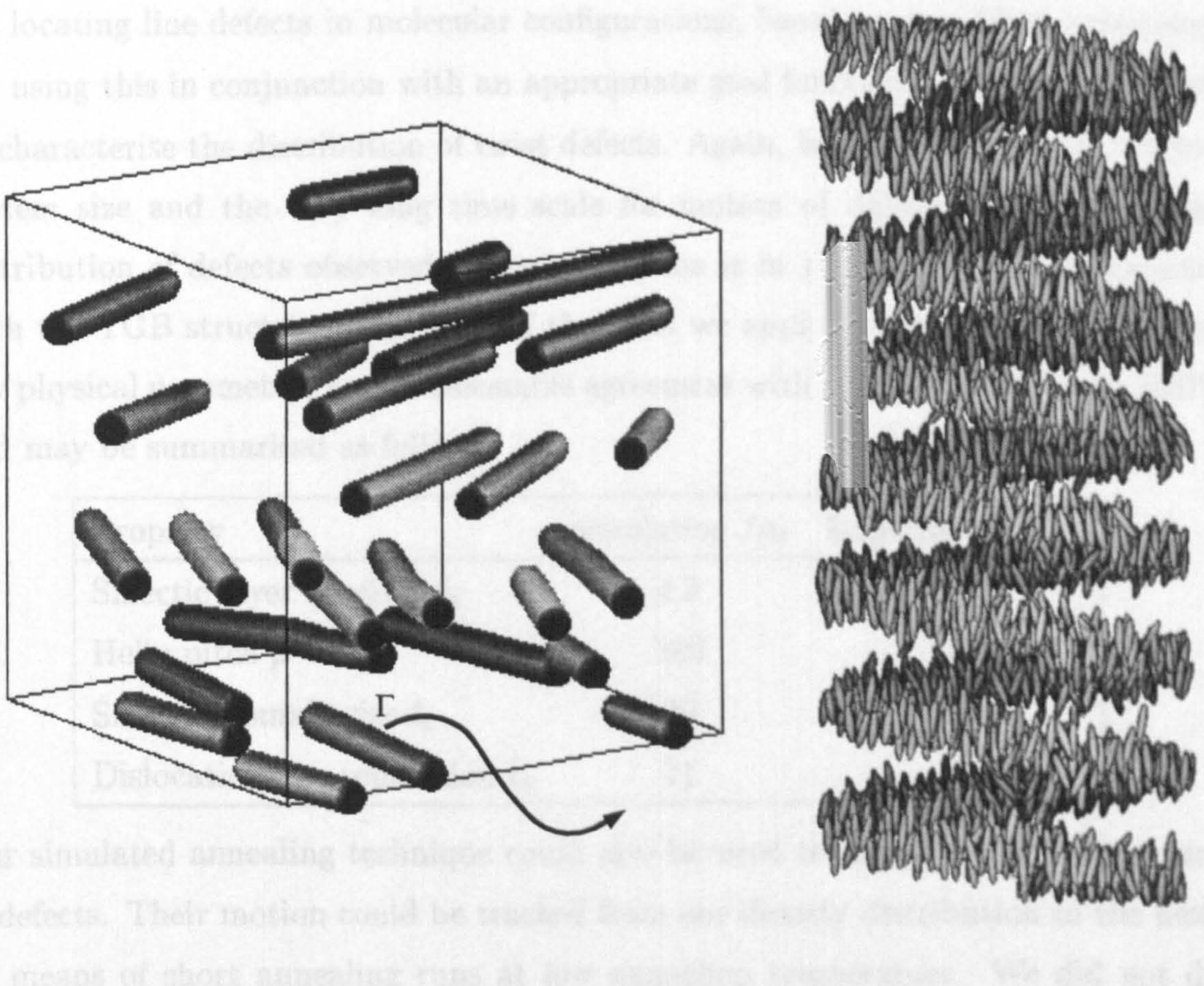

5.7 Conclusions

We have performed extensive large scale molecular dynamics simulations of a system of particles interacting via a particular parametrisation the Gay-Berne potential. In order to represent the effects of molecular chirality (or an externally applied torque), twisted periodic boundary conditions were used. Starting from a twisted nematic, we investigated the structure that forms on lowering the temperature below the nematic - smectic A transition of the untwisted system. We calculated profiles to characterise the variation of orientational and translational ordering along the twist axis. These results indicate the development of several smectic-like domains, which at lower temperatures are separated by well defined grain boundaries. To this extent, the structure we observe corresponds with that of the twist grain boundary (TGB) phase. In order to study the interfacial regions, we have developed a novel technique for locating line defects in molecular configurations, based on simulated annealing. By using this in conjunction with an appropriate goal function, we have attempted to characterise the distribution of twist defects. Again, bearing in mind the limited system size and the very long time scale for motion of defects, the nature and distribution of defects observed in our simulation is in good qualitative agreement with the TGB structure. The pitch of the twist we apply to our system, and other key physical parameters are in reasonable agreement with experimental results [107], and may be summarised as follows:

Property	Simulation $/\sigma_0$	Experiment /nm
Smectic layer spacing d_0	4.3	4.1
Helix pitch p	320	500
Smectic domain size l_s	20	24
Dislocation line separation l_d	11	15

Our simulated annealing technique could also be used to investigate the *dynamics* of defects. Their motion could be tracked from one density distribution to the next by means of short annealing runs at low annealing temperature. We did not do this; our director and structure profiles at $T^* = 0.9$ and $T^* = 0.8$ do not change appreciably once the domains have formed, and this suggests that the network of

defects is fairly static. Locating defects in a number of independent configurations would also give us good statistics for the single particle density distribution in the neighbourhood of a defect, which would allow us to calculate a radial profile $|\psi(r)|$.

Appendix A

Behaviour of the single-segment goal function

In the case where Γ lies within a perfectly ordered smectic domain, we can calculate $G(\Gamma, k)$ analytically, and so obtain an upper bound on the goal function in the absence of defects. To represent a uniform smectic with layer spacing $2\pi/q_0$, layer normal N, and average density $\rho_0 = \langle\rho\rangle$, we take

$$\rho(\mathbf{r}) = 2\rho_0 \cos^2\left(\frac{q_0 \mathbf{r}\cdot\mathbf{N}}{2}\right) . \tag{A.1}$$

Defining

$$q_{\|} = q_0\cos(\theta)\,, \quad q_{\perp} = q_0\sin(\theta)\,, \tag{A.2}$$

we obtain a goal function per unit length

$$\frac{G(\Gamma,k)}{l_\Gamma} = 2\pi\rho_0 g_{\|} g_{\perp}, \tag{A.3}$$

where

$$g_{\|} = \frac{1}{{l_\Gamma}^2(k^2-{q_{\|}}^2)^2}\left[(q_{\|}-k)\sin\left(\frac{(q_{\|}+k)l_\Gamma}{2}\right) - (q_{\|}+k)\sin\left(\frac{(q_{\|}-k)l_\Gamma}{2}\right)\right]^2 \tag{A.4a}$$

$$g_{\perp} = \frac{1}{r_{\max}^2 - r_{\min}^2}\left[\int_{r_{\min}}^{r_{\max}} r\,\mathrm{d}r\, J_1(q_\perp r)\right]^2 . \tag{A.4b}$$

In figure A we show the behaviour of $2\pi g_{\|} g_{\perp}$ as a function of θ and l_Γ. The goal function is zero for segments oriented perpendicular to the smectic layers. With

Figure A.1: The goal function per unit length, maximised over k, for a segment Γ lying in a uniformly aligned smectic with no defects. The graph shows $G(\Gamma)/l_\Gamma\rho_0$ as a function of the segment length l_Γ and its orientation θ relative to the layer normal.

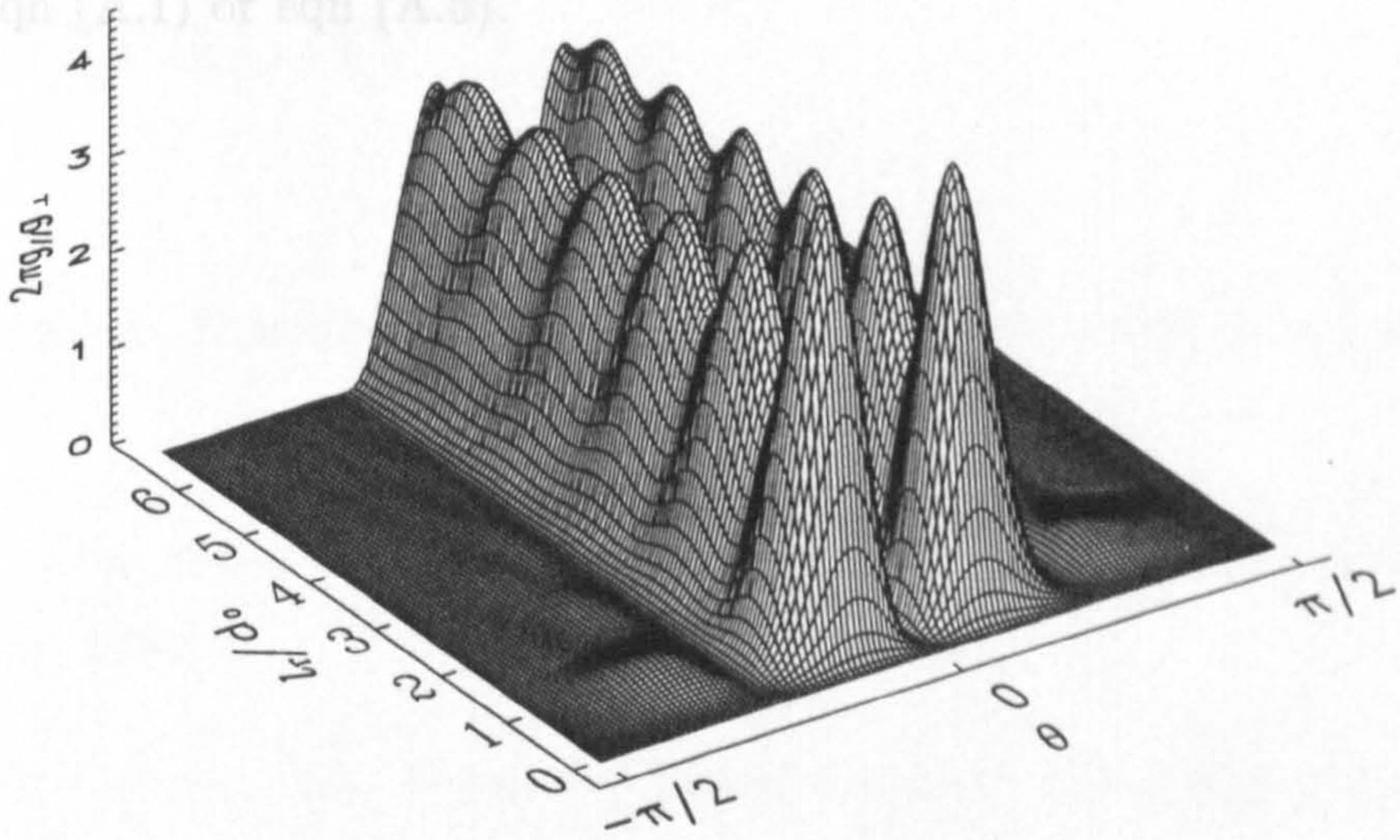

$r_{\min} = 2.0$ and $r_{\max} = 5.5$, G/l_Γ has local maxima for $|\theta| \approx 18°$, and a global maximum of $\approx 4.5\rho_0$.

A general expression for $G(\Gamma, k)$ as a function of segment orientation and distance from a defect is rather difficult to obtain, but this is not really necessary: we are interested mainly in the peak value of the goal function, which occurs when the segment is positioned along the defect. In this case, we use a model density of similar form to eqn (A.1), except that we assume $\mathbf{N} = \mathbf{z}$ and include a phase dependence on ϕ:

$$\rho(\mathbf{r}) = 2\rho_0 \cos^2\left(\frac{q_0 z - \phi}{2}\right) . \tag{A.5}$$

This gives a goal function per unit length

$$\frac{G(\Gamma, k)}{l_\Gamma} = 2\pi\rho_0 \left(r_{\max}^2 - r_{\min}^2\right) \operatorname{sinc}^2\left[\frac{(k - q_0)l}{2}\right] \tag{A.6}$$

Evaluating this for the same values of $r_{\min}$ and $r_{\max}$ as above we find a peak value at $k = q_0$ of $\approx 165\rho_0$. Comparing this with the value above, we conclude that our

chosen goal function discriminates effectively between uniform translational order and ideal twist defects. It should be stressed, however, that the goal function per unit length obtained from actual configurations (for example those in figure 5.15) is much lower, since the degree of smectic density modulation is much less than that implied by eqn (A.1) or eqn (A.5).

Bibliography

[1] P.S. Pershan. *Structure of Liquid Crystal Phases.* World Scientific, Singapore, 1988.

[2] G. W. Gray and J. W. G. Goodby. *Smectic Liquid Crystals.* Leonard Hill, Glasgow, 1984.

[3] P. G. de Gennes. *The Physics of Liquid Crystals.* Clarendon Press, Oxford, 1974.

[4] P. J. Collings. *Liquid Crystals: Nature's Delicate Phase of Matter.* Princeton University Press, Princeton, 1991.

[5] K. Huang. *Statistical Mechanics.* Wiley, New York, 1963.

[6] E. M. Lifshitz and L. P. Pitaevskii. *Statistical Physics*, volume 5 of *Landau and Lifshitz Course of Theoretical Physics.* Pergamon, Oxford, third edition, 1980.

[7] J.-P. Hansen and I. R. McDonald. *Theory of Simple Liquids.* Academic Press, London, second edition, 1986.

[8] D. Forster. *Hydrodynamic Fluctuations, Broken Symmetry and Correlation Functions*, volume 47 of *Frontiers in Physics.* Benjamin, Reading, 1975.

[9] R.J. Baxter. *Exactly solved models in statistical mechanics.* Academic Press, London, 1982.

[10] L. Onsager. *Phys. Rev.*, 65:117, 1944.

[11] P. A. Lebwohl and G. Lasher. *Phys. Rev. A*, 6:426, 1972.

[12] P. A. Lebwohl and G. Lasher. *Phys. Rev. A*, 7:2222, 1973. Erratum.

[13] P.M. Chaikin and T.C. Lubensky. *Principles of condensed matter physics.* Cambridge University Press, Cambridge, 1995.

[14] L. S. Ornstein and F. Zernike. *Proc. Akad. Sci. (Amsterdam)*, 17:793, 1914.

[15] L. Onsager. The effects of shape on the interaction of colloidal particles. *Ann. N. Y. Acad. Sci.*, 51:627, 1949.

[16] B. J. Alder and T. E. Wainwright. Phase transition for a hard sphere system. *J. Chem. Phys.*, 27:1208–1209, 1957.

[17] X.F. Yuan and R.C. Ball. Rheology of hydrodynamically interacting concentrated hard disks. *J. Chem. Phys.*, 101(10):9016–9021, 1994.

[18] Michael P. Allen, Glenn T. Evans, Daan Frenkel, and Bela Mulder. Hard convex body fluids. *Adv. Chem. Phys.*, 86:1–166, 1993.

[19] B. J. Berne and P. Pechukas. *J. Chem. Phys.*, 64:4213, 1972.

[20] J. G. Gay and B. J. Berne. *J. Chem. Phys.*, 74:3316, 1981.

[21] G. R. Luckhurst, R. A. Stephens, and R. W. Phippen. Computer-simulation studies of anisotropic systems: XIX. Mesophases formed by the Gay-Berne model mesogen. *Liq. Cryst.*, 8:451–464, 1990.

[22] E. de Miguel, L. F. Rull, M. K. Chalam, K. E. Gubbins, and F. van Swol. Location of the isotropic-nematic transition in the Gay-Berne model. *Molec. Phys.*, 72:593, 1991.

[23] R. Berardi, A. P. J. Emerson, and C. Zannoni. Monte Carlo investigations of a Gay-Berne liquid crystal. *J. Chem. Soc. Faraday Trans.*, 89:4069, 1993.

[24] E. Martín del Río. *Estudio de las propiedades interfaciales de cristales liquidos nematicos.* PhD thesis, Seville University, 1996.

[25] J. T. Brown. *The computer simulation of liquid crystals.* PhD thesis, University of Bristol, 1996.

[26] E. de Miguel, L. F. Rull, and K. E. Gubbins. Dynamics of the Gay-Berne fluid. *Phys. Rev. A*, 45:3813–3822, 1992.

[27] S. Sarman. *J. Chem. Phys.*, 101:480, 1994.

[28] S. Sarman and D. J. Evans. *J. Chem. Phys.*, 99:620, 1993.

[29] S. Sarman. *J. Chem. Phys.*, 103:393, 1995.

[30] A. M. Smondyrev, G. B. Loriot, and R. A. Pelcovits. *Phys. Rev. Lett.*, 75:2340, 1995.

[31] M. A. Bates and G. R. Luckhurst. Monte-carlo investigations of a Gay-Berne discotic at constant-pressure. *J. Chem. Phys.*, 104(17):6696–6709, 1996.

[32] R. Berardi, C. Fava, and C. Zannoni. A generalized Gay-Berne intermolecular potential for biaxial particles. *Chem. Phys. Lett.*, 236:462–468, 1995.

[33] K. Binder. *Monte Carlo methods in statistical physics.* Springer Berlin, New York, 1979.

[34] Michael P. Allen and Dominic J. Tildesley. *Computer simulation of liquids.* Clarendon Press, Oxford, hardback edition, 1987. ISBN 0–19–855375–7, 385pp.

[35] D. Frenkel. Numerical techniques to study complex liquids. In M. Baus, L. F. Rull, and J.-P. Ryckaert, editors, *Observation, prediction and simulation of phase transitions in complex fluids*, volume 460 of *NATO ASI Series C*, pages 357–419, Dordrecht, 1995. Kluwer Academic Publishers. Proceedings of the NATO Advanced Study Institute on 'Observation, prediction and simulation of phase transitions in complex fluids', Varenna, Italy, July 25–August 5, 1994.

[36] D. Frenkel and B. Smit. *Understanding molecular simulation: from algorithms to applications.* Academic Press, London, 1996.

[37] N. Metropolis, A. W. Rosenbluth, M. N. Rosenbluth, A. H. Teller, and E. Teller. *J. Chem. Phys.*, 21:1087, 1953.

[38] D. Fincham. *MS*, 11:79, 1993.

[39] A. W. Lees and S. F. Edwards. *J. Phys. C*, 5:1921, 1972.

[40] National Center for Supercomputing Applications. Hierarchical Data Format (HDF): A library and platform independent data format for the storage and exchange of scientific data. Source code and documentation is available from the URL `http://hdf.ncsa.uiuc.edu/index.html`.

[41] M. A. Warren and M.P. Allen. MG: A set of routines for interactive visualisation of molecular configurations. Source code and documentation may be downloaded via the world wide web from the URL `http://www.phy.bris.ac.uk/research/theory/simulation/software.html`.

[42] S. Brode and R. Ahlrichs. *Comput. Phys. Commun.*, 42:51, 1986.

[43] Mark R. Wilson, Michael P. Allen, Mark A. Warren, Alain Sauron, and William Smith. Replicated data and domain decomposition molecular dynamics techniques for the simulation of anisotropic potentials. *J. Comput. Chem.*, 18:478–488, 1997.

[44] F. C. Frank. *Discuss. Faraday Soc.*, 25:19, 1958.

[45] F. Leslie. In J. L. Ericksen and D. Kinderlehrer, editors, *Theory and Applications of Liquid Crystals*, page 235. Springer-Verlag, New York, 1987.

[46] S. Chandrasekhar. *Liquid Crystals.* Cambridge University Press, Cambridge, 1977.

[47] V. Freedericksz and V. Zolina. *Trans. Faraday Soc.*, 29:919, 1933.

[48] A. Saupe. *Z. Naturf. (a)*, 15:815, 1960.

[49] H. Gruler, T. Scheffer, and G. Meier. *Z. Naturf. (a)*, 27:966, 1972.

[50] I. Haller. *J. Chem. Phys.*, 57:1400, 1972.

[51] H. Gruler and G. Meier. *Mol. Cryst. Liq. Cryst.*, 16:299, 1972.

[52] P. R. Gerber and M. Schadt. *Z. Naturf. (a)*, 35:1036, 1980.

[53] S. Shtrikman, E. P. Wohlfarth, and Y. Wand. *Phys. Lett. A*, 37:369, 1971.

[54] J. L. Martinand and G. Durand. *Sol. St. Commun.*, 10:815, 1972.

[55] S. Faetti and V. Palleschi. *Liq. Cryst.*, 2:261, 1987.

[56] Douglas J. Cleaver and Michael P. Allen. Computer simulations of the elastic properties of liquid crystals. *Phys. Rev. A*, 43:1918–1931, 1991.

[57] D. J. Cleaver. *The computer simulation of liquid crystals.* PhD thesis, University of Bristol, 1991.

[58] Michael P. Allen and Daan Frenkel. Calculation of liquid crystal Frank constants by computer simulation. *Phys. Rev. A*, 37:1813–1816, 1988.

[59] Michael P. Allen and Daan Frenkel. Calculation of liquid crystal Frank constants by computer simulation. *Phys. Rev. A*, 42:3641, 1990. Erratum.

[60] Broto Tjipto-Margo, Glenn T. Evans, Michael P. Allen, and Daan Frenkel. Elastic constants of hard and soft nematic liquid crystals. *J. Phys. Chem.*, 96:3942–3948, 1992.

[61] Michael P. Allen, Daan Frenkel, and Julian Talbot. Molecular dynamics simulation using hard particles. *Comput. Phys. Rep.*, 9:301–355, 1989.

[62] D. J. Adams, G. R. Luckhurst, and R. W. Phippen. *Molec. Phys.*, 61:1575, 1987.

[63] J. W. Emsley, G. R. Luckhurst, W. E. Palke, and D. J. Tildesley. *Liq. Cryst.*, 11:519, 1992.

[64] M. K. Chalam, K. E. Gubbins, E. de Miguel, and L. F. Rull. *Molec. Simul.*, 7:357, 1991.

[65] E. de Miguel, L. F. Rull, M. K. Chalam, and K. E. Gubbins. Liquid vapour coexistence of the Gay-Berne fluid by gibbs ensemble simulation. *Molcc. Phys.*, 71:1223, 1990.

[66] E. de Miguel, L. F. Rull, M. K. Chalam, and K. E. Gubbins. Liquid crystal phase diagram of the Gay-Berne fluid. *Molec. Phys.*, 74:405–424, 1991.

[67] C. Zannoni. In G. R. Luckhurst and G. W. Gray, editors, *The Molecular Physics of Liquid Crystals*, chapter 3, pages 191–220. Academic Press, New York, 1979.

[68] A. Poniewierski and J. Stecki. *Molec. Phys.*, 38:1931, 1979.

[69] M. D. Lipkin, S. A. Rice, and U. Mohanty. *J. Chem. Phys.*, 82:472, 1985.

[70] A. M. Somoza and P. Tarazona. *Molec. Phys.*, 72:911, 1991.

[71] Michael P. Allen, Carl P. Mason, Enrique de Miguel, and Joachim Stelzer. Structure of molecular liquids. *Phys. Rev. E*, 52:R25–R28, 1995.

[72] J. Stelzer, L. Longa, and H.-R. Trebin. *J. Chem. Phys.*, 103:3098, 1995.

[73] J. Stelzer, L. Longa, and H.-R. Trebin. Elastic constants of nematic liquid crystals from molecular dynamics simulations. *Mol. Cryst. Liq. Cryst.*, 262:455–461, 1995.

[74] R. G. Priest. *Phys. Rev. A*, 7:720, 1973.

[75] J. P. Straley. *Phys. Rev. A*, 8:2181, 1973.

[76] W. M. Gelbart and A. Ben-Shaul. *J. Chem. Phys.*, 77:916, 1982.

[77] Y. Singh and K. Singh. *Phys. Rev. A*, 33:3481, 1986.

[78] E. Govers and G. Vertogen. *Liq. Cryst.*, 5:323, 1989.

[79] A. M. Somoza and P. Tarazona. Frank elastic constants of a nematic liquid crystal of hard molecules. *Phys. Rev. A*, 40:6069–6076, 1989.

[80] J. Nehring and A. Saupe. *J. Chem. Phys.*, 56:5527, 1972.

[81] E. Govers and G. Vertogen. *Liq. Cryst.*, 2:31, 1987.

[82] J.-P. Ryckaert, G. Ciccotti, and H. J. C. Berendsen. *J. Comput. Phys.*, 23:327, 1977.

[83] G. Ciccotti, M. Ferrario, and J.-P. Ryckaert. *Molec. Phys.*, 47:1253, 1982.

[84] G. Ciccotti and J. P. Ryckaert. *Comput. Phys. Rep.*, 4:345, 1986.

[85] Michael P. Allen. Simulation of condensed phases using the Distributed Array Processor. In *Parallel Computing in Chemical Physics*, volume 84, pages 399–411, Chicago 1991, 1993.

[86] Michael P. Allen and Dominic J. Tildesley. *Computer simulation of liquids.* Clarendon Press, Oxford, paperback edition, 1989. ISBN 0–19–855645–4, 385pp.

[87] U. Fabbri and C. Zannoni. *Molec. Phys.*, 58:763, 1986.

[88] Z. Zhang, O. G. Mouritsen, and M. J. Zuckermann. Weak first-order orientational transition in the lebwohl-lasher model for liquid crystals. *Phys. Rev. Lett.*, 69:2803–2806, 1992.

[89] Z. Zhang, M. J. Zuckermann, and O. G. Mouritsen. Weak first-order orientational transition in the lebwohl-lasher model for liquid crystals. *Molec. Phys.*, 80:1195, 1993.

[90] Michael P. Allen and Daan Frenkel. Observation of dynamical precursors of the isotropic-nematic transition by computer simulation. *Phys. Rev. Lett.*, 58:1748–1750, 1987.

[91] Shuang Tang, Glenn T. Evans, Carl P. Mason, and Michael P. Allen. Shear viscosity for fluids of hard ellipsoids: a kinetic theory and molecular dynamics study. *J. Chem. Phys.*, 102:3794–3811, 1995.

[92] J. Stecki and A. Kloczkowski. *J. Phys., Paris*, 40(C3):360–362, 1979.

[93] J. Stecki and A. Kloczkowski. *Molec. Phys.*, 51:42, 1981.

[94] A. Perera, G. N. Patey, and J. J. Weis. Density functional theory applied to the isotropic-nematic transition in model liquid crystals. *J. Chem. Phys.*, 89:6941, 1988.

[95] C. Gray and K. E. Gubbins. *Theory of Molecular Fluids.* Clarendon Press, Oxford, 1984.

[96] P. H. Fries and G. N. Patey. *J. Chem. Phys.*, 82:429, 1985.

[97] L. Blum and A. J. Torruella. *J. Chem. Phys.*, 56:303, 1972.

[98] L. Blum. *J. Chem. Phys.*, 57:1862, 1972.

[99] L. Blum. *J. Chem. Phys.*, 58:3295, 1973.

[100] R. J. Baxter. *Phys. Rev.*, 154:170, 1967.

[101] A. J. Bray. *AP*, 43(3):357–459, 1994.

[102] S. R. Renn and T. C. Lubensky. Abrikosov dislocation lattice in a model of the cholesteric-to-smectic-a transition. *Phys. Rev. A*, 38:2132, 1988.

[103] J. W. Goodby, M. A. Waugh, S. M. Stein, E. Chin, R. Pindak, and J.S. Patel. *Nature*, 337(2):449–452, 1989.

[104] L. Navailles, P. Barois, and H. T. Nguyen. *PRL*, 71(4):545–548, 1993.

[105] Y. Galerne. *PRL*, 72(8):1299, 1994.

[106] L. Navailles, P. Barois, and H. T. Nguyen. *PRL*, 72(8):1300, 1994.

[107] K. J. Ihn, J. A. N. Zasadzinski, R. Pindak, A. J. Slaney, and J. Goodby. Obervations of the liquid crystal analog of the abrikosov phase. *Science*, 258:275–278, 1992.

[108] J. S. Patel. Possibility of twist-grain-boundary structure in nonchiral liquid crystals. *Phys. Rev. E*, 49:R3594–R3597, 1994.

[109] S. Fraden. Phase transitions in colloidal suspensions of virus particles. In M. Baus, L. F. Rull, and J.-P. Ryckaert, editors, *Observation, prediction and simulation of phase transitions in complex fluids*, volume 460 of *NATO ASI Series C*, pages 113–164, Dordrecht, 1995. Kluwer Academic Publishers. Proceedings of the NATO Advanced Study Institute on 'Observation, prediction and simulation of phase transitions in complex fluids', Varenna, Italy, July 25–August 5, 1994.

[110] Martin Bates. Private communication.

[111] W. H. Press, B. P. Flannery, S. A. Teukolsky, and W. T. Vetterling. *Numerical Recipes*. Cambridge University Press, Cambridge, 1986.